

**INFLUENCE OF MANGANESE SUBSTITUTION ON
MICROSTRUCTURAL AND ELECTRO-MAGNETIC PROPERTIES
OF NANOCRYSTALLINE Li-Ni-Zn FERRITES**

*A Dissertation Submitted to the
Department of Physics, Bangladesh University of Engineering & Technology, Dhaka, in
Partial Fulfillment of Requirement for the Degree of Master of Philosophy in Physics*

SUBMITTED BY

Md. Moiful Alam

Examination Roll No. : 0413143016F

Session of Enrollment : April, 2013

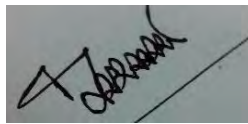


**DEPARTMENT OF PHYSICS, FACULTY OF ENGINEERING
BANGLADESH UNIVERSITY OF ENGINEERING & TECHNOLOGY (BUET)
DHAKA-1000, BANGLADESH**

March, 2019

Candidate's Declaration

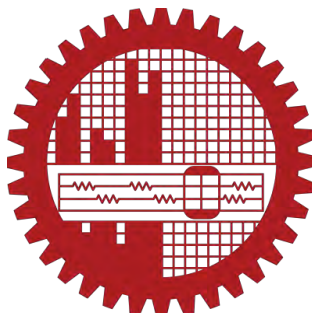
It is hereby declared that this thesis or any part of it has not been submitted elsewhere for the award of any degree or diploma.



.....

Md. Moiful Alam



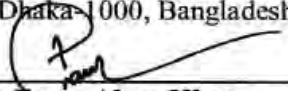


BANGLADESH UNIVERSITY OF ENGINEERING & TECHNOLOGY (BUET)
DEPARTMENT OF PHYSICS, DHAKA-1000, BANGLADESH



CERTIFICATION OF THESIS

The thesis titled “**INFLUENCE OF MANGANESE SUBSTITUTION ON MICROSTRUCTURAL AND ELECTRO-MAGNETIC PROPERTIES OF NANOCRYSTALLINE Li-Ni-Zn FERRITES**” submitted by **Md. Moiful Alam**, Examination Roll No.: 0413143016F, Registration No.: 0413143016, Session: April/2013, has been accepted as satisfactory in partial fulfillment of the requirement for the degree of **Master of Philosophy (M. Phil.)** in Physics on March 23, 2019.

BOARD OF EXAMINERS

- | | | |
|----|---|--------------------------|
| 1. | ()
Dr. A. K. M. Akther Hossain
Professor, Department of Physics,
BUET, Dhaka-1000, Bangladesh | Chairman
(Supervisor) |
| 2. | ()
Dr. Md. Forhad Mina
Professor & Head, Department of Physics,
BUET, Dhaka-1000, Bangladesh | Member
(Ex-Officio) |
| 3. | ()
Dr. Md. Feroz Alam Khan
Professor, Department of Physics,
BUET, Dhaka-1000, Bangladesh | Member |
| 4. | ()
Dr. Mohammad Khurshed Alam
Assistant Professor, Department of Physics,
BUET, Dhaka-1000, Bangladesh | Member |
| 5. | ()
Dr. Ain-ul Huda
Professor & Chairman, Department of Physics,
Jagannath University, Dhaka-1100, Bangladesh | Member
(External) |

*"Dedicated to my Beloved Son
Md. Mustahseen Adiyaat (Taheen)
& his Mom"*

*--- Md. Moiful Alam
(Author)*

ACKNOWLEDGEMENTS

First of all, I would like to express all my admiration and devotion to the *Allah Subhanahu Wa Ta'ala*, the most beneficent who has enabled me to complete this research successfully. After that, I would like to express my heartfelt gratitude to my Honorable supervisor *Prof. Dr. A. K. M. Akther Hossain*, Department of Physics, *BUET*, for his persistent cooperation and active supervision without which the completion of the present research would never be possible. I am ever grateful for his constant direction, motivation, encouragement, constructive criticism, and guidance in pursuing the whole investigation of this current work. His expertise, understanding, patience, vast knowledge, and skill in many areas added considerably to my experience.

It was really difficult for me to perform my *M. Phil.* research work at *BUET* without amiable assistance, sincere support, and cordial collaboration from many friendly people of my surroundings.

I am cordially grateful to *Prof. Dr. Md. Forhad Mina*, Head, Dept. of Physics, *BUET*, for his valuable suggestions, appreciations, and patient in every step of my thesis. I would like to express my gratitude to *Prof. Dr. Md. Abu Hashan Bhuiyan*, *Prof. Dr. Jiban Podder*, *Prof. Dr. Md. Feroz Alam Khan*, *Prof. Dr. Nasreen Akter*, *Dr. Mohammad Abu Sayem Karal*, *Dr. Mohammad Khurshed Alam*, and all other faculty members of the Dept. of Physics, *BUET*, for their inspiration and cooperation. I remain indebted to the Dept. of Physics, *BUET*, for providing me this platform of excellence.

I am also thankful to the Dept. of Glass and Ceramic Engineering (*GCE*) of *BUET*, for allowing me to use the *X-ray Diffraction (XRD)* and *Field Emission Scanning Electron Microscopy (FESEM)* devices. I am also grateful to all of the *Ph. D. and M. Phil.* Researchers of the *Experimental Solid State Physics Lab* of *BUET* for their sufficient support and incredible inspiration.

Finally, I would like to mention very special gratefulness for the ethical support and sustaining inspiration provided by my *friends and family*. Their love, care, and affection encouraged me throughout the dissertation work.

Md. Moiful Alam

March, 2019

ABSTRACT

Mn substituted *Li-Ni-Zn* ferrite nanoparticles with nominal compositions of $Li_{0.15}Ni_{0.30-x}Mn_xZn_{0.40}Fe_{2.15}O_4$ (where $x=0.00, 0.03, 0.06, 0.09, 0.12, \text{ and } 0.15$) were synthesized by the chemical sol-gel auto-combustion technique. Disk- and toroid-shaped samples prepared from each composition have been sintered at the temperature of 1373, 1423, 1473, and 1523 K for 4~5 h. The internal structure was characterized by X-ray diffraction (XRD), which has confirmed the formation of spinel structure for each composition consist of major spinel cubic phase with the minor impurity phases (Fe_2O_3 and MnO). The crystallite size of the as-grown powder varied from 46 to 52 nm estimated by using Debye-Scherrer formula. The lattice constant (a_o) slightly increased with the increase of *Mn* content up to $x=0.12$, beyond that a slight decrease in a_o was observed. Both theoretical density (ρ_{th}) and bulk density (ρ_B) decreased in a similar fashion with the increase of *Mn* content except $x=0.15$, in present ferrite samples for a fixed sintering temperature ($T_s=1523$ K). An opposite trend was found for the porosity of the samples. The density of various samples increased and as expected porosity decreased with T_s . The mean ionic radius of the variant ions, as well as hopping lengths of the samples sintered at optimum T_s , were also observed. To reveal the microstructure of the ferrites, the surface micrographs and the elemental analyses of the samples were taken using Field Emission Scanning Electron Microscopy (FESEM) and Energy Dispersive X-ray Spectroscopy (EDS), respectively. The average grain size (D_{grain}) was found to increase with increasing Mn^{2+} substitution up to $x=0.12$, beyond that D_{grain} decreased, which was estimated by linear intercept technique from the FESEM micrograph. The real part (μ_i') and imaginary part (μ_i'') of initial permeability, relative quality factor (RQF), and magnetic loss factor ($\tan\delta_M$) varied with *Mn* content for a fixed T_s . It was also observed that μ_i' of $Li_{0.15}Ni_{0.18}Mn_{0.12}Zn_{0.40}Fe_{2.15}O_4$ increased with T_s . The maximum value of μ_i' (=334) and RQF (=14067) were observed for $Li_{0.15}Ni_{0.18}Mn_{0.12}Zn_{0.40}Fe_{2.15}O_4$ sintered at 1523 K, which are 7% and 16% greater compared to the parent composition, respectively. As a result, the minimum $\tan\delta_M$ was observed in this composition. The weakening of exchange interaction confirmed by increasing the a_o and decreasing the Néel temperature (T_N) as the increase of *Mn* content up to $x=0.12$. The real part of dielectric constant (ϵ'), dielectric loss tangent ($\tan\delta_E$), complex impedance, ac conductivity (σ_{ac}) as well as ac resistivity (ρ_{ac}) were studied in the frequency range 100 Hz-100 MHz to achieve the information about the dielectric features of the studied ferrites.

TABLE OF CONTENTS

ABSTRACT.....	VI
TABLE OF CONTENTS.....	VII
LIST OF TABLES.....	XI
LIST OF FIGURES.....	XII
LIST OF ABBREVIATIONS.....	XVI
LIST OF SYMBOLS.....	XVII
CHAPTER: 1 INTRODUCTION.....	1~7
1.1 Introduction to spinel ferrites.....	1
1.2 Manganese substituted <i>Li-Ni-Zn</i> ferrites.....	1
1.3 Motivation, objectives, and possible outcome.....	2
1.3.1 Motivation.....	2
1.3.2 Objectives with specific aims.....	3
1.3.3 Possible outcome of the present work.....	3
1.4 Outline of the thesis.....	4
References.....	5
CHAPTER: 2 BACKGROUND AND LITERATURE REVIEW.....	8~53
2.1 Aspects of magnetism: General ideas.....	8
2.2 Magnetism and its origin.....	8
2.2.1 Magnetic moment of atoms.....	11
2.2.2 Magnetic moment of electrons.....	12
2.3 Magnetic behavior of materials.....	14

2.4	Classification of magnetic behavior of materials.....	15
2.4.1	Diamagnetism.....	16
2.4.2	Paramagnetism.....	17
2.4.3	Ferromagnetism.....	17
2.4.4	Antiferromagnetism.....	19
2.4.5	Ferrimagnetism.....	19
2.5	Ferrites.....	20
2.5.1	Soft magnetic materials (soft ferrites).....	20
2.5.2	Crystal structure of spinel ferrites.....	21
2.5.3	Cation distribution of spinel ferrites.....	23
2.6	Hysteresis loop.....	25
2.6.1	Magnetization in the hysteresis loop.....	26
2.6.2	Demagnetization or degaussing in the hysteresis loop.....	26
2.6.3	Different magnetic properties in the hysteresis loop.....	27
2.7	Magnetic domains.....	27
2.7.1	Structure of domain wall.....	31
2.8	Microstructure of magnetic materials.....	32
2.9	Theories of initial permeability.....	34
2.9.1	Mechanisms of permeability.....	37
2.9.2	Wall permeability.....	37
2.9.3	Rotational permeability.....	39
2.10	Interaction between magnetic moments on lattice sites.....	41
2.11	Magnetic exchange interaction.....	43
2.11.1	Super-exchange interaction.....	43
2.12	Two sub-lattices in spinel ferrites.....	45
2.13	Magnetic structure of substituted ferrites.....	47
2.13.1	Néel's collinear model.....	47
2.13.2	Non-collinear model.....	48
2.14	Conduction mechanism in ferrites.....	49
2.15	Dielectric properties of materials.....	50

2.15.1	Dielectric constant.....	50
2.15.2	Dielectric loss.....	50
References.....		51

CHAPTER: 3 SYNTHESSES AND STRUCTURAL CHARACTERIZATION.....54~63

3.1	Goal to ferrite sample preparation.....	54
3.2	Sample preparation techniques.....	54
3.3	Auto-combustion synthesis.....	56
3.4	Calcination, pressing, sintering, and thermal etching.....	57
3.4.1	Calcination.....	57
3.4.2	Pressing.....	58
3.4.3	Sintering.....	58
3.4.4	Thermal etching.....	60
3.5	Composition of the studied ferrite.....	60
3.6	Synthesis of present nanoparticles.....	61
3.7	Preparation of the present samples.....	62
References.....		62

CHAPTER: 4 EXPERIMENTAL TECHNIQUES.....64~75

4.1	Study of <i>X</i> -ray diffraction.....	64
4.1.1	Phase identification by <i>XRD</i>	64
4.1.2	Crystallite size measurement.....	65
4.1.3	Lattice parameter, Lattice constant, and $r_{(variant)}$ measurements.....	68
4.1.4	Density, porosity, and hopping length measurements.....	68
4.2	Surface morphology analysis.....	70
4.3	Complex initial permeability measurement.....	70
4.3.1	Techniques for the initial permeability measurement.....	71
4.3.2	Frequency characteristics of the ferrite samples.....	71

4.4	Temperature-dependent μ'_i and Néel temperature measurements.....	72
4.4.1	Techniques for measurement of temperature-dependent μ'_i	72
4.4.2	The Néel temperature measurement.....	73
4.5	Dielectric properties measurement.....	73
4.6	Complex impedance spectroscopy measurement.....	74
4.7	<i>ac</i> conductivity and <i>ac</i> resistivity measurements.....	74
	References.....	74

CHAPTER: 5 RESULTS AND DISCUSSION.....76~106

5.1	Structural analysis.....	76
5.1.1	X-ray diffraction analysis.....	76
5.1.2	Crystallite size.....	77
5.1.3	Lattice constant and $r_{(variant)}$	79
5.1.4	Density and porosity.....	80
5.2	Surface morphology.....	83
5.3	Complex initial permeability.....	88
5.4	Temperature-dependent permeability and Néel temperature.....	95
5.5	<i>dc</i> magnetization of $Li_{0.15}Ni_{0.30-x}Mn_xZn_{0.40}Fe_{2.15}O_4$	96
5.6	Dielectric properties of $Li_{0.15}Ni_{0.30-x}Mn_xZn_{0.40}Fe_{2.15}O_4$	98
5.7	Complex impedance spectroscopy study.....	100
5.8	<i>ac</i> conductivity and <i>ac</i> resistivity.....	101
	References.....	103

CHAPTER: 6 CONCLUSIONS.....107~109

6.1	Major findings of present study.....	107
-----	--------------------------------------	-----

6.2	Suggestions for further research.....	108
APPENDIX-A.....		110
APPENDIX-B.....		110
APPENDIX-C.....		111

LIST OF TABLES

<i>Table No.</i>	<i>Caption of the Table</i>	<i>Page No.</i>
Table 2.1	Summary of ferrite structure types, typified by changes in the Fe_2O_3 - MeO (or Me_2O_3) modifier oxide ratios	20
Table 5.1	<i>FWHM</i> and particle size of various $Li_{0.15}Ni_{0.30-x}Mn_xZn_{0.40}Fe_{2.15}O_4$ samples sintered at 1523 K	78
Table 5.2	The lattice constant, the mean ionic radius of the variant ions, theoretical density, bulk density, porosity, the distance between magnetic ions in the <i>A</i> -sites, shared sites, and <i>B</i> -sites, and average grain size of various $Li_{0.15}Ni_{0.30-x}Mn_xZn_{0.40}Fe_{2.15}O_4$ samples sintered at 1523 K	81
Table 5.3	The real part of initial permeability (μ_i') at 1 MHz, maximum relative quality factor (RQF_{max}), and resonance frequency (f_r) for various $Li_{0.15}Ni_{0.30-x}Mn_xZn_{0.40}Fe_{2.15}O_4$ spinel ferrite nanoparticles sintered at 1523 K including expected total (net) magnetization (M_T) for various samples	89

LIST OF FIGURES

<i>Fig. No.</i>	<i>Caption of the Fig.</i>	<i>Page No.</i>
Fig. 2.1	A spin magnetic moment associated with it due to the electron itself spinning (like the earth on its own axis)	10
Fig. 2.2	Spinning electron on its own axis and orbiting electron around the nucleus (like the earth around the sun)	10
Fig. 2.3	Schematic diagrams of 5 (five) major magnetic materials based on their magnetic orderings	16
Fig. 2.4	The inverse susceptibility varies with temperature (T) for (a) Paramagnetic, (b) Ferromagnetic, (c) Ferrimagnetic, and (d) Antiferromagnetic materials. ' T_N ' and ' T_C ' are Néel temperature and Curie temperature, respectively	18
Fig. 2.5	Two sub-cells of a unit cell of the spinel structure	22
Fig. 2.6	Unit cell of spinel ferrite divided into eight sub-cells with A - and B -sites	22
Fig. 2.7	Hysteresis loop	25
Fig. 2.8	Stages of the rotation of orientation and increase in the size of magnetic domains after applying external field.	28
Fig. 2.9	Schematic illustration of the breakup of magnetization into domains: (a) Single domain, (b) Two domains, (c) Four domains, and (d) Closure domains	30
Fig. 2.10	Schematic representation of a 180° domain wall	31
Fig. 2.11	Porosity character: (a) Inter-granular and (b) Intra-granular	34
Fig. 2.12	Grain growth: (a) Discontinuous and (b) Duplex (schematic)	34
Fig. 2.13	Schematic magnetization curve showing initial permeability ' μ_i ' (the slope of the curve at low fields) and the main magnetization mechanism in each magnetization range	36
Fig. 2.14	Magnetization by wall motion and spin rotation	38

Fig. 2.15	Schematic diagram of nearest neighbors of (a) a tetrahedral site, (b) an octahedral site, and (c) an anion site	41
Fig. 2.16	Interionic angles in the spinel structure for the different type of lattice site interactions	42
Fig. 2.17	Three major types of super-exchange interactions in spinel ferrites are as follows: ' J_{AB} ', ' J_{BB} ', and ' J_{AA} '. The small empty circle is A -site, the small solid circle is B -site, and the large empty circle is oxygen anion	44
Fig. 2.18	Schematic representation of ions ' M ' and ' M ' and the O^{2-} ion through which their super exchange is made. ' r ' and ' q ' are the centre to centre distances from ' M ' and ' M ' respectively to O^{2-} and ' φ ' is the angle between ' M ' and ' M '	45
Fig. 3.1	Flow-chart of the stages in preparation of spinel ferrite	56
Fig. 3.2	Schematic representation of sintering stages: (a) Green body, (b) Initial stage, (c) Intermediate stage, and (d) Final stage	59
Fig. 3.3	Steps in preparation of present spinel ferrite samples	61
Fig. 3.4	(a) Disk and (b) Toroid shaped samples	62
Fig. 4.1	Bragg's law of diffraction	65
Fig. 4.2	The effect of fine particle size on diffraction curves (Schematic): (a) Small particle size and (b) Large particle size	66
Fig. 5.1	X -ray diffraction pattern of nanocrystalline $Li_{0.15}Ni_{0.30-x}Mn_xZn_{0.40}Fe_{2.15}O_4$ sintered at 1523 K	77
Fig. 5.2	The XRD patterns for various as prepared powder of $Li_{0.15}Ni_{0.30-x}Mn_xZn_{0.40}Fe_{2.15}O_4$ for (311) peak sintered at 1523 K	78
Fig. 5.3	Variation of the a_o and the $r_{(variant)}$ as a function of Mn content for $Li_{0.15}Ni_{0.30-x}Mn_xZn_{0.40}Fe_{2.15}O_4$ sintered at 1523 K	80
Fig. 5.4	The variation of ρ_{th} , ρ_B , and $P(\%)$ as a function of Mn content in $Li_{0.15}Ni_{0.30-x}Mn_xZn_{0.40}Fe_{2.15}O_4$ sintered at 1523 K	81

Fig. 5.5	The variation of bulk density and porosity (%) as a function of Mn content in $Li_{0.15}Ni_{0.30-x}Mn_xZn_{0.40}Fe_{2.15}O_4$ sintered at 1523 K	81
Fig. 5.6	The variation of bulk density as a function of T_s for various $Li_{0.15}Ni_{0.30-x}Mn_xZn_{0.40}Fe_{2.15}O_4$ samples	82
Fig. 5.7	The FESEM micrographs of manganese substituted spinel ferrite nanoparticles of various $Li_{0.15}Ni_{0.30-x}Mn_xZn_{0.40}Fe_{2.15}O_4$ sintered at 1523 K, where the magnification is 5000	84
Fig. 5.8	The FESEM micrographs of manganese substituted spinel ferrite nanoparticles of various $Li_{0.15}Ni_{0.30-x}Mn_xZn_{0.40}Fe_{2.15}O_4$ sintered at 1523 K, where the magnification is 10000	85
Fig. 5.9	The FESEM micrographs of manganese substituted spinel ferrite nanoparticles of various $Li_{0.15}Ni_{0.30-x}Mn_xZn_{0.40}Fe_{2.15}O_4$ sintered at 1523 K, where the magnification is 15000	86
Fig. 5.10	The EDS spectrum of manganese substituted spinel ferrite nanoparticles of various $Li_{0.15}Ni_{0.30-x}Mn_xZn_{0.40}Fe_{2.15}O_4$ sintered at 1523 K	87
Fig. 5.11	The variation of (a) μ_i' and (b) μ_i'' as a function of frequency for various $Li_{0.15}Ni_{0.30-x}Mn_xZn_{0.40}Fe_{2.15}O_4$ spinel ferrite nanoparticles sintered at 1523 K	90
Fig. 5.12	The variation of (a) RQF and (b) $\tan\delta_M$ as a function of frequency for various $Li_{0.15}Ni_{0.30-x}Mn_xZn_{0.40}Fe_{2.15}O_4$ spinel ferrite nanoparticles sintered at 1523 K	90
Fig. 5.13	The variation of (a) μ_i' and (b) μ_i'' as a function of frequency for $Li_{0.15}Ni_{0.30-x}Mn_xZn_{0.40}Fe_{2.15}O_4$ ($x=0.12$) spinel ferrite nanoparticles sintered at various temperatures	91
Fig. 5.14	The variation of (a) μ_i' and (b) μ_i'' as a function of sintering temperature for various $Li_{0.15}Ni_{0.30-x}Mn_xZn_{0.40}Fe_{2.15}O_4$ spinel ferrite nanoparticles at a constant frequency of 1 MHz	92

Fig. 5.15	The variation of (a) μ_i' and (b) μ_i'' as a function of <i>Mn</i> content (<i>x</i>) for various $Li_{0.15}Ni_{0.30-x}Mn_xZn_{0.40}Fe_{2.15}O_4$ spinel ferrite nanoparticles sintered at 1523 K, at different frequencies	93
Fig. 5.16	The variation of (a) μ_i' and (b) μ_i'' as a function of <i>Mn</i> content (<i>x</i>) for various $Li_{0.15}Ni_{0.30-x}Mn_xZn_{0.40}Fe_{2.15}O_4$ spinel ferrite nanoparticles at a constant frequency of 1 MHz sintered at various temperatures	93
Fig. 5.17	The variation of (a) RQF and (b) $\tan\delta_M$ as a function of <i>Mn</i> content (<i>x</i>) for various $Li_{0.15}Ni_{0.30-x}Mn_xZn_{0.40}Fe_{2.15}O_4$ spinel ferrite nanoparticles at a constant frequency of 1 MHz sintered at various temperatures	94
Fig. 5.18	(a) The temperature-dependent μ_i' (at constant frequency 1 MHz) and (b) Variation of a_o and T_N with <i>Mn</i> content (<i>x</i>) for various $Li_{0.15}Ni_{0.30-x}Mn_xZn_{0.40}Fe_{2.15}O_4$ spinel ferrite nanoparticles sintered at 1523 K	95
Fig. 5.19	The variation of the (a) Real part of dielectric constant (ϵ') and (b) Loss tangent ($\tan\delta_E$) as a function of frequency at room temperature for various $Li_{0.15}Ni_{0.30-x}Mn_xZn_{0.40}Fe_{2.15}O_4$ spinel ferrite nanoparticles sintered at 1523 K	99
Fig. 5.20	(a) The variation of Z' with frequency and (b) The Cole-Cole plot at room temperature for various $Li_{0.15}Ni_{0.30-x}Mn_xZn_{0.40}Fe_{2.15}O_4$ spinel ferrite nanoparticles sintered at 1523 K	100
Fig. 5.21	The variation of (a) <i>ac</i> conductivity (σ_{ac}) and (b) <i>ac</i> resistivity (ρ_{ac}) as a function of frequency for various $Li_{0.15}Ni_{0.30-x}Mn_xZn_{0.40}Fe_{2.15}O_4$ spinel ferrites sintered at 1523 K	102

LIST OF ABBREVIATIONS

<i>AC</i>	: Alternating Current
<i>DC</i>	: Direct Current
<i>EDS</i>	: Energy Dispersive <i>X</i> -ray Spectroscopy
<i>EDX</i>	: Energy Dispersive <i>X</i> -ray
<i>FESEM</i>	: Field Emission Scanning Electron Microscopy
<i>FWHM</i>	: Full Width at Half Maximum
<i>RF</i>	: Radio Frequency
<i>RQF</i>	: Relative Quality Factor
<i>SEM</i>	: Scanning Electron Microscopy
<i>XRD</i>	: <i>X</i> -ray Diffraction

LIST OF SYMBOLS

Angular velocity	: ω
Avogadro's number	: N_A
Bohr magneton	: μ_B
Bulk density	: ρ_B
Complex impedance	: Z
Critical field	: H_{cr}
Curie temperature	: T_c
Dielectric loss factor	: $\tan\delta_E$
Domain wall energy	: Γ
Domain wall susceptibility	: χ_w
Exchange integral	: J
Imaginary part of complex impedance	: Z''
Imaginary part of complex permeability	: μ_i''
Inductance of the winding coil without sample	: L_o
Initial permeability	: μ_i
Inter-granular porosity	: P_{inter}
Intra-granular porosity	: P_{intra}
Intrinsic rotational susceptibility	: χ_{spin}
Landé splitting factor	: G
Magnetic induction	: B
Magnetic loss factor	: $\tan\delta_M$
Magnetization	: M
Magneto-crystalline anisotropy constant	: K_1
Néel temperature	: T_N
Nelson-Riley function	: $F(\theta)$
Porosity	: P
Real part of complex impedance	: Z'
Real part of complex permeability	: μ_i'
Resonance frequency	: f_r
Restoring force coefficient	: A
Saturation magnetization	: M_s
Self-inductance of the sample core	: L_s
Sintering temperature	: T_S
Theoretical density	: ρ_{th}
Total anisotropy	: K

CHAPTER 1

INTRODUCTION

This chapter focused on the basic and general information of the ferrite materials. The importance of the spinel ferrites and applications of it's as 'magnetic nanoparticles' are also discussed here. Motivation, objectives with specific aims, and possible outcome of this present study are also briefly discussed in this chapter. This chapter also includes an outline of the thesis.

1.1 Introduction to spinel ferrites

Spinel ferrites are the prominent magnetic ceramics which are attractive for electrical and biomedical applications for their high electrical resistivity, low dielectric loss, low magnetic loss, high saturation magnetization, excellent chemical stability, mechanical hardness, squareness of hysteresis loop, high Néel temperature, high permeability in the radio-frequency (*RF*) region, easy to fabrication, and reasonable cost [1-8]. From the application point of view, spinel ferrites become the interesting research field for many researchers over recent decades. These ferrites show various magnetic properties based on their chemical composition and cation distribution in tetrahedral-*A* sites and octahedral-*B* sites in AB_2O_4 crystal structure [9].

The chemical formula of magnetically soft ferrites which have a cubic (spinel) structure, is generally expressed as $MeFe_2O_4$, where 'Me' represents a divalent metal ion (e.g. Fe^{2+} , Ni^{2+} , Mn^{2+} , Mg^{2+} , Co^{2+} , Zn^{2+} , Cu^{2+} , etc.). The microstructural, electrical and magnetic features of ferrites depend on several factors including the method of preparation, the quantity of substitution, sintering temperature, sintering atmosphere, and chemical composition [10].

1.2 Manganese substituted *Li-Ni-Zn* ferrites

It was found that *Ni-Zn* and *Mn-Zn* ferrites have been investigated widely. The *Ni-Zn* ferrites have higher resistivity and *Mn-Zn* ferrites exhibit higher permeability. The *Ni-Zn* ferrites are most suitable for frequencies over 10^6 Hz and *Mn-Zn* ferrites are

suitable up to 3×10^6 Hz [11-16]. The lattice parameter, average grain size, and initial permeability increased with *Mn*-substitution in *Ni-Zn* ferrites. In this case, the initial permeability strongly depends on the average grain size and porosity [17]. However, studies on the combination of these two ferrites (*Ni-Zn* and *Mn-Zn*) are inadequate.

Many researchers also have investigated the structural, electrical and magnetic properties of *Li-Mn* [18], *Li-Ni* [19], *Li-Co* [20], *Li-Zn* [21], *Li-Cu-Co-Zn* [22], and *Li-Mg-Ni* ferrites [23,24] prepared by auto-combustion method and solid state reaction technique. Recently studies on *Li-Ni-Mn* [25] and *Li-Ni-Zn* [26] ferrites have been carried out by the researchers. The Curie temperature is found to increase with *Li* content in *Li-Ni-Mn* ferrites and real part of initial permeability is found to increase with increasing *Zn* content in *Li-Ni-Zn* ferrites. All these indicated that investigations on *Mn*-substitutions in *Li-Ni-Zn* ferrites will open a new window in material research. In this present research, microstructural and electro-magnetic properties of nanocrystalline $Li_{0.15}Ni_{0.30-x}Mn_xZn_{0.40}Fe_{2.15}O_4$ have been investigated.

1.3 Motivation, objectives, and possible outcome

For more than half a century ferrite materials have been considered as most important electronic materials. Because of their high resistivity, ferrites are especially convenient for high frequency uses. The high-frequency response of the complex permeability is very useful in determining the convenient frequency range in which a particular ferrite material can be applied in practical purpose. From the relative magnitudes of the real and imaginary part of the complex permeability, the mechanism of eddy current losses and damping of domain wall motion can be understood. Therefore, the composition, sintering temperature, and microstructure have a very powerful effect on the frequency response.

1.3.1 Motivation

Bangladesh is very dependent on the imported soft magnetic materials including ferrite core. So to save foreign currency, we need to concentrate on developing a high-quality ferrite with desired characteristics in our country.

However, the selection of these present compositions of *Mn* substituted *Li-Ni-Zn* ferrite is to achieve suitable permeability, loss reduction, adequate saturation magnetization, justified Néel temperature, at last, but not the least cost effectiveness.

In addition, from scientific point of view, researchers need to focus on ferrite material to enhance its features to develop effective future technology.

1.3.2 Objectives with specific aims

The main objectives of the present research are as follows:

- a) Preparation of various $Li_{0.15}Ni_{0.30-x}Mn_xZn_{0.40}Fe_{2.15}O_4$ (where $x=0.00, 0.03, 0.06, 0.09, 0.12,$ and 0.15) compositions using auto-combustion technique.
- b) Investigation of surface morphology and microstructure using Scanning Electron Microscopy (*SEM*).
- c) Investigation of compositional analyses using Energy Dispersive *X*-ray (*EDX*) spectroscopy.
- d) *X*-ray diffraction (*XRD*) analysis for phase identification.
- e) Determination of initial permeability as a function of frequency (100 Hz - 120 MHz) for samples having various microstructures (e. g. grain size).
- f) Measurement of the ferrimagnetic to paramagnetic transition temperature (T_N) from the measurement of temperature dependent initial permeability.
- g) Investigation of *dc* magnetization.
- h) Investigation of dielectric properties (dielectric constant and dielectric loss).
- i) Investigation of impedance and *ac* conductivity using Impedance Analyzer.

1.3.3 Possible outcome of the present work

The possible outcome of the research is as follows:

The crystal structure and cation distribution are expected to change due to the substitution of *Mn* in $Li_{0.15}Ni_{0.30-x}Mn_xZn_{0.40}Fe_{2.15}O_4$. Due to above changes, there may be a variation of magnetic interaction between *A*-site and *B*-site cations and hence a

modification of electromagnetic properties are also expected in proposed ferrites. The results of this study might be helpful for practical application of these ferrites. For example, these ferrite materials might be applicable as the component of electronic filter, microwave devices, transducers, magnetic switches, and memory elements for the computer. Magnetic nanoparticles of these ferrites might be useful for the biomedical application.

1.4 Outline of the thesis

The overall summary of this thesis is as follows:

- The importance of the ferrite and applications of its as ‘magnetic nanoparticles’ are discussed in the *first chapter* of this thesis. Objectives with specific aims and possible outcome of this current research work are also presented here.
- A brief overview of the materials as well as the theoretical background of magnetic moment, magnetic domain, and hysteresis loop are discussed in the *second chapter*. Crystal structure of the spinel type ferrites is also described in this chapter of the thesis.
- Details of the sample preparation technique are given in the *third chapter*. This chapter also includes the structural characterization of the samples.
- Different experimental techniques (e.g. *XRD*, *SEM*, and *EDS* analysis; impedance, dielectric, and permeability measurements) that have been used in this present research are presented in the *fourth chapter*.
- The *fifth chapter* of this thesis is devoted to the results of various investigations of the study. Explanation of results in the light of existing theories is also given in this chapter.
- The conclusions including suggested future works drawn from the overall experimental results and discussion are displayed in the *sixth chapter*.

References:

- [1] Li, O. A., Lin, C. R., Chen, H. Y., Hsu, H. S., Shih, K. Y., Edelman, I. S., Wu, K. W., Tseng, Y. T., Ovchinnikov, S. G., and Lee, J. S., "Size dependent magnetic and magneto-optical properties of $\text{Ni}_{0.2}\text{Zn}_{0.8}\text{Fe}_2\text{O}_4$ nanoparticles," *Journal of Magnetism and Magnetic Materials*, vol. 408, pp. 206-212, 2016.
- [2] Verma, A., and Dube, D. C., "Processing of nickel-zinc ferrites via the citrate precursor route for high-frequency applications," *J. Am. Ceram. Soc.*, vol. 88, pp. 519-523, 2005.
- [3] Akhtar, M. N., Yahya, N., and Hussain, P. B., "Structural and magnetic characterizations of nanostructured $\text{Ni}_{0.8}\text{Zn}_{0.2}\text{Fe}_2\text{O}_4$ prepared by self-combustion method," *Int. J. Basic Appl. Sci.*, vol. 9, pp. 37-40, 2009.
- [4] Kooti, M., and Sedeh, A. N., "Synthesis and characterization of NiFe_2O_4 magnetic nanoparticles by combustion method," *J. Mater. Sci. Technol.*, vol. 29, pp. 34-38, 2013.
- [5] Mazarío, E., Herrasti, P., Morales, M. P., and Menéndez, N., "Synthesis and characterization of CoFe_2O_4 ferrite nanoparticles obtained by an electrochemical method," *Nanotechnology*, vol. 23(35), p. 355708, 2012.
- [6] Kumar, A., Kumar, P., Rana, G., Yadav, M. S., and Pant, R. P., "A study on structural and magnetic properties of $\text{Ni}_x\text{Zn}_{1-x}\text{Fe}_2\text{O}_4$ ($0.1 \leq x \leq 0.6$) ferrite nanoparticles," *Appl. Sci. Letter.*, vol. 1, pp. 33-36, 2015.
- [7] Kumar, A., Singh, A., Yadav, M. S., Arora, M., and Pant, R. P., "Finite size effect on Ni doped nanocrystalline $\text{Ni}_x\text{Zn}_{1-x}\text{Fe}_2\text{O}_4$ ($0.1 \leq x \leq 0.5$)," *Thin Solid Films*, vol. 519, pp. 1056-1058, 2010.
- [8] Shahane, G. S., Kumar, A., Arora, M., Pant, R. P., and Lal, K., "Synthesis and characterization of Ni-Zn ferrite nanoparticles," *Journal of Magnetism and Magnetic Materials*, vol. 322, pp. 1015-1019, 2010.
- [9] Peelamedu, R., Grimes, C., Agrawal, D., and Roy, R., "Ultralow dielectric constant nickel-zinc ferrites using microwave sintering," *J. Mater. Res.*, vol. 18, pp. 2292-2295, 2003.
- [10] Jalaiah, K., and Babu, K. V., "Structural, magnetic and electrical properties of nickel doped Mn-Zn spinel ferrite synthesized by sol-gel method," *Journal of Magnetism and Magnetic Materials*, vol. 423, pp. 275-280, 2017.
- [11] Hossain, A. K. M. A., Mahmud, S. T., Seki, M., Kawai, T., and Tabata, H., "Structural, electrical transport, and magnetic properties of $\text{Ni}_{1-x}\text{Zn}_x\text{Fe}_2\text{O}_4$," *Journal of Magnetism and Magnetic Materials*, vol. 312, pp. 210-219, 2007.
- [12] Singh, A. K., Goel, Mendiratta, R. G., Thakur, O. P., and Prakash, C., "Magnetic properties of Mn-substituted Ni-Zn ferrites," *J. Appl. Phys.*, vol. 92(7), pp. 3872-3876, 2002.

- [13] Rath, C., Anand, S., Das, R. P., Sahu, K. K., Kulkarni, S. D., Date, S. K., and Mishra, N. C., "Dependence on cation distribution of particle size, lattice parameter, and magnetic properties in nanosize Mn–Zn ferrite," *J. Appl. Phys.*, vol. 91(4), pp. 2211-2215, 2002.
- [14] Rezlescu, E., Sachelarie, L., Popa, P. D., and Rezlescu, N., "Effect of substitution of divalent ions on the electrical and magnetic properties of Ni-Zn-Me ferrites," *IEEE Trans. on Magnetism*, vol. 36, pp. 3962-3967, 2000.
- [15] Sattar, A. A., El-Sayed, H. M., El-Shokrofy, K. M., and El-Tabey, M. M., "Improvement of the Magnetic Properties of Mn-Ni-Zn Ferrite by the Non-magnetic Al³⁺-Ion Substitution," *J. Appl. Sci.*, vol. 5(1), pp. 162-168, 2005.
- [16] Singh, A. K., Goel, T. C., and Mendiratta, R. G., "Effect of cation distribution on the properties of Mn_{0.2}Zn_xNi_{0.8-x}Fe₂O₄," *Solid State Commun.*, vol. 125, pp. 121-125, 2003.
- [17] Hossain, A. K. M. A. et al., "Enhancement of initial permeability due to Mn substitution in polycrystalline Ni_{0.5-x}Mn_xFe₂O₄," *Journal of Magnetism and Magnetic Materials*, vol. 321, pp. 81-87, 2009.
- [18] Ravinder, D., Balachander, L., and Venudhar, Y. C., "Electrical conductivity in manganese-substituted lithium ferrites," *Mater. Letter*, vol. 49, pp. 267-271, 2001.
- [19] Trivedi, U. N., Jani, K. H., Modi, K. B., and Joshi, H. H., "Study of cation distribution in lithium doped nickel ferrite," *J. Mater. Sci. Lett.*, vol. 19, pp. 1271-1273, 2000.
- [20] Ata, A. M. A. E., Attia, S. M., Kony, D. E., and Al-Hammadi, A. H., "Spectral, initial magnetic permeability and transport studies of Li_{0.5-0.5x}Co_xFe_{2.5-0.5x}O₄ spinel ferrite," *Journal of Magnetism and Magnetic Materials*, vol. 295, pp. 28-36, 2005.
- [21] Sattar, A. A., El-Sayed, H. M., Agami, W. R., and Ghani, A. A., "Magnetic Properties and Electrical Resistivity of Zr⁴⁺ Substituted Li-Zn Ferrite," *Am. J. Appl. Sci.*, vol. 4, pp. 89-93, 2007.
- [22] Parvin, R., Momin, A. A., and Hossain, A. K. M. A., "Improvement of microstructure, initial permeability, magnetization and dielectric properties of nanocrystalline Li_xCu_{0.1}Co_{0.1}Zn_{0.8-2x}Fe_{2+x}O₄," *Journal of Magnetism and Magnetic Materials*, vol. 401, pp. 760-769, 2016.
- [23] Hossain, A. K. M. A., Rahman, M. A., Farhad, S. F. U., Vilquin, B., and Tanaka, H., "Effect of Li substitution on the magnetic properties of Li_xMg_{0.40}Ni_{0.60-2x}Fe_{2+x}O₄ ferrites," *Physica B: Condensed Matter*, vol. 406, pp. 1506-1512, 2011.
- [24] Hossain, A. K. M. A., Chowdhury, M. M. A., Vilquin, B., and Tanaka, H., "Influence of Li substitution on structural and magnetic properties of Li_xNi_{0.2}Mg_{0.8-2x}Fe_{2+x}O₄," *Mater. Chem. Phys.*, vol. 133, pp. 941-945, 2012.

- [25] Momin, A. A., Parvin, R., and Hossain, A. K. M. A., “Structural, morphological and magnetic properties variation of nickel-manganese ferrites with lithium substitution,” *Journal of Magnetism and Magnetic Materials*, vol. 423, pp. 124-132, 2017.
- [26] Islam, M. A., Hasan, M., and Hossain, A. K. M. A., “Enhancement of initial permeability and reduction of loss factor in Zn substituted nanocrystalline $\text{Li}_{0.35-0.5x}\text{Ni}_{0.3}\text{Zn}_x\text{Fe}_{2.35-0.5x}\text{O}_4$,” *Journal of Magnetism and Magnetic Materials*, vol. 424, pp. 108-114, 2017.

.....

CHAPTER 2

BACKGROUND AND LITERATURE REVIEW

This chapter includes a brief overview of the ferrite materials. Origin of magnetism as well as the theoretical background of the magnetic moment, magnetic domain, structure of domain wall, and hysteresis loop are also described in this chapter. Theories of initial permeability and crystal structure of the spinel type ferrites are also explained here.

2.1 Aspects of magnetism: General ideas

Magnetism, which is caused by the motion of electric charges, is the force exerted by magnets when they attract or repel each other. It is well known that every substance is made up of atoms, which have electrons that carry electric charges. The movement of electrons generates an electric current and causes each electron to act like a microscopic magnet. However, equal numbers of electrons spin in opposite directions cancels out the magnetism. This is happening in most substances. That's why materials such as cloth, wood or paper are said to be weakly magnetic.

In substances such as iron, cobalt, manganese, zinc, and nickel, most of the electrons spin in the same direction. This makes the atoms in these substances strongly magnetic (but they are not magnets). To become magnetized, another strongly magnetic substance must enter the magnetic field of an existing magnet [1-3].

2.2 Magnetism and its origin

Magnetism is considered as a class of physical phenomena that are mediated by magnetic fields. The electric currents and magnetic moments of elementary particles give rise to a magnetic field, which effects on other currents and magnetic moments [2,3].

The origin of magnetism lies in the orbital and spin motions of electrons and how the electrons interact with one another. The greatest way to introduce the different types of magnetism is to explain how materials respond to magnetic fields. It is just that some materials are much more magnetic than others. The main difference is that some materials

the electrons being grouped in pairs causing the magnetic moment to be cancelled by its neighbor.

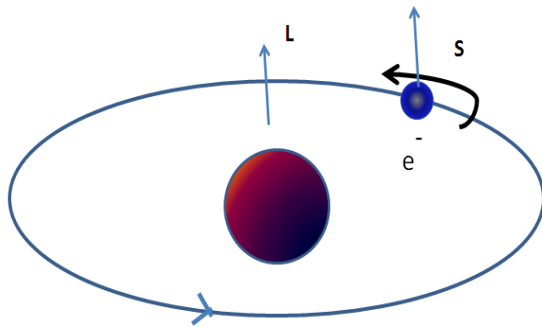


Fig. 2.1. A spin magnetic moment associated with it due to the electron itself spinning (like the earth on its own axis).

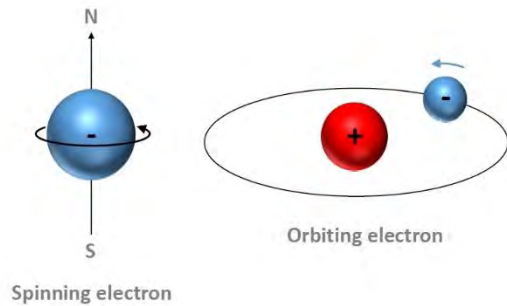


Fig. 2.2. Spinning electron on its own axis and orbiting electron around the nucleus (like the earth around the sun).

To produce a unified magnetic field in a certain magnetic material, the magnetic moments of a large proportion of the electrons aligned. The field produced in the material (or by an electromagnet) has a direction of flow and any magnet will experience a force trying to align it with an externally applied field, the smallest possible magnetic moment due to the spin of the electron is $\mu = \frac{e\hbar}{2m}$. According to quantum theory the spin of electrons has only two possibilities (+1/2 or -1/2). Similar to **equation (2.3)** we can write it in the form,

$$\mu = \left(\frac{e}{2m}\right)S \quad \dots \quad \dots \quad \dots \quad \dots \quad \dots \quad \dots \quad \dots \quad \dots \quad \dots \quad \dots \quad (2.4)$$

Where, 'S' is the spin quantum number here given by $\frac{1}{2} \hbar$.

In short,

$$\mu = g\left(\frac{e}{2m}\right)S \quad \dots \quad \dots \quad \dots \quad \dots \quad \dots \quad \dots \quad \dots \quad \dots \quad \dots \quad \dots \quad (2.5)$$

Here, 'g' is the term known as *g-factor*. When $g=2$, the spin contribution arises and when $g=1$, the orbital contribution arises. However, the magnetic moment contribution can be

by a bar magnet, at a given point in space, therefore depends on two factors:

- a) On the strength of its poles (P), and
- b) On the distance separating them (d).

The force is proportional to the following product,

$$\mu = PR \dots \dots \dots \dots \dots \dots \dots \dots \dots \dots \dots \dots \dots \quad (2.8)$$

Where ' μ ' describes the 'magnetic moment' or 'dipole moment' of the magnet along a distance ' R ' and its direction as the angle between ' R ' and the axis of the bar magnet. Magnetism can be created by the electric current in loops and coils so any current circulating in a planar loop produces a magnetic moment whose magnitude is equal to the product of the current and the area of the loop. When any charged particle is rotating, it behaves like a current loop with a magnetic moment.

The equation for the magnetic moment in the current-carrying loop, carrying current (I) and of area vector (a) for which the magnitude is given by,

$$\vec{\mu}_m = I\vec{a} \dots \dots \dots \dots \dots \dots \dots \dots \dots \dots \dots \dots \dots \quad (2.9)$$

Where ' $\vec{\mu}_m$ ' is the magnetic moment, a vector measured in ampere-square meters, or equivalent joules per tesla, ' I ' is the current, a scalar measured in amperes, and ' \vec{a} ' is the loop area vector, having as x , y , and z coordinates the area in square meters of the projection of the loop into the yz -, zx -, and xy -planes.

2.2.2 Magnetic moment of electrons

It is well known that the electron is a negatively charged particle with angular momentum. A rotating electrically charged body in classical electrodynamics causes a magnetic dipole effect creating magnetic poles of equal magnitude but opposite polarity like a bar magnet. For magnetic dipoles, the dipole moment points from the magnetic south to the magnetic north pole. The electron exists in a magnetic field which exerts a torque opposing its alignment creating potential energy that depends on its orientation with respect to the field. The magnetic energy of an electron is approximately twice what it should be in classical mechanics. The factor of two multiplying the electron spin angular momentum comes from the fact that it is twice as effective in producing magnetic moment.

This factor is called the electronic spin *g-factor*. The persistent early spectroscopists, such as Alfred Lande, worked out a way to calculate the effect of the various directions of angular momenta. The resulting geometric factor is called the *Lande g-factor*.

The intrinsic magnetic moment of a particle with charge (q), mass (m), and spin (s) is,

$$\vec{\mu}_m = g \left(\frac{e}{2m} \right) \vec{s} \quad \dots \quad \dots \quad \dots \quad \dots \quad \dots \quad \dots \quad \dots \quad \dots \quad \dots \quad \dots \quad (2.10)$$

Where the dimensionless quantity ‘ g ’ is called the *g-factor*.

The *g-factor* is an essential value related to the magnetic moment of the subatomic particles and corrects for the precession of the angular momentum. One of the triumphs of the theory of quantum electrodynamics is its accurate prediction of the electron *g-factor*, which has been experimentally determined to have the value 2.002319 . The value of 2 arises from the Dirac equation, a fundamental equation connecting the electron’s spin with its electromagnetic properties, and the correction of 0.002319 , called the anomalous magnetic dipole moment of the electron, arises from the electron’s interaction with virtual photons in quantum electrodynamics. Reduction of the Dirac equation for an electron in a magnetic field to its non-relativistic limit yields the Schrödinger equation with a correction term which takes account of the interaction of the electron’s intrinsic magnetic moment with the magnetic field giving the correct energy [5].

The total spin magnetic moment of the electron is,

$$\vec{\mu}_s = -g_s \mu_B \left(\frac{\vec{s}}{\hbar} \right) \dots \dots \dots \dots \dots \dots \dots \dots \dots \dots \dots \dots (2.11)$$

Where $g_s = 2$ in Dirac mechanics, but is slightly larger due to quantum electrodynamics effects, ‘ μ_B ’ is the Bohr magneton, and ‘ \vec{s} ’ is the electron spin (in vector form).

The z -component of the electron magnetic moment is,

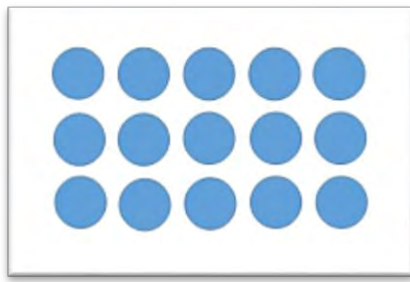
$$\vec{\mu}_z = -g_s \mu_B m_s \dots \dots \dots \dots \dots \dots \dots \dots \dots \dots \dots \dots (2.12)$$

Where ‘ m_s ’ is the spin quantum number.

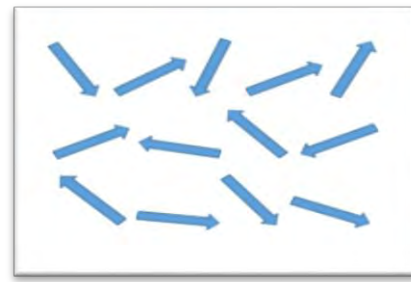
The total magnetic dipole moment due to orbital angular momentum in form of

2.4.1 Diamagnetism

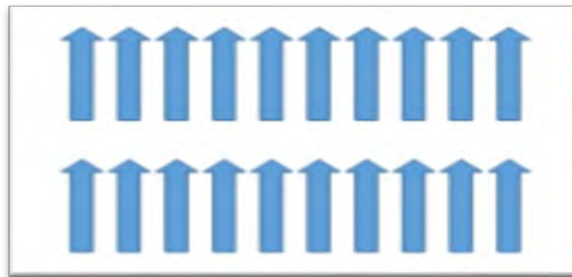
Diamagnetism is a fundamental property of all matter, although it is usually very weak. It is due to the non-cooperative behavior of orbiting electrons when exposed to an applied magnetic field. Diamagnetic substances are composed of atoms which have no net magnetic moments (i.e., all the orbital shells are filled and there are no unpaired electrons). However, when exposed to a field, a negative magnetization is produced and thus the susceptibility is negative. It obeys Lenz's law. The other characteristic behavior of diamagnetic materials is that the susceptibility is temperature independent. The typical value of susceptibility is on the order of 10^{-5} to 10^{-6} . Most of the materials are diamagnetic, including *Cu*, *B*, *S*, *N₂*, and most organic compounds.



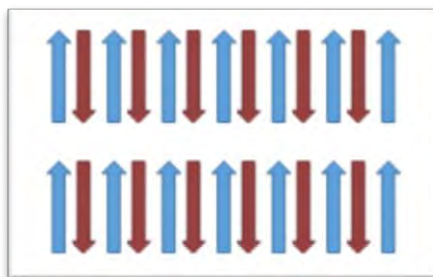
(a) Diamagnetism



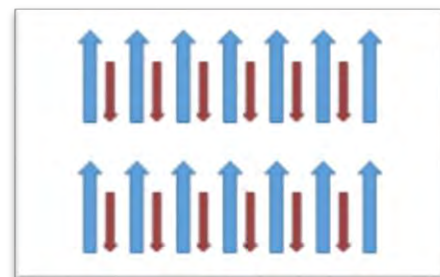
(b) Paramagnetism



(c) Ferromagnetism



(d) Antiferromagnetism



(e) Ferrimagnetism

Fig. 2.3. (a-e) Schematic diagrams of 5 (five) major magnetic materials based on their magnetic orderings.

Where ‘ C ’ is a constant and ‘ θ ’ is called Weiss constant.

For ferromagnetic materials, the Weiss constant is almost identical to the Curie temperature (T_C). At a temperature below T_C , the magnetic moments are ordered whereas above T_C , material loses magnetic ordering and shows paramagnetic character. The elements *Fe*, *Ni*, *Co*, and many of their alloys are typical ferromagnetic materials.

Two distinct characteristics of ferromagnetic materials are:

- a. Spontaneous magnetization and
- b. The existence of magnetic ordering temperature (Curie temperature).

The spontaneous magnetization is the net magnetization that exists inside a uniformly magnetized microscopic volume in the absence of a field. The magnitude of this magnetization, 0 K , is dependent on the spin magnetic moments of electrons. The saturation magnetization is the maximum induced magnetic moment that can be obtained in a magnetic field (H_{sat}); beyond this field, no further increase in magnetization occurs. Saturation magnetization is an intrinsic property, independent of particle size but dependent on temperature.

Even though electronic exchange forces in ferromagnets are very large, thermal energy eventually overcomes the exchange and produces a randomizing effect. This occurs at a particular temperature called the Curie temperature (T_C). Below the Curie temperature, the ferromagnet is ordered and above it, disordered. The saturation magnetization goes to zero at the Curie temperature. The Curie temperature is also an intrinsic property.

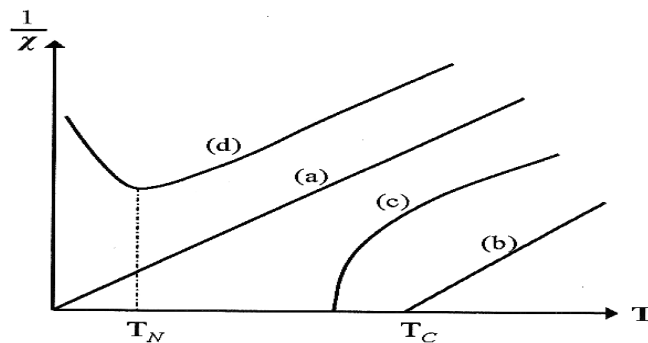


Fig. 2.4. The inverse susceptibility varies with temperature T for (a) Paramagnetic, (b) Ferromagnetic, (c) Ferrimagnetic, and (d) Antiferromagnetic materials. ‘ T_N ’ and ‘ T_C ’ are Néel temperature and Curie temperature, respectively.

2.4.4 Antiferromagnetism

Antiferromagnetic material aligns the magnetic moments in a way that all moments are anti-parallel to each other, the net moment is zero. The antiferromagnetic susceptibility is followed by the Curie-Weiss law with a negative ' θ ' as in **equation (2.21)**. The inverse susceptibility as a function of temperature is shown in **Fig. 2.4(d)**. Common examples of materials with antiferromagnetic ordering include *MnO*, *FeO*, *CoO*, and *NiO*.

However, imperfect antiferromagnetic form, which is referred to as *canted antiferromagnetism*, exhibits parasitic ferromagnetism which may result due to impurities or lattice defects, and by spin canting. The spins are not exactly anti-parallel and are inclined at a small angle, do not cancel out completely and thus results in spontaneous as well as remanent magnetizations. An important geological example is a hematite (α -*Fe₂O₃*), in which both the spin-canted and defect moments contribute to the ferromagnetic properties and another example is iron hydroxide (Goethite α -*FeOOH*).

2.4.5 Ferrimagnetism

Ferrimagnetic material has the same anti-parallel alignment of magnetic moments as an antiferromagnetic material does. However, the magnitude of the magnetic moment in one direction differs from that of the opposite direction. As a result, a net magnetic moment remains in the absence of an external magnetic field. The behavior of susceptibility of a ferrimagnetic material also obeys Curie-Weiss law and has a negative ' θ ' as well in **equation (2.21)** and shown in **Fig. 2.4(c)**. In ionic compounds, such as oxides, more complex forms of magnetic ordering can occur as a result of the crystal structure. The magnetic structure is composed of two magnetic sub-lattices (called *A* and *B*) separated by oxygens. The exchange interactions are mediated by the oxygen anions. When this happens, the interactions are called indirect or super-exchange interactions. The strongest super-exchange interactions result in an antiparallel alignment of spins between the *A* and *B* sub-lattices. In ferrimagnets, the magnetic moments of the *A* and *B* sub-lattices are not equal and result in a net magnetic moment. Ferrimagnetism is therefore similar to ferromagnetism. It exhibits all the hallmarks of ferromagnetic behavior like spontaneous magnetization, Néel temperature, hysteresis, and remanence. However, ferromagnets and ferrimagnets have a very different magnetic ordering.

2.5 Ferrites

Ferrites are ceramic materials that are dark grey or black in color [7]. They are divided into three sub-classes according to their crystal structures: spinels (cubic ferrites), magnetoplumbite (hexagonal ferrites), and Garnets (rare earth ferrites). The cubic ferrites are used as soft magnetic materials, whereas hexagonal ferrites are hard magnets exhibiting permanent magnetism. Garnets are utilized in high-frequency microwave applications [8]. These sub-classes are distinguished with respect to the molar ratio of Fe_2O_3 to the other oxide component within the ceramic as shown in **Table 2.1**.

Table 2.1. Summary of ferrite structure types, typified by changes in the Fe_2O_3 - MeO (or Me_2O_3) modifier oxide ratios [9].

Sl. No.	Types	Ferrites Name	Compositions	Comment(s)
i)	Spinet	Cubic	$1 Fe_2O_3-1 MeO$	Where MeO is a transition metal oxide
ii)	Magnetoplumbite	Hexagonal	$6 Fe_2O_3-1 MeO$	Where MeO is a divalent metal oxide from group IIA- BaO , CaO , SrO
iii)	Garnet	Rare earth	$5 Fe_2O_3-3 Me_2O_3$	Where MeO is a rare earth metal oxide

2.5.1 Soft magnetic materials (soft ferrites)

The wide variety of magnetic materials can be divided into two groups, the magnetically soft and the magnetically hard.

At high frequency metallic soft magnetic materials simply cannot be used due to the eddy current losses. Therefore, soft ferrites, which are ceramic insulators, become the most desirable material. These materials are ferrimagnetic with a cubic crystal structure and the general composition $MeO.Fe_2O_3$, where 'Me' is a transition metal such as nickel, manganese, magnesium or zinc [5]. The magnetically soft ferrites first came into commercial production in 1948.

Mn - Zn ferrite sold commercially as ferroxcube, can be used at frequencies up to

10 MHz, for example in telephone signal transmitters and receivers and in switch mode power supplies (also referred to as *dc-dc* converters). For these type of application, the driving force to increase frequency is to allow miniaturization.

Additionally, part of the family of soft ferrites, are the microwave ferrites, e.g. yttrium iron garnet. These ferrites are used in the frequency range from 100 MHz to 500 GHz, for waveguides for electromagnetic radiation and in microwave devices such as phase shifters.

2.5.2 Crystal structure of spinel ferrites

Ferrites have the cubic structure, which is very close to that of the mineral spinel $MgO.Al_2O_3$, and are called cubic spinel. Analogous to the mineral spinel, magnetic spinel have the general formula $MeO.Fe_2O_3$ or $MeFe_2O_4$ where 'Me' is the divalent metal ion [10]. This crystal structure was first determined by Bragg and by Nishikawa [4,11]. Formerly, spinels containing 'Fe' were called ferrites but now the term has been broadened to include many other ferrimagnets including garnets and hexagonal ferrites these need not necessarily contain iron. The spinel lattice is composed of a close-packed oxygen (radius about 0.13 nm) arrangement in which 32 oxygen ions form a unit cell that is the smallest repeating unit in the crystal network. The unit cell of the ideal spinel structures is given in Fig. 2.5. Between the layers of oxygen ions, if we simply visualize them as spheres, there are interstices that may accommodate the metal ions (radii ranging from 0.06 to 0.08 nm). Now, the interstices are not all the same: some which we call *A*-sites are surrounded by or coordinated with 4 nearest neighboring oxygen ions whose lines connecting their centers form a tetrahedron. Thus, *A*-sites are called tetrahedral sites. The other type of sites (*B*-sites) is coordinated by 6 nearest neighbor oxygen ions whose center connecting lines describe an octahedron. The *B*-sites are called octahedral sites. In the unit cell of 32 oxygen ions, there are 64 tetrahedral sites and 32 octahedral sites. If all these were filled with metal ions, of either +2 or +3 valence, the positive charge would be very much greater than the negative charge and so the structure would not be electrically neutral. It turns out that of the 64 tetrahedral sites, only 8 are occupied and out of 32 octahedral sites, only 16 are occupied. Thus the unit cell contains eight formula units AB_2O_4 , with 8 *A*-sites, 16 *B*-sites, and 32 oxygen ions, and a total of 56 (8×7) ions. A spinel unit cell contains two types of

sub cells, **Fig. 2.5**. The two types of sub-cells alternate in a three-dimensional array so that each fully repeating unit cell requires eight sub-cells, **Fig. 2.6**.

The positions of the ions in the spinel lattice are not perfectly regular (as the packing of hard spheres) and some distortion does occur. The tetrahedral sites are often too small for the metal ions so that the oxygen ions move slightly to accommodate them. The oxygen ions connected with the octahedral sites move in such a way as to shrink the size of the octahedral cell by the same amount as the tetrahedral site expands.

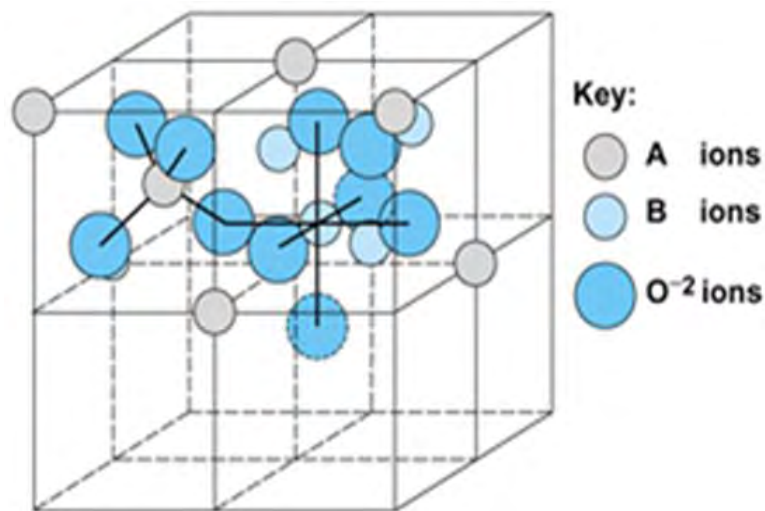


Fig. 2.5. Two sub-cells of a unit cell of the spinel structure.

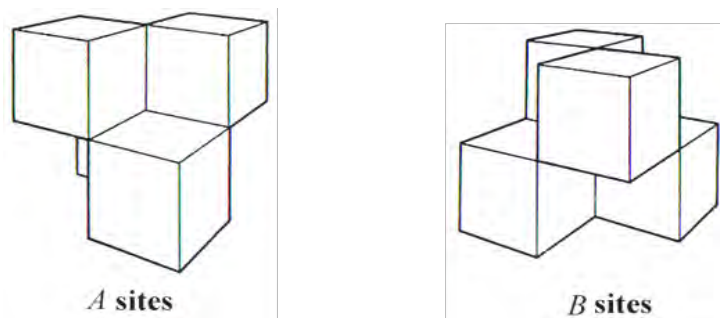


Fig. 2.6. A unit cell of spinel ferrite divided into eight sub-cells with *A*- and *B*-sites.

The movement of the tetrahedral oxygen is reflected in a quantity called the oxygen parameter, which is the distance between the oxygen ion and the face of the cube edge along the cube diagonal of the spinel sub-cell. This distance is theoretically equal to $\frac{3}{8}a_0$, where 'a₀' is the lattice constant [11].

2.5.3 Cation distribution of spinel ferrites

The cation distribution in the spinel ferrite $Me^{2+}Fe^{3+}O_4$ can be as follows [12,13]:

- *Normal spinel ferrite*

The Me^{2+} cations are in tetrahedral *A*-sites, while the two Fe^{3+} cations are in octahedral *B*-sites which are represented as $(Me^{2+})_A[Fe_2^{3+}]_BO_4$.

- *Inverse spinel ferrite*

In this case, the Me^{2+} cation and one of the Fe^{3+} cations are in octahedral *B*-sites while the second Fe^{3+} cation occupies tetrahedral *A*-sites. The arrangement is as $(Fe^{3+})_A[Me^{2+}Fe^{3+}]_BO_4$.

- *Mixed spinel ferrite*

The arrangement of the form $(Me_{1-\delta}^{2+}Fe_{\delta}^{3+})_A[Me_{1-x}^{2+}Fe_{1+x}^{3+}]_BO_4$ is often referred to as mixed spinel, where 'δ' is called the inversion parameter. $\delta=0$ for completely normal, $\delta=1$ for completely inverse spinel ferrites, and $0<\delta<1$ for mixed spinel ferrites.

The factors affecting the cation distribution over *A*- and *B*- sites are as follows [13,14]:

- The size of the cations,
- The electronic configurations of the cations,
- The electronic energy,
- The saturation magnetization of the lattice etc.

Smaller cations (trivalent) prefer to occupy the *A*-sites. The cations have a special preference for *A*- and *B*-sites and the preference depends on some factors, such as:

- Ionic radius,
- Size of interstices,
- Sintering temperature,
- Orbital preference for the specific coordination etc.

However, Zn^{2+} , Cd^{2+} , Ga^{2+} , In^{3+} , Ge^{2+} etc. have a strong preference for *A*-sites while Ni^{2+} , Cr^{3+} , Ti^{4+} , Sn^{4+} etc. have the preference for *B*-sites. Mg^{2+} , Fe^{3+} , Al^{3+} , Mn^{2+} , Cu^{2+} , Co^{2+} are distributed among *A*- and *B*-sites. Moreover, the electrostatic energy also affects the cation distribution in the spinel lattice.

Spinel oxides are ionic compounds and hence the chemical bonding occurring in them can be taken as purely ionic to a good approximation. The total energy involved, however, consists of the Coulomb energy, the Born repulsive energy, the polarization, and the magnetic interaction energy. The energy terms are all dependent on the lattice constant, the oxygen position parameter, and the ionic distribution. In principle, the equilibrium cation distribution can be calculated by minimizing the total energy with respect to these variables. But the only energy that can be written with any accuracy is the Coulomb energy. The individual preference of some ions for certain sites resulting from their electronic configuration also plays an important role. The divalent ions are generally larger than the trivalent (because the larger charge produces greater electrostatic attraction and so pulls the outer orbits inward). The octahedral sites are also larger than the tetrahedral. Therefore, it would be reasonable that the trivalent ions Fe^{3+} (0.067 nm) would go into the tetrahedral sites and the divalent ions Fe^{2+} (0.083 nm) go into the octahedral. Two exceptions are found in Zn^{2+} and Cd^{2+} which prefer tetrahedral sites because the electronic configuration is favorable for tetrahedral bonding to the oxygen ions. Thus Zn^{2+} (0.074 nm) prefer tetrahedral sites over the Fe^{3+} (0.067 nm) ions. Zn^{2+} (0.074 nm) and Ni^{2+} (0.077 nm) have almost the same ionic radius but *Zn* prefers tetrahedral sites and *Ni* prefers octahedral sites because of the configuration exception. Ni^{2+} (0.077 nm) and Cr^{3+} (0.064 nm) have strong preferences for octahedral sites [15-17]. In addition, Mn^{2+} (0.089 nm) has a strong preference for tetrahedral sites. Hence the factors influencing the distribution the cations among the two possible lattice sites are mainly their ionic radii of the specific ions, the size of the interstices, temperature, the matching of their electronic configuration to the

surrounding anions, and the electrostatic energy of the lattice, the so-called *Madelung energy*, which has the predominant contribution to the lattice energy under the constraint of overall energy minimization and charge neutrality.

2.6 Hysteresis loop

Hysteresis is the lagging of the magnetization of a ferromagnetic material behind the magnetizing force (H). A curve, or loop, plotted on B - H coordinates showing how the magnetization of a ferromagnetic material varies when subjected to a periodically reversing magnetic field, is called hysteresis loop.

By using a graph having B - H coordinates (or M - H coordinates), we can plot the hysteresis characteristics of a given ferromagnetic material. Such a curve with B - H coordinates is plotted in **Fig. 2.7** and it is known as the hysteresis loop. By periodically reversing a magnetizing force, we can plot the changing values of (B) within the material.

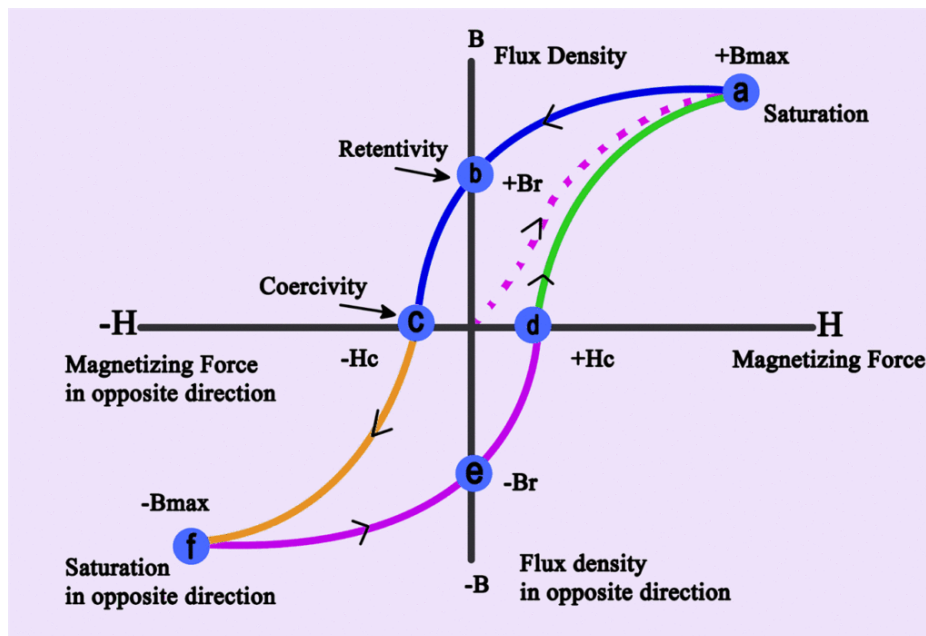


Fig. 2.7. Hysteresis loop

Actually, a hysteresis loop is a B - H curve under the influence of an *ac* magnetizing force. Values of flux density (B) are shown on the vertical axis and are in Tesla. Magnetizing force (H) is plotted on the horizontal axis.

2.6.1 Magnetization in the hysteresis loop

In **Fig. 2.7**, the specimen is assumed to be unmagnified, and the current is starting from zero in the center of the graph. As H increases positively, B follows the dotted curve from origin to saturation point 'a', indicated by ' B_{max} '. As H decreases to zero, the flux follows the curve 'ab' and drops to ' B_r ', which indicates the retentively or residual induction. This point represents the amount of flux remaining in the core after the magnetizing force is removed.

2.6.2 Demagnetization or degaussing in the hysteresis loop

Demagnetization or degaussing is the process by which the magnetization within the ferromagnetic materials is reduced to zero by exposing it to a strong alternating magnetic field that is gradually reduced to zero.

To demagnetize any magnetic material, we must reduce its residual magnetism (B_r) to zero. This can be done by connecting a suitable coil to a source of alternating current and placing it close to the object to be degaussed. Slowly moving the coil and object away from each other, causes the hysteresis loop to become progressively small. Finally, a point is reached where the loop is reduced to zero and no residual magnetism remains.

In **Fig. 2.7**, when ' H ' starts in the negative direction, the core will lose its magnetism, as shown by following the curve from point 'b' to 'c'. The amount of magnetizing force required to completely demagnetize the core is called the coercive force and is designated as ' $-H_c$ '. As the peak of the negative cycle is approached, the flux follows the portion of the curve labeled 'cd'. Point ' $-B_{max}$ ' represents saturation in the opposite direction from ' B_{max} '. From point 'd', the ' $-H$ ' value decreases to point 'e', which corresponds to a zero magnetizing force. Flux ' $-B_r$ ' still remains in the core.

A coercive force of ' $+H_c$ ' is required to reduce the core magnetization to zero. As the magnetic force continues to increase in the positive direction, the portion of the loop from point 'f' to 'a' is completed. The periodic reversal of the magnetizing force causes the core flux to repeatedly trace out the hysteresis loop.

2.6.3 Different magnetic properties in the hysteresis loop

From the hysteresis loop, we can conclude different magnetic properties of a material such as:

- i. **Reluctance:** The opposition that a magnetic circuit presents to the passage of magnetic lines through it.
- ii. **Retentivity:** The ability of a ferromagnetic material to retain residual magnetism is termed its retentivity.
- iii. **Residual magnetism:** The magnetism remaining after the external magnetizing force is removed.
- iv. **Coercive force:** The magnetic field strength required to reduce the residual magnetism to zero is termed the coercive force.
- v. **Permeability:** Permeability is the measure of the ease, with which magnetic lines of force pass through a given material.

2.7 Magnetic domains

Magnetic domain theory was developed by French physicist Pierre-Ernest Weiss [18]. In 1906 Weiss proposed that a magnetic material consists of physically distinct regions called domains and each of which was magnetically saturated in different directions (the magnetic moments are oriented in a fixed direction) as shown schematically in **Fig. 2.8**. Even each domain is fully magnetized but the material as a whole may have zero magnetization. The externally applied field aligns the domains, so there is a net moment. At low fields, this alignment occurs through the growth of some domains at the cost of less favorably oriented ones and the intensity of the magnetization increases rapidly. The growth of domains stops as the saturation region is approached and rotation of unfavorably aligned domain occurs. Domain rotation requires more energy than domain growth. In a ferromagnetic domain, there is a parallel alignment of the atomic moments. In a ferrite domain, the net moments of the antiferromagnetic interactions are spontaneously oriented parallel to each other. Domains typically contain from 10^{12} to 10^{18} atoms and are separated by domain boundaries or walls called Bloch walls. The formation of domains allows a ferro- or ferri-material to minimize its total magnetic energy [19].

$$E_k = K_1(\alpha_1^2 \alpha_2^2 + \alpha_2^2 \alpha_3^2 + \alpha_3^2 \alpha_1^2) + K_2(\alpha_1^2 \alpha_2^2 \alpha_3^2 + \dots \dots \dots \dots \dots) \quad (2.23)$$

Where, 'K' is the anisotropy constant, 'θ' is the angle between the easy axis and the direction of magnetization, and 'α₁', 'α₂', 'α₃' ... are the direction cosines, which are the ratios of the individual components of the magnetization projected on each axis divided by the magnitude of the magnetization. A crystal is higher in anisotropy energy when the magnetization points in the hard direction rather than in the easy direction. The formation of domains permits the magnetization to point along the easy axis, resulting in a decrease in the net anisotropy energy.

c) Magnetostrictive energy: In a magnetic field, the material may change its dimensions on the order of several parts per million. This change in dimension results in what is called magnetostrictive energy, which is dropped by a reduction in the size of the domains, requiring the formation of more domains.

d) Domain wall energy: This is energy resulting from the increase or decrease in the width of the walls due to the growth or shrinkage of domains. The magnetization in a domain changes by two mechanisms: rotation of the magnetic dipoles toward the direction of the applied field and change in the domain volume. In the first case, a certain amount of anisotropy energy is needed to rotate the magnetization in a crystal from the easy to another axis. In the second mechanism, the volume of the domain changes, changing its contribution to the bulk magnetization, while the magnetization direction is unchanged. The change in the magnetization intensity of a domain depends on how close its direction is to the direction of the applied field. If the magnetization direction is close, the intensity in the domain increases, whereas if it is far, the intensity decreases.

The domain volume changes due to the motion of the domain wall. This movement is originated by a torque that rotates the moments of the domain in line with the field, moving the center of the wall toward the domain opposed to the field. Consequently, the volume of the domains whose direction is favorable is increased whereas the domains with unfavorable direction decrease in volume [8]. In order to explain the fact that ferromagnetic materials with spontaneous magnetization could exist in the demagnetized state Weiss proposed the concept of magnetic domains. The magnetization within the domain is saturated and will always lie in the easy direction of magnetization when there

is no externally applied field. The direction of the domain alignment across a large volume of material is more or less random and hence the magnetization of a specimen can be zero.

Magnetic domains exist in order to reduce the energy of the system. A uniformly magnetized specimen as shown in **Fig. 2.9(a)** has large magneto-static energy associated with it. This is the result of the presence of magnetic free poles at the surface of the specimen generating a demagnetizing field (H_d). From the convention adopted for the definition of the magnetic moment for a magnetic dipole the magnetization within the specimen points from the South Pole to the North Pole, while the direction of the magnetic field points from north to south. Therefore, the demagnetizing field is in opposition to the magnetization of the specimen. The magnitude of H_d is dependent on the geometry and magnetization of the specimen. In general, if the sample has a high length to diameter ratio (and is magnetized in the long axis) then the demagnetizing field and the magneto-static energy will be low.

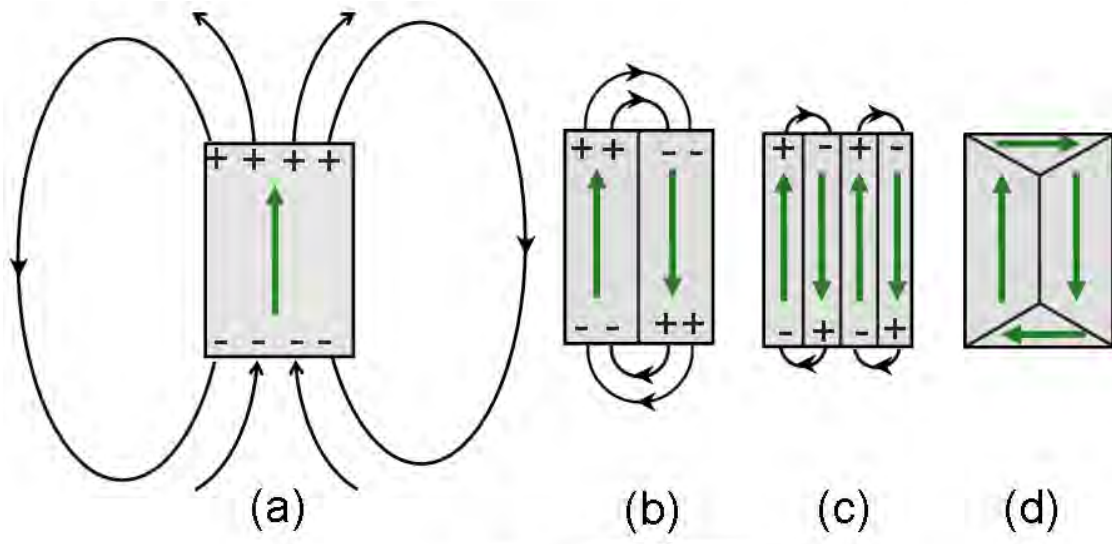


Fig. 2.9. Schematic illustration of the breakup of magnetization into domains: (a) Single domain, (b) Two domains, (c) Four domains, and (d) Closure domains.

The breakup of the magnetization into two domains as illustrated in **Fig. 2.9(b)** reduces the magneto-static energy by half. In fact, if the magnet breaks down into ' N ' domains then the magneto-static energy is reduced by a factor of ' $1/N$ ', hence **Fig. 2.9(c)** has a quarter of the magneto-static energy of **Fig. 2.9(a)**.

Fig. 2.9(d) shows a closure domain structure where, the magneto-static energy is zero, this is only possible for materials that do not have a strong uniaxial anisotropy, and the neighboring domains do not have to be at 180° to each other.

2.7.1 Structure of domain wall

The overall energy of the system is raised by introducing a domain. The division into domains only keeps up while the minimization in magneto-static energy is larger than the energy required to form the domain wall. The energy related to a domain wall is proportional to the area of the domain wall. In the domain wall, the dipole moments of the atoms are not pointing in the easy direction of magnetization and hence are in a higher energy state, which is illustrated in Fig. 2.10. In addition, the exchange energy is also raised within the wall because of the atomic dipoles within the wall are not at 180° to each other.

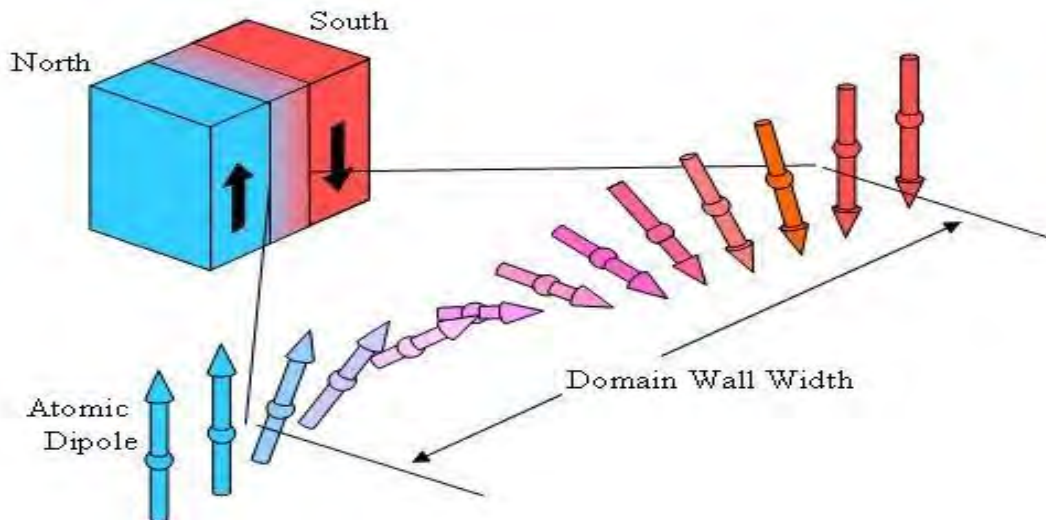


Fig. 2.10. Schematic representation of a 180° domain wall.

Therefore, the domain wall energy is an intrinsic property of a material, which depends on:

- a) Degree of magneto-crystalline anisotropy and
- b) Strength of the exchange interaction between neighboring atoms.

The thickness of the domain wall will also vary in relation to these parameters. The

narrower wall is because of strong magneto-crystalline anisotropy, whereas the wider wall is for a strong exchange interaction between neighboring atoms.

However, within a specimen, minimum energy can be obtained with a specific number of domains. This number of domains will depend on the size and shape of the sample (which will affect the magneto-static energy) and the intrinsic magnetic properties of the material (which will affect the magneto-static energy and the domain wall energy). Ferromagnetic materials get their magnetic properties not only because of their atoms to carry a magnetic moment but also because the material is made up of small regions known as magnetic domains. In each domain, all of the atomic dipoles are coupled together in a preferential direction. During solidification, a trillion or more atom moments are aligned parallel so that the magnetic force within the domain is strong in the same direction.

Ferromagnetic materials are said to be characterized by ‘spontaneous magnetization’ since they obtain saturation magnetization in each of the domains without an external magnetic field is applied. Even though the domains are magnetically saturated, the bulk material may not show any signs of magnetism because the domains develop themselves and are randomly oriented relative to each other. Ferromagnetic materials become magnetized when the magnetic domains within the material are aligned. This can be done by placing the material in a strong external magnetic field or by passing electrical current through the material. Some or all of the domains can become aligned. The more domains that are aligned, the stronger the magnetic field in the material. When all of the domains are aligned, the material is said to be magnetically saturated. When a material is magnetically saturated, no additional amount of external magnetization force will cause an increase in its internal level of magnetization. In an un-magnetized sample of material, there is no overall magnetization of the sample; because the domains are pointed in random directions, or form closed loops. In a magnetized sample of material, a strong overall magnetism is produced by the combination of magnetic effects of the aligned domains.

2.8 Microstructure of magnetic materials

A polycrystalline material is much more than many tiny crystals bonded together. The interfaces between the crystals, or the grain boundaries which separate and bond the grains, are complex and interactive interfaces. The whole set of a given material’s

properties (mechanical, chemical, and especially electro-magnetic) depend strongly on the nature of the microstructure.

In the simplest case, the grain boundary is the region, which accommodates the difference in crystallographic orientation between the neighboring grains. For certain simple arrangements, the grain boundary is made of an array of dislocations whose number and spacing depends on the angular deviation between the grains. The ionic nature of ferrites leads to dislocation patterns considerably more complex than in metals since electrostatic energy accounts for a significant fraction of the total boundary energy [5].

For low-loss ferrite, Ghate states that the grain boundaries influence properties by [6]:

- a) Creating a high resistivity inter-granular layer,
- b) Acting as a sink for impurities which may act as a sintering aid and grain growth modifiers,
- c) Providing a path for oxygen diffusion, which may modify the oxidation state of cations near the boundaries.

In addition to grain boundaries, ceramic imperfections can impede domain wall motion and thus reduce the magnetic property. Among these are pores, cracks, inclusions, second phases, as well as residual strains. Imperfections also act as energy wells that pin the domain walls and require higher activation energy to detach. Stresses are microstructural imperfections that can result from impurities or processing problems such as too rapid a cool. They affect the domain dynamics and are responsible for a much greater share of the degradation of properties than would expect [6].

Grain growth kinetics depends strongly on the impurity content. A minor dopant can drastically change the nature and concentration of defects in the matrix, affecting grain boundary motion, pore mobility, and pore removal [5]. The effect of a given dopant depends on its valence and solubility with respect to the host material. If it is not soluble at the sintering temperature, the dopant becomes a second phase which usually segregates to the grain boundary.

At microwave frequency, and also in low anisotropic amorphous materials, dB and dH may be in different directions, the permeability thus a tensor character. In the case of amorphous materials containing a large number of randomly oriented magnetic atoms, the permeability will be scalar. As we have the **equation (2.15)** of magnetic induction (B). Now the susceptibility,

$$\chi = \frac{dM}{dH} = \frac{d}{dH} \left(\frac{B}{\mu_0} - H \right) = \frac{1}{\mu_0} (\mu - 1) \quad \dots \dots \dots \quad (2.25)$$

Again, the magnetic energy density,

$$E = \frac{1}{\mu_0} \int H dB \quad \dots \dots \dots \quad (2.26)$$

For time-harmonic fields, $H = H_0 \sin \omega t$, the dissipation can be described by a phase difference (δ) between H and B . In the case of permeability, defined as the proportional constant between the magnetic field induction (B) and applied field intensity (H), as **equation (2.16)**.

If a magnetic material is subjected to an *ac* magnetic field as we get,

$$B = B_0 e^{i\omega t} \quad \dots \dots \dots \quad (2.27)$$

Then it is observed that the magnetic flux density (B) experiences a delay. This is caused due to the presence of various losses and is thus expressed as,

$$B = B_0 e^{i(\omega t - \delta)} \quad \dots \dots \dots \quad (2.28)$$

Where ' δ ' is the phase angle and marks the delay of B with respect to H , the permeability is then given by,

$$\mu = \frac{B}{H} = \frac{B_0 e^{i(\omega t - \delta)}}{H_0 e^{i\omega t}} = \frac{B_0 e^{-i\delta}}{H_0} = \frac{B_0}{H_0} \cos \delta - i \frac{B_0}{H_0} \sin \delta = \mu' - i\mu'' \quad \dots \dots \quad (2.29)$$

Where $\mu' = \frac{B_0}{H_0} \cos \delta \dots \dots \dots \quad (2.30)$

And $\mu'' = \frac{B_0}{H_0} \sin \delta \dots \dots \dots \quad (2.31)$

The real part (μ') of complex permeability (μ) as expressed in **equation (2.30)** represents the component of induction (B), which is in phase with H , so it corresponds to the normal permeability.

If there are no losses, we should have ' $\mu = \mu'$ '. The imaginary part (μ'') corresponds to that part of B , which is delayed by phase ' δ ' from H . The presence of such a component requires a supply of energy to maintain the alternation magnetization, regardless of the origin of delay. It is useful to introduce the magnetic loss factor or loss tangent ($\tan\delta_M$).

The ratio of μ'' to μ' , as is evident from equation gives,

$$\frac{\mu''}{\mu'} = \frac{\frac{B_0}{H_0} \sin \delta}{\frac{B_0}{H_0} \cos \delta} = \tan \delta \dots \dots \dots (2.32)$$

This ' $\tan\delta$ ' is called the loss factor (also known as magnetic loss factor or loss tangent ' $\tan\delta_M$ ').

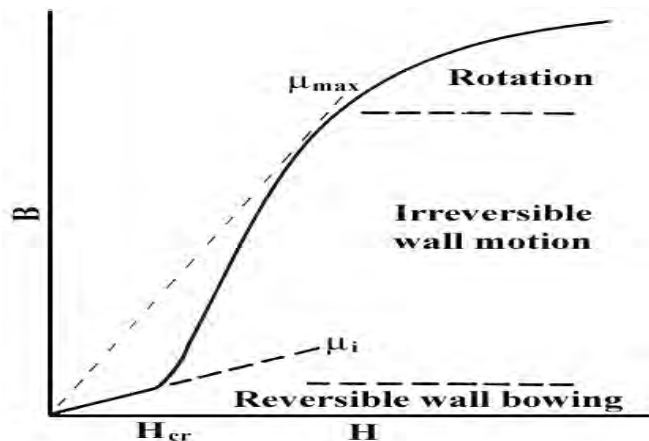


Fig. 2.13. Schematic magnetization curve showing initial permeability ' μ_i ' (the slope of the curve at low fields) and the main magnetization mechanism in each magnetization range.

The Q -factor or quality factor is defined as the reciprocal of this loss factor i.e.

$$\text{Quality factor (or } Q \text{- factor)} = \frac{1}{\tan \delta_M} \dots \dots \dots (2.33)$$

$$\text{And, the relative quality factor, } RQF = \frac{\mu'}{\tan \delta_M} \quad \dots \quad \dots \quad \dots \quad \dots \quad (2.34)$$

The behavior of μ' versus frequency and μ'' versus frequency is known as the complex permeability spectrum. The combined effect of the wall permeability and rotational permeability mechanism is referred to as the initial permeability of a ferromagnetic substance. A Schematic magnetization curve showing the initial permeability μ_i and the main magnetization mechanism in each magnetization range is presented in **Fig. 2.13**.

2.9.1 Mechanisms of permeability

A demagnetized magnetic material is divided into the number of Weiss domains separated by Bloch walls. In each domain, all the magnetic moments are oriented in parallel and the magnetization has its saturation value ' M_S '. In the walls, the magnetization direction changes gradually from the direction of magnetization in one domain to that in the next.

The equilibrium positions of the walls result from the interactions with the magnetization in neighboring domains and from the influence of pores; crystal boundaries and chemical in-homogeneities which tend to favor certain wall positions. This is the explanation of the mechanisms of the permeability of magnetic materials.

2.9.2 Wall permeability

The mechanism of wall permeability arises from the displacement of the domain walls in small fields. Let us consider a piece of material in the demagnetized state, divided into Weiss domains with equal thickness ' L ' by means of 180° Bloch walls (as in **Fig. 2.14**). The walls are parallel to the yz -plane. The magnetization (M_S) in the domains is oriented alternately in the $+z$ - or $-z$ -direction. When a field H with a component in the $+z$ direction is applied, the magnetization in this direction will be favored. A displacement ' dx ' of the walls in the direction shown by the dotted lines will decrease the energy density by the amount mentioned hereafter [21],

Now, we obtain the following equation,

$$\chi_w = \frac{(\Delta M)_\theta}{H} = \frac{4M_s^2 \cos^2 \theta}{KL} \quad \dots \quad \dots \quad \dots \quad \dots \quad \dots \quad \dots \quad \dots \quad \dots \quad \dots \quad (2.41)$$

2.9.3 Rotational permeability

The rotational permeability mechanism arises from the rotation of the magnetization in each domain. The direction of M can be found by minimizing the magnetic energy (E) as a function of the orientation. The major contribution to E comes from the crystal anisotropy energy. Other contributions may be due to the stress and shape anisotropy. The stress may influence the magnetic energy via the magnetostriction. The shape anisotropy is caused by the boundaries of the sample as well as by pores, non-magnetic inclusions, and in-homogeneities. For small angular deviations, ' α_x ' and ' α_y ' may be written as,

$$\alpha_x = \frac{M_x}{M_s} \quad \dots \quad \dots \quad \dots \quad \dots \quad \dots \quad \dots \quad \dots \quad \dots \quad \dots \quad \dots \quad (2.42)$$

$$\text{And } \alpha_y = \frac{M_y}{M_s} \quad \dots \quad \dots \quad \dots \quad \dots \quad \dots \quad \dots \quad \dots \quad \dots \quad \dots \quad \dots \quad (2.43)$$

For equilibrium z-direction, E may be expressed as [3,22],

$$E = E_0 + \frac{1}{2} \alpha_x^2 E_{xx} + \frac{1}{2} \alpha_y^2 E_{yy} \quad \dots \quad \dots \quad \dots \quad \dots \quad \dots \quad \dots \quad \dots \quad \dots \quad \dots \quad (2.44)$$

Where it is assumed that x - and y - are the principal axes of the energy minimum. Instead of ' E_{xx} ' and ' E_{yy} ', the anisotropy field ' H_x^A ' and ' H_y^B ', are often introduced. Their magnitude is given by,

$$H_x^A = \frac{E_{xx}}{2M_s} \quad \dots \quad \dots \quad \dots \quad \dots \quad \dots \quad \dots \quad \dots \quad \dots \quad \dots \quad \dots \quad (2.45)$$

$$\text{And } H_y^A = \frac{E_{yy}}{2M_s} \quad \dots \quad \dots \quad \dots \quad \dots \quad \dots \quad \dots \quad \dots \quad \dots \quad \dots \quad \dots \quad (2.46)$$

If the shape and stress anisotropies cannot be neglected, H^A will be larger. Any estimate of χ_r will then be rather uncertain as long as the domain structure and the pore distribution in the material are not known. A similar estimate of χ_w would require knowledge of the stiffness parameter (K) and the domain width (L).

These parameters are influenced by such factors as imperfection, porosity, and crystallite shape and distribution which are essentially unknown.

2.10 Interaction between magnetic moments on lattice sites

Spontaneous magnetization of spinels (at 0 K) can be estimated on the basis of their composition, cation distribution, and the relative strength of the possible interaction. Since cation-cation distances are generally large, direct (ferromagnetic) interactions are negligible. Because of the geometry of orbital involved, the strongest super-exchange interaction is expected to occur between octahedral and tetrahedral cations.

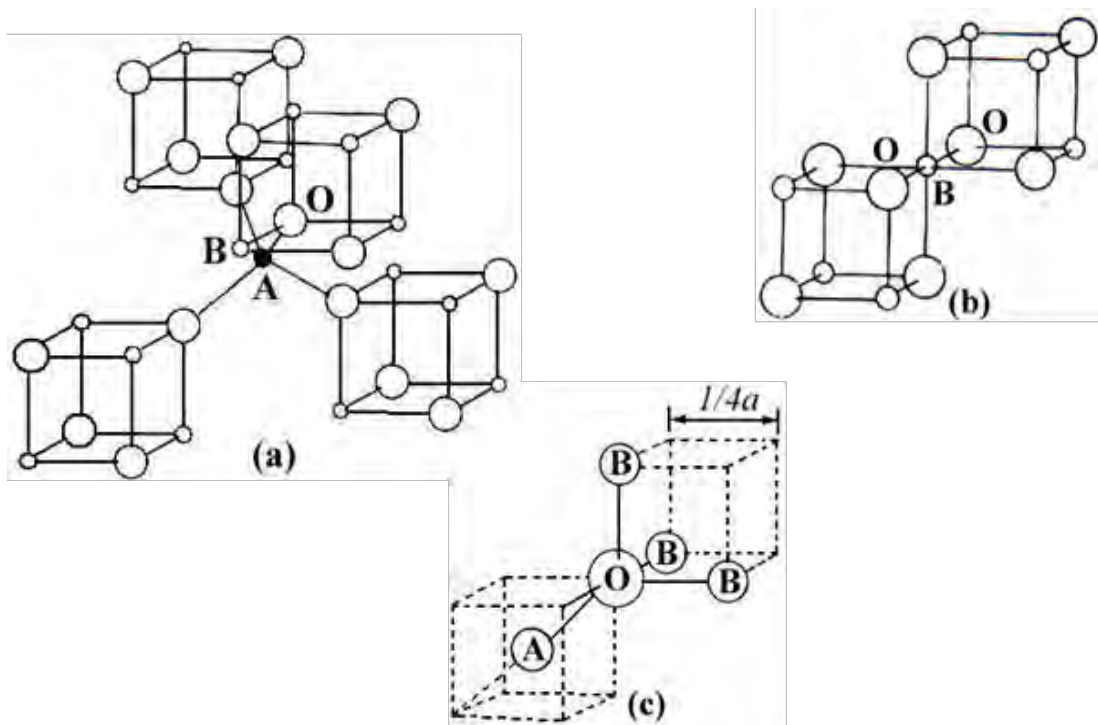


Fig. 2.15. Schematic diagram of nearest neighbors of (a) a tetrahedral site, (b) an octahedral site, and (c) an anion site.

The strength of interaction or exchange force between the moments of the two metal ions on different sites depends on the distances between these ions and the oxygen ion that links them and also on the angle between the three ions. The nearest neighbors of a tetrahedral, an octahedral and an anion site are shown in **Fig. 2.15**. The interaction is greatest for an angle of 180° and also where the interionic distances are the shortest.

Fig. 2.16 shows the interionic distances and the angles between the ions for the different type of interactions. In the $A-A$ and $B-B$ cases, the angles are too small or the distances between the metal ions and the oxygen ions are too large. The best combination of distances and angles are found in $A-B$ interactions.

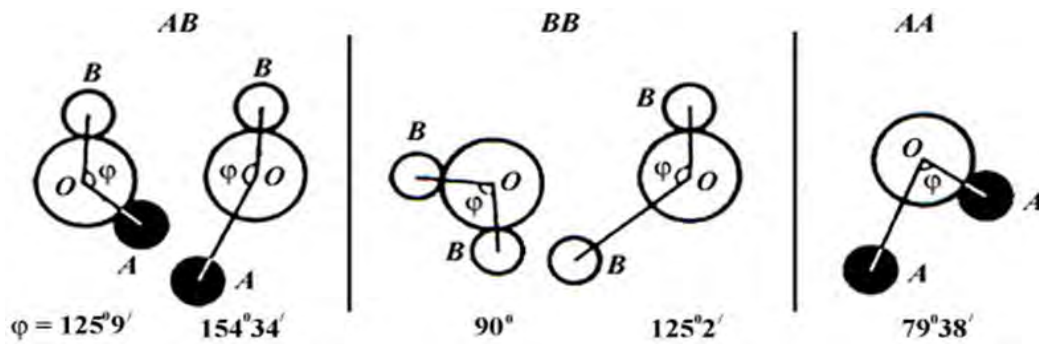


Fig. 2.16. Interionic angles in the spinel structure for the different type of lattice site interactions.

For an undistorted spinel, the $A-O-B$ angles are about 125° and 154° [3,23-24]. The $B-O-B$ angles are 90° and 125° but the latter, one of the $B-B$ distances is large. In the $A-A$ case, the angle is about 80° . Therefore, the interaction between moments on the A - and B -site is strongest. The $B-B$ interaction is much weaker and the most unfavorable situation occurs in the $A-A$ interaction.

By examining the interaction involving the major contributor, or the $A-B$ interaction which orients the unpaired spins of these ions antiparallel, Néel was able to explain the ferrimagnetism of ferrites.

2.11 Magnetic exchange interaction

The exchange energy between the two atoms having spins ' S_i ' and ' S_j ' can be expressed universally in terms of Heisenberg Hamiltonian [25],

$$H = - \sum J_{ij} S_i S_j \quad \dots \quad \dots \quad \dots \quad \dots \quad \dots \quad \dots \quad \dots \quad \dots \quad \dots \quad (2.52)$$

Where ' J_{ij} ' the exchange integral represents the strength of the exchange coupling between the spin angular momentum ' i ' and ' j '. It is well known that the favored situation is the one with the lowest energy and there are two ways in which the wave functions can combine for lowering the energy by ' H '. These are:

If ' J_{ij} ' is positive, the parallel spin configuration will minimize the system total energy and all spins aligned to each other in the ground state. This is the case leading to ferromagnetic ordering.

If ' J_{ij} ' is negative, ' J_{ij} ' favors the antiparallel alignment of spins and consequently gives rise to antiferromagnetic ordering.

2.11.1 Super-exchange interaction

The magnetic interaction in magnetic oxide (ferrites) cannot be explained on the basis of direct exchange interaction because of the following facts:

- The magnetic ions are located too far apart from each other shielded by the nonmagnetic anion (oxygen). This is because these are not band type semiconductor. The non-magnetic anion is situated in the line joining magnetic cations.
- Super-exchange interactions appear, i.e., indirect exchange via anion p -orbitals that may be strong enough to order the magnetic moments.

Ferrimagnetic oxides are one kind of magnetic systems in which there exist at least two equivalent sub-lattices for the magnetic ions. The antiparallel alignment between these sub-lattices (ferrimagnetic ordering) may occur provided the inter-sub-lattice exchange interactions are antiferromagnetic (AF) and some requirements concerning the signs and

strengths of the intra-sub-lattice interactions are fulfilled. Since usually in ferrimagnetic oxides, the magnetic cations are surrounded by bigger oxygen anions (almost excluding the direct overlap between cation orbitals) magnetic interactions occur via indirect super-exchange mediated by the ‘*p*’ oxygen orbitals.

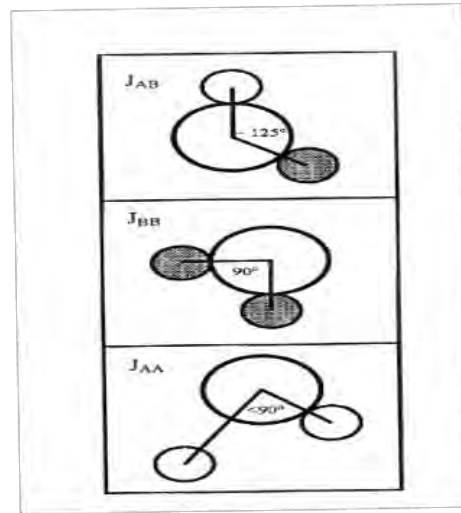


Fig. 2.17. Three major types of super-exchange interactions in spinel ferrites are as follows: ‘ J_{AB} ’, ‘ J_{BB} ’, and ‘ J_{AA} ’. The small empty circle is *A*-site, the small solid circle is *B*-site, and the large empty circle is oxygen anion.

It is well known that the sign of these super-exchange interactions depends both on the electronic structure of the cations and their geometrical arrangement (**Fig. 2.17**). In most of the ferrimagnetic oxides, the crystallographic and electronic structure give rise to antiferromagnetic inter and intra-sub-lattice competing interactions. The magnitude of negative exchange energies between two magnetic ions ‘*M*’ and ‘*M*’ depends upon the distances from these ions to the oxygen ion O^{2-} , via which the super-exchange takes place, and on the angle $M-O^2-M'$ (φ). According to the super-exchange theory, the angle $\varphi=180^\circ$ gives rise to the greatest exchange energy, and this energy decreases very rapidly as the distance between the ions increases.

If *A*- and *B*- are the tetrahedral and octahedral ions respectively in a spinel structure, the *A*-*B* interaction is the greatest and *A*-*A* exchange interaction is the weakest [25-27].

2.12 Two sub-lattices in spinel ferrites

The term ‘magnetic sub-lattice’ is widely used in the study of magnetic structures of the whole spectrum of magnetic materials. In the case of ferromagnetic materials, the ‘magnetic sub-lattice’ is exactly the same as the crystal structure and no problem arises. In the case of antiferromagnetic, the importance of the direction of the magnetic moments is evident and makes clear the existence of two magnetic sub-lattices, as for example, in *MnO*. The difference between the two magnetic sub-lattices is the direction of their magnetic moment. However, ferrimagnetic materials are considerably more complex and the application of the molecular field theory to spinels has pointed to the problem of a clear definition of the concept of magnetic sub-lattices. In spinel ferrites, the metal ions are separated by the oxygen ions and the exchange energy between spins of neighboring metal ions is found to be negative, that is, antiferromagnetic. This is explained in terms of super-exchange interaction of the metal ions via the intermediate oxygen ions [25,28].

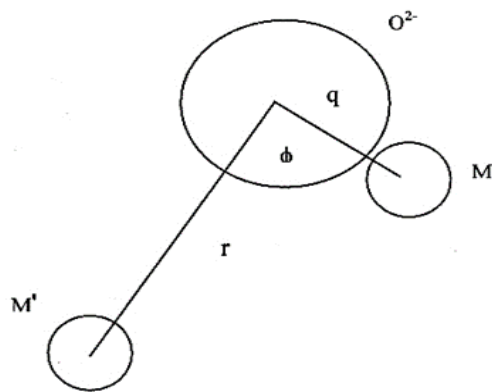


Fig. 2.18. Schematic representation of ions ‘*M*’ and ‘*M*’ and the O^{2-} ion through which super-exchange is made. ‘*r*’ and ‘*q*’ are the center to center distances from ‘*M*’ and ‘*M*’ respectively to O^{2-} and ‘ ϕ ’ is the angle between ‘*M*’ and ‘*M*’.

There are a few points to line out about the interaction between two ions in tetrahedral *A*-sites:

- The distance between two *A*-ions (~ 0.35 nm) is very large compared with their ionic radius (0.067 nm for Fe^{3+}),

- The angle $A-O^2-A$ ($\varphi=79^\circ38'$) is unfavorable for super-exchange interaction,
- The distance from one A -ion to O^2- is not the same as the distance from the other A -ion to O^2- as there is only one A -nearest neighbor to an oxygen ion (in **Fig. 2.18**, ' M ' and ' M ' are A -ions, $r=0.33$ nm and $q=0.17$ nm). As a result, two nearest A -ions are connected via two oxygen ions.

These considerations led us to the conclusion that super-exchange interaction between A -ions is very unlikely. This conclusion together with the observation that direct exchange is also unlikely in this case to support the assumption that $J_{AA}=0$ in the spinel ferrites. According to Néel's theory, the total magnetization of a ferrite divided into two sub-lattices A and B is,

$$M_T(T) = M_B(T) - M_A(T) \dots \dots \dots \dots \dots \dots \dots \dots \dots \dots \quad (2.53)$$

Where ' T ' is the temperature, ' $M_B(T)$ ' and ' $M_A(T)$ ' are A - and B - sub-lattice magnetizations. Both ' $M_B(T)$ ' and ' $M_A(T)$ ' are given in terms of the Brillouin function ' $B_{si}(x_i)$ ',

$$M_B(T) = M_B(T=0) B_{sB}(x_s) \dots \dots \dots \dots \dots \dots \dots \dots \dots \dots \quad (2.54)$$

$$M_A(T) = M_A(T=0) \dots \dots \dots \dots \dots \dots \dots \dots \dots \dots \quad (2.55)$$

$$\text{With } \chi_B = \frac{\mu_B g_A S_A}{k_B T} M_B N_{AB} \dots \dots \dots \dots \dots \dots \dots \dots \dots \dots \quad (2.56)$$

$$\text{And } \chi_B = \frac{\mu_B g_B S_B}{k_B T} (M_B N_{BB} + M_A N_{AB}) \dots \dots \dots \dots \dots \dots \dots \dots \dots \dots \quad (2.57)$$

The molecular field coefficients ' N_{ij} ', are related to the exchange constants ' J_{ij} ' by the following expression,

$$J_{ij} = \frac{n_j g_i g_j \mu_B^2}{2z_{ij}} N_{ij} \dots \dots \dots \dots \dots \dots \dots \dots \dots \dots \quad (2.58)$$

With ' r_{ij} ' the number of magnetic ions per mole in the j^{th} sub-lattice, ' g ' the Lande factor, ' μ_B ' is the Bohr magneton and ' z_{ij} ' the number of nearest neighbors on the j^{th} sub-lattice that interact with the i^{th} ion.

According to Néel's theory and using $J_{AA}=0$, equating the inverse susceptibility $1/\chi=0$ at $T=T_c$, we obtain for the coefficients of the molecular field theory ' N_{AB} ' and ' N_{BB} ' of the following expression,

$$N_{BB} = \frac{T_C}{C_B} - \frac{C_A N_{AB}^2}{T_C} \dots \dots \dots \dots \dots \dots \dots \dots \dots \dots \dots \dots \quad (2.59)$$

Where ' C_A ' and ' C_B ' are the Curie constants for each sub-lattice. **Equations (2.53) & (2.59)** constitute a set of equations with two unknown, N_{AB} and N_{BB} , provided that M_A and M_B are a known function of temperature (T).

2.13 Magnetic structure of substituted ferrites

Analysis and characterization of substituted ferrites are vary from the application point of view of materials. In this case, collinear and non-collinear models are related to the magnetic structure of substituted ferrites. These are presented hereafter in next two sub-sections.

2.13.1 Néel's collinear model

Soft ferrites belong to the cubic spinel structure. According to Néel's theory, the magnetic ions are assumed to be distributed among the tetrahedral A -and octahedral B -sites of the spinel structure. The magnetic structure of such crystals essentially depends upon the type of magnetic ions residing on the A -and B -sites and the relative strengths of inter- (J_{AB}) and intra-sub-lattice exchange interactions (J_{AA} , J_{BB}). Negative exchange interactions exist between A - A , A - B , and B - B ions. When A - B antiferromagnetic interaction is the dominant one, A - and B - sub-lattices will be magnetized in opposite direction below a transition temperature. When the A - A (or B - B) interaction is dominant, Néel found that the above transition will not take place and he concluded that the substance remains paramagnetic down to the lower temperature. But this conclusion was not correct as, in the presence of strong interactions, some kind of order may be expected to occur at a low temperature as claimed by Yafet and Kittel (Y - K) [29].

2.13.2 Non-collinear model

In general, all the interactions are negative (antiferromagnetic) with $|J_{AB}| \gg |J_{BB}| \gg |J_{AA}|$. In such a situation, collinear or Néel type of order is obtained. Yafet and Kittel (*Y-K*) theoretically considered the stability of the ground state of magnetic ordering, taking all the three exchange interactions into account and concluded that beyond a certain value of J_{BB}/J_{AB} , the stable structure was a non-collinear triangular configuration of the moment wherein the *B*-site moments are oppositely canted relative to the *A*-site moments. Later on Leyons et al. extending these theoretical considerations showed that for normal spinel the lowest energy corresponds to conical spinel structure for the value of $3J_{BB}S_B/2J_{AB}S_A$ greater than unity. Initially one can understand why the collinear Néel structure gets perturbed when J_{BB}/J_{AB} increases. Since all these three exchange interactions are negative (favoring antiferromagnetic alignment of moments) the inter- and intra-sub-lattice exchange interaction compete with each other in aligning the moment direction in the sub-lattice. This is one of the origins of topological frustration in the spinel lattice. By selective magnetic directions of say, *A*-sub-lattice one can effectively decrease the influence of J_{AB} vis-a-vis J_{BB} and thus perturb the Néel ordering. The first neutron diffraction study of such system i.e., $Zn_xNi_{1-x}Fe_2O_4$ was done at Trombay and it was shown to have the *Y-K* type of magnetic ordering followed by Néel ordering before passing on to the paramagnetic phase [30-33].

It was found that ferrites which have been substituted sufficiently with non-magnetic atoms showed significant departure from Néel collinear model. These theoretical models have been used to explain these departures:

- A paramagnetic center model in which the number of magnetic nearest neighbors determines whether a magnetic ion remains paramagnetic or contributes to the magnetization,
- A uniform spin canting relative to the average magnetization, and
- A localized canting where the canting angle of a magnetic ion spin depends on the local magnetic environment.

The discrepancy in the Néel's theory was resolved by Yafet and Kittel (*Y-K*) [33] and they formulated the non-collinear model of ferrimagnetism. They concluded that the ground state at '*0 K*' might have one of the configuration mentioned hereafter:

- Have an antiparallel arrangement of the spins on two sites,
- Consists of triangular arrangements of the spins on the sub-lattices,
- An antiferromagnetic in each of the sites separately.

2.14 Conduction mechanism in ferrites

Ferrites are ferromagnetic semiconductors that could be used in electronic devices. The increasing demand for low loss ferrites resulted in detailed investigations on conductivity and on the influence of various substitutions on the electrical conductivity, thermoelectric power, etc. The conduction mechanism in ferrites is quite different from that in semiconductors. In ferrites, the temperature dependence of mobility affects the conductivity and the carrier concentration is almost unaffected by temperature variation. In semiconductors, the band type conduction occurs, wherein ferrites, the cations are surrounded by closed pack oxygen anions and as a first approximation can well be treated as isolated from each other. There will be a little direct overlap of the anion charge clouds or orbital. In other words, the electrons associated with particular ion will largely remain isolated and hence a localized electron model is more appropriate than a collective electron (band) model. This accounts for the insulating nature of ferrites. These factors led to the hopping electron model. An appreciable conductivity in these ferrites is found to be due to the presence of iron ion ions with different valence states at crystallographically different equivalent lattice sites. Conduction is due to exchange of $3d$ electron, localized at the metal ions, from Fe^{3+} to Fe^{2+} . Various models have been suggested to account for the electrical properties. These are as follows [23,34-38]:

- *Hopping model of electrons:* In ferrites, there is a possibility in exchanging valency of a considerable fraction of metal ions and especially that of iron. The temperature dependence of conductivity arises only due to mobility and not due to the number of charge carriers in the sample.
- *Small polaron model:* A small polaron is a defect occurred when an electronic carrier becomes trapped at a given site as a consequence of the displacement of adjacent atoms or ions. The entire defect then migrates by an activated hopping mechanism.

- [3] Kittel, C. (1996) *Introduction to Solid State Physics*, 7th edition, Jhon Wiley & Sons, Inc., New York.
- [4] Cullity, B. D. (1972) *Introduction to Magnetic Materials*, Addison-Wiley Publishing Company, Inc., California.
- [5] Valenzuela, R. (1994) *Magnetic Ceramics*, Cambridge University Press, Cambridge.
- [6] Callister, W. (2003) *Materials Science and Engineering an introduction*, Sixth edition, JoHn Wiley & Sons, Inc., New York.
- [7] Snelling, E. C. (1969) *Soft ferrites: Properties and Applications*, First edition, Life Books Ltd., London.
- [8] Heck, C. (1974) *Magnetic Materials and Their Applications*, Butterworths, London.
- [9] Buchanan, R. C. ed. (2004) *Ceramic Materials for Electronics*, Marcel Dekker Inc., New York.
- [10] Chougule, S. S., and Chougule, B. K., "Response of Dielectric Behaviour on Ferroelectric rich (y) $\text{Ni}_{0.8}\text{Zn}_{0.2}\text{Fe}_2\text{O}_4+(1-y)$ PZT ME Composites," *Mat. Chem. and Phy.*, vol.108, pp. 408-412, 2007.
- [11] Goldman, A. (1999) *Handbook of Modern Ferromagnetic Materials*, Kulwer Acad. Pub., Boston.
- [12] Sharma, J. K., Srivastava, P., Singh, G., and Virk, H. S., "Nanoferrites of transition metals and their catalytic activity," *Ferrites and Ceramics II. Solid State Phenomena Series*, vol. 241, pp. 126-138, 2016.
- [13] Goldman, A. (1990) *Modern Ferrite Technology*, Van Nostrand Reinhold, New York.
- [14] Morrison, S. A., Cahill, C. L., Carpenter, E. E., Calvin, S., Swaminathan, R., McHenry, M. E., and Harris, V. G., "Magnetic and structural properties of nickel zinc ferrite nanoparticles synthesized at room temperature," *Journal of Applied Physics*, vol. 95(11), pp. 6392-6395, 2004.
- [15] Chukalkin, Y. G., Shtirts, V. R., "Magnetic state of ZnFe_2O_4 ," *Phys. Solid State (Fiz. Tverd. Tela)*, vol. 30, pp. 2919-2923, 1988.
- [16] Kumar, A., Kumar, P., Rana, G., Yadav, M. S., and Pant, R. P., "A study on structural and magnetic properties of $\text{Ni}_x\text{Zn}_{1-x}\text{Fe}_2\text{O}_4$ ($0.1 \leq x \leq 0.6$) ferrite nanoparticles," *Appl. Sci. Letter.*, vol. 1, pp. 33-36, 2015.
- [17] Li, O. A., Lin, C. R., Chen, H. Y., Hsu, H. S., Shih, K. Y., Edelman, I. S., Wu, K. W., Tseng, Y. T., Ovchinnikov, S. G., and Lee, J. S., "Size dependent magnetic and magneto-optical properties of $\text{Ni}_{0.2}\text{Zn}_{0.8}\text{Fe}_2\text{O}_4$ nanoparticles," *Journal of Magnetism and Magnetic Materials*, vol. 408, pp. 206-212, 2016.
- [18] Weiss, P., "La variation du ferromagnétisme avec la temperature," *Comptes Rendus*, vol. 143, pp. 1136-1139, 1906.

- [19] Cullity, Graha, C. D. (2008) *Introduction to Magnetic Materials, 2nd edition*, Wiley-IEEE, New York. ISBN: 0-471-47741-9.
- [20] Spaldin, N. (2003) *Magnetic materials: Fundamentals and device applications*, Cambridge University Press, Cambridge.
- [21] Snoek, J. L., "Dispersion and absorption in magnetic ferrites at frequencies above one Mc/s," *Physica*, vol. 14(4), pp. 207-217, 1948.
- [22] Hossain, A. K. M. A., Seki, M., Kawai, T., and Tabata, H., "Colossal magneto-resistance in spinel type $Zn_{1-x}Ni_xFe_2O_4$," *Journal of Applied Physics*, vol. 96(2), pp. 1273-1275, 2004.
- [23] Li, Y. J., Chen, X. M., and Tang, Y. H., "Magneto-electric Effect in $Ni_{0.8}Zn_{0.2}Fe_2O_4/Sr_{0.5}Ba_{0.5}Nb_2O_6$ composites," *Journal of the European Ceramic Society*, vol. 26, pp. 2839-2844, 2006.
- [24] Zhai, J., Cai, N., Shi, Z., Lin Y., and Nan, C. W., "Magnetic- Dielectric Properties of $NiFe_2O_4/PZT$ Particulate composites," *Journal of Physics D: Applied Physics*, vol. 37, pp. 823-827, 2004.
- [25] Smit, J., and Wijn, H. P. J. (1959) *Ferrites*, Philips Technical Library, Eindhoven, Netherlands.
- [26] Viswanathan, B., and Murthy, V. R. K. (1990) *Ferrite Materials Science and Technology*, Springer Verlag, Noarosa Publishing House, New Delhi.
- [27] Fuentes, V., Aburto, S., and Valenzuela, R., "Magnetic sublattices in nickel ferrite," *J. Mag. Mag. Mater.*, vol. 69(3), pp. 233-236, 1987.
- [28] Anderson, P. W. (1963) *Magnetism, Vol-1*, Eds. G. T. Rado and H. Suhl, Academic Press, New York.
- [29] Leyons, D. H., Keplan, T. A., Dwight, K., and Menyuk, N., "Classical theory of the ground spin-state in cubic spinets," *Phys. Rev.*, vol. 126(2), p. 540, 1962.
- [30] Murthy, N. S. S., Natera, M. G., Youstif, S. I., Begum, R. J., and Srivatava, C. M., "Yafet-Kittel angles in Zinc-Nickel ferrites," *Phys. Rev.*, vol. 181(2), p. 969, 1969.
- [31] Nogues, M., Dorman, J. L., Teillet, T., and Villers, G., "Randomly canted structures in the ferrite $Zn_xMg_{1-x}Fe_2O_4$," *J. Mag. Mag. Mater.*, vol. 415, pp. 104-107, 1992.
- [32] Samokhvalov, A. A., and Rustamov, A. G., "*Fiz. Tverd. Tela*," *Soviet Physics- Solid State*, vol. 6, p. 749, 1964.
- [33] Yafet, Y., and Kittel, C., "Antiferromagnetic arrangements in ferrites," *Phys. Rev.*, vol. 87(2), p. 290, 1952.
- [34] Bossmann, A. J., and Crevecoeur, C., "Mechanism of the electrical conduction in Li-doped NiO," *Phys. Rev.*, vol. 144(2), p. 763, 1966.

- [35] Jonker, G. H., Santen, J. H. V., “Magnetic compounds with perovskite structure III ferromagnetic compounds of cobalt,” *Physica*, vol. 19, pp. 120-130, 1953.
- [36] Bhise, B. V., Ghatage, A. K., Kulkarni, B. M., Lotka, S. D., and Patil, S. A., “Conduction in Mn substituted Ni-Zn ferrites,” *Bulletin of Material Science*, vol. 19(3), pp. 527-531, 1996.
- [37] Patil, M. G., Mahajan, V. C., Bhise, B. V., Chendke, S. M., and Patil, S. A., “Conduction phenomenon in Mn-substituted NiCd ferrites,” *Physica Status Solidi (a)*, vol. 144(2), pp. 415-420, 1994.
- [38] Jalaiah, K., and Babu, K. V., “Structural, magnetic and electrical properties of nickel doped Mn-Zn spinel ferrite synthesized by sol-gel method,” *Journal of Magnetism and Magnetic Materials*, vol. 423, pp. 275-280, 2017.

.....

CHAPTER 3

SYNTHESIS AND STRUCTURAL CHARACTERIZATION

Sample preparation techniques of ferrite materials including their goal are briefly discussed in this chapter. The procedure of auto-combustion technique to achieve ferrite nanoparticle is explained here properly. Flow-chart of the stages in the preparation of spinel ferrite as well as image diagram to prepare present samples are also presented here. This chapter also includes short notes on calcination, pressing, sintering, and thermal etching.

3.1 Goal to ferrite sample preparation

The formation of the spinel structure is a goal common to all the ferrites. It is still a complex and difficult task to prepare polycrystalline composite with optimum desired properties. Knowledge and control of the chemical composition, homogeneity, and microstructure are very crucial. As most of the properties needed for composite applications are not intrinsic but extrinsic, preparation of samples has to encounter added complexity. It is well known that almost all composites decompose at the elevated temperature if we want to melt them under normal conditions.

Four basic steps in the preparation of ferrite are mentioned below:

- a) Preparation of materials to form an intimate mixture with the metal nitrate in the ratio which they will have in the final product;
- b) Heating of this mixture to form the ferrite (often called calcining);
- c) Grinding the calcined powders and pressing the fine powders into the required shape; and
- d) Sintering to produce a highly dandified product.

3.2 Sample preparation techniques

It is well known that solid state reaction technique is the most popular conventional ceramic process which is applied to assure the majority of ferrite powders.

However, ferrite developed by a ceramic method involves high calcination temperature synthesis for the completion of solid-state reaction between the constituent oxides or carbonates and the particles are obtained rather bigger and non-uniform in size. These non-uniform particles, on compacting, result in the formation of voids and subsequently the low density ferrites. In order to overcome these drawbacks, wet chemical methods, viz. co-precipitation, hydrothermal processing, combustion, etc. had been used. Most of the non-conventional processes are involved in producing the ferrite powder by a wet method. Among these methods, some are listed below [1,2]:

- a) Co-precipitation;
- b) Organic precursors;
- c) Sol-gel synthesis;
- d) Spray-drying;
- e) Freeze-drying;
- f) Glass crystallization;
- g) Combustion synthesis etc.

Nowadays, to achieve fine ferrite nanoparticles, auto-combustion synthesis is often applied. In this present research work, auto-combustion method is used to get nanocrystalline ferrites. Auto-combustion technique has the following features over other techniques:

- a) Faster heating rate and shorter reaction time;
- b) Use of relatively simple equipment with low cost;
- c) Formation of high-purity products;
- d) Production of homogeneous, fine, and reproducible ferrites etc.

In the next section (**section 3.3**), a brief description of auto-combustion synthesis is given.

3.3 Auto-combustion synthesis

Combustion method, a novel method for preparation of fine particles of ferrites makes use of the strongly exothermic reaction between metal nitrate and fuel. In this processes, the stoichiometric ratio of nitrates is dissolved in the minimum amount of ethanol in a glass beaker and starrier it until all the nitrate salts completely soluble in the ethanol. Then the mixed solution evaporated on a constant temperature water bath.

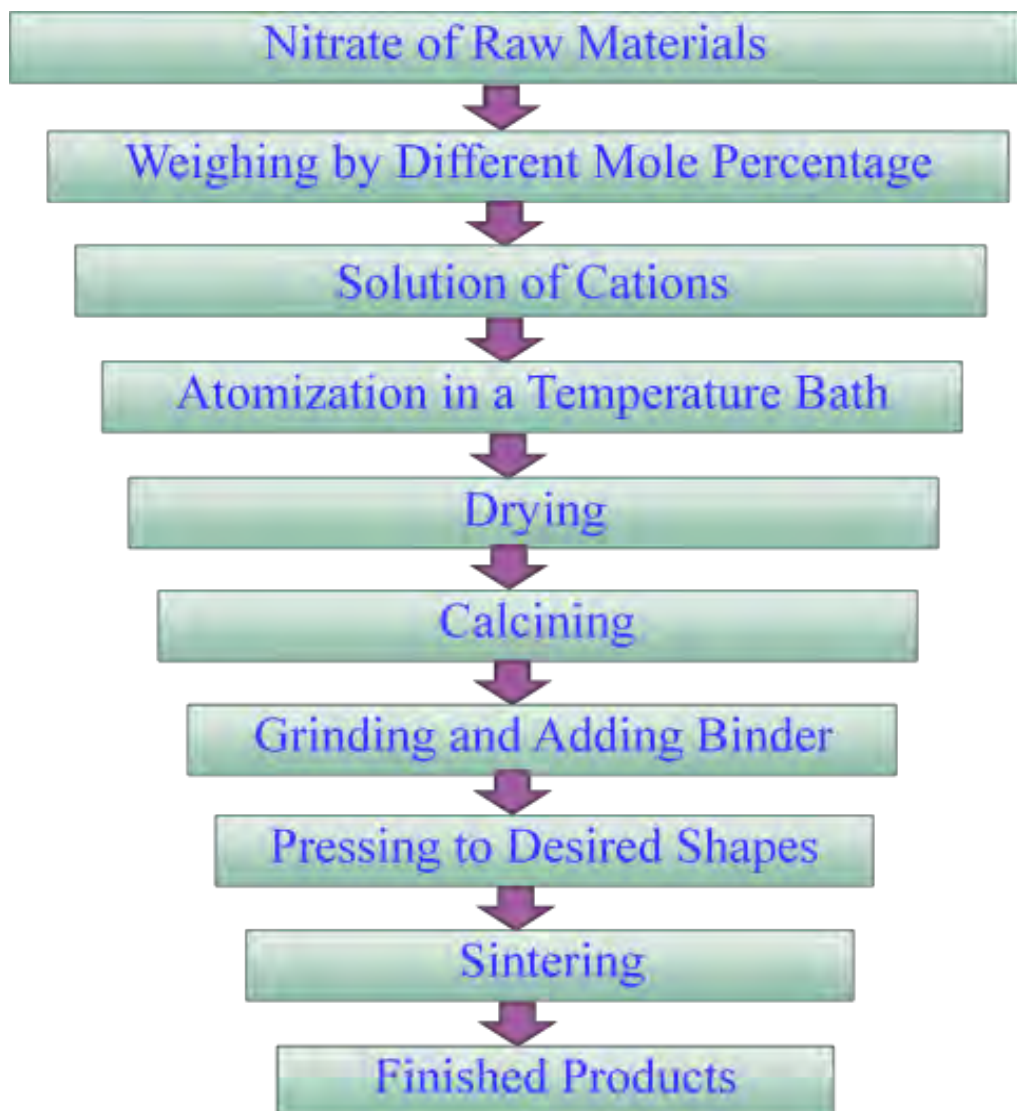


Fig. 3.1. Flow-chart of the stages in the preparation of spinel ferrite.

After boiling and ignition of the mixture, a spinel residue is obtained in a few minutes. A heating rate of at least 348 K/min is used to obtain good combustion. These powders are crushed and ground thoroughly. Low-temperature calcinations are also performed. The calcined powders are again crushed into fine powders. The pellet and toroid-shaped samples are prepared from these calcined powders using die-punch assembly or hydrostatic or isostatic pressure. Sintering is carried out, at the temperature ranging $1473\text{-}1623\text{ K}$, for times of typically $1\text{-}40\text{ h}$, and in various atmospheres (e.g. air, O_2 or N_2) [3-9]. The stages followed in ferrite preparation are schematically presented in Fig. 3.1.

3.4 Calcination, pressing, sintering, and thermal etching

Calcination, pressing, sintering, and thermal etching processes have a very important role in the preparation of ferrite samples. Short notes on these techniques are described in the following sub-sections (**sub-sections 3.4.1-3.4.4**).

3.4.1 Calcination

The calcining process can be repeated several times to obtain a high degree of homogeneity. The calcined powders are crushed into fine powders. The ideal characteristics of fine powders are [2]:

- a) Small particle size (sub-micron);
- b) Narrow distribution in particle size;
- c) Dispersed particles;
- d) The equiaxed shape of particles;
- e) High purity; and

f) Homogeneous composition.

A small particle size of the reactant powders provides a high contact surface area for initiation of the reaction; diffusion paths are shorted, leading to more efficient completion of the reaction. Porosity is easily eliminated if the initial pores are very small. Narrow size distribution of spherical particles as well as a dispersed state is important for compaction of the powder. Grain growth during sintering can be better controlled if the initial size is small and uniform.

3.4.2 Pressing

A binder is usually added prior to compaction, at a concentration lower than 5wt % [2]. Binders are polymers or waxes; the most commonly used binder in ferrite is polyvinyl alcohol (PVA). The binder facilitates the particles flow during compacting and increases the bonding between the particles, presumably by forming bonds of the type particle-binder-particle. During sintering, binders decompose and are eliminated from the ferrite. Pressures are used for compacting very widely but are commonly several tons per square inch (i. e., up to 10^8 Nm^{-2}).

3.4.3 Sintering

Sintering is defined as the process of obtaining a dense, tough body by heating a compacted powder for a certain time at a temperature high enough to significantly promote diffusion, but clearly lower than the melting point of the main component. The driving force for sintering is the reduction in surface free energy of the powder. Part of this energy is transferred into interfacial energy (grain boundaries) in the resulting polycrystalline body [2,8]. The sintering time, temperature, and the furnace atmosphere play a very important role on the magnetic property of ferrite materials. The purposes of the sintering process are mentioned below:

- a. To bind the particles together so as to impart sufficient strength to the product;
- b. To densify the material by eliminating the pores; and
- c. To homogenize the materials by completing the reactions left unfinished in the calcining step.

- a) Low sintering temperature excluding O_2 (Vacuum, argon, nitrogen); and
- b) A high temperature in pure oxygen to reduce Zn loss.

Accordingly, other properties correlated along with density:

- a) The lattice constant is greater for O_2 but smaller for vacuum;
- b) Curie temperature is greater for the vacuum but smaller for O_2 ; and
- c) Resistivity is greater for O_2 but smaller for vacuum.

3.4.4 Thermal etching

Thermal etching is the process to achieve an accurate surface for further investigation of the samples after the investigation of bulk density. Basically, it is performed at a fixed temperature, below the least sintering temperature for 2~3 hours. This process is required for polished disk-shaped samples, to regain their accurate surface after polishing by emery papers.

However, an ultrasonic bath for 5~15 minutes is essential for all disk-shaped samples to remove dust from their surface after investigating surface morphology by field emission scanning electron microscopy (FESEM) device.

3.5 Composition of the studied ferrite

Manganese substituted microstructural and electro-magnetic properties of nanocrystalline $Li-Ni-Zn$ ferrites are synthesized and thoroughly investigated in this present research.

This investigation mainly focused on the following ferrites:

$Li_{0.15}Ni_{0.30-x}Mn_xZn_{0.40}Fe_{2.15}O_4$ (where $x=0.00, 0.03, 0.06, 0.09, 0.12, \text{ and } 0.15$).

3.6 Synthesis of present nanoparticles

The $Li_{0.15}Ni_{0.30-x}Mn_xZn_{0.40}Fe_{2.15}O_4$ have been prepared by auto-combustion technique. Stoichiometric amounts (*Appendix-A*) of commercially available $LiNO_3$ ($\geq 99\%$), $Ni(NO_3)_2 \cdot 6H_2O$ ($\geq 98.5\%$), $MnCl_2 \cdot 4H_2O$ ($\geq 99\%$), $Zn(NO_3)_2 \cdot 6H_2O$ ($\geq 98\%$), $Fe(NO_3)_3 \cdot 9H_2O$ ($\geq 98\%$), and citric acid ($C_6H_8O_7$) (99%) was dissolved in distilled water. The *pH* value of the solution was adjusted to about 7 by using ammonia solution. The solution was heated at temperature of 353 K to transform into gel then auto-combustion occurred and fluffy nano-sized loose powders was formed.



Fig. 3.3. Steps in preparation of present spinel ferrite samples.

These nano-sized powders (like ashes), achieved from auto-combustion synthesis, then crushed (by foil paper) to get semi-fine nanoparticles. These semi-fine nanoparticles then crushed and ground thoroughly in a mortar with the pestle to achieve fine nanoparticles (**Fig. 3.3**).

These fine nanoparticles of various compositions are then calcined at 1173 K temperature for 5 hours (*this is an optional action for ferrite nanoparticles by auto-combustion synthesis, not shown in Fig. 3.3*) for the final formation of $Li_{0.15}Ni_{0.30-x}Mn_xZn_{0.40}Fe_{2.15}O_4$ nanoparticles.

3.7 Preparation of the present samples

Fine nanoparticles are granulated using polyvinyl alcohol (*PVA*) as a binder and pressed into the disk- and toroid-shaped samples (**Fig. 3.4**). The samples are sintered at various sintering temperatures (*1373*, *1423*, *1473*, and *1523 K*) in air for *4~5 hours*. The temperature ramps for sintering are *5 K/min* for heating and *10 K/min* for cooling.



Fig. 3.4. (a) Disk and (b) Toroid shaped samples.

Emery papers were used to polish all disk- and toroid-shaped samples. Thermal etching was performed at *1273 K* for *2~3 hours* for all disk-shaped samples to achieve accurate surface to investigate surface morphology of the samples. After investigation of surface morphology by field emission scanning electron microscopy (*FESEM*) device, an ultrasonic bath was performed for all disk-shaped samples for *5~15 minutes* to remove dust from the surface of the samples.

References:

- [1] Goldman, A. (1999) *Handbook of Modern Ferromagnetic Materials*, Kulwer Acad. Pub., Boston.
- [2] Valenzuela, R. (1994) *Magnetic Ceramics*, Cambridge University Press, Cambridge.
- [3] Li, O. A., Lin, C. R., Chen, H. Y., Hsu, H. S., Shih, K. Y., Edelman, I. S., Wu, K. W., Tseng, Y. T., Ovchinnikov, S. G., and Lee, J. S., "Size dependent magnetic and magneto-optical properties of $\text{Ni}_{0.2}\text{Zn}_{0.8}\text{Fe}_2\text{O}_4$ nanoparticles," *Journal of Magnetism and Magnetic Materials*, vol. 408, pp. 206-212, 2016.
- [4] Hossain, A. K. M. A., *Investigation of colossal magnetoresistance in bulk and thick film magnetites*, Ph. D. Thesis, Imperial College, London, 1998.
- [5] Cullity, B. D. (1972) *Introduction to Magnetic Materials*, Addison-Wisley Publishing Company, Inc., California.

- [6] Brook, R. J. (1991) *Sintering: An Overview*, Concise Encyclopedia of Advanced Ceramic Materials, Pergamon Press, Oxford.
- [7] Reijnen, P. (1967) *Science of Ceramics*, Academic Press, London.
- [8] Hossain, A. K. M. A., Biswas, T. S., Mahmud, S. T., Yanagida, T., Tanaka, H., and Kawai, T., "Enhancement of initial permeability due to Mn substitution in polycrystalline $\text{Ni}_{0.50-x}\text{Mn}_x\text{Zn}_{0.50}\text{Fe}_2\text{O}_4$," *Journal of Magnetism and Magnetic Materials*, vol. 321(2), pp. 81-87, 2009.
- [9] Kingery, W. D., Bowen, H. K., and Uhlman, D. R. (1976) *Introduction to Ceramics, 2nd edition*, Wiley Interscience, New York.
- [10] Coble, R. L., and Burke, J. E., "Sintering of crystalline solids," in *4th Int. Symposium on the Reactivity of Solids, Amsterdam*, vol. 1, pp. 38-51 (1960).
- [11] Mc-Cole, I. J., and Clark, N. J. (1988) *Forming, Shaping and Working of high Performance Ceramics*, Blackie, Glasgow.

.....

CHAPTER 4

EXPERIMENTAL TECHNIQUES

This chapter basically focused on various experimental techniques which are applied in this research work to characterize the samples. XRD is used for phase identification which is explained here including experimental techniques to measure the lattice parameters and average crystallite size. The technique that is used to analyze surface morphology is also described here. This chapter also provides frequency dependent ac permeability measurement methods for ferrite samples. Description of the experimental techniques for the measurement of temperature dependent initial permeability and Néel temperature are presented here. A brief analysis of measuring the electrical properties of the samples is also included here.

4.1 Study of X-ray diffraction

X-ray diffraction (XRD) patterns of these ferrite samples of $Li_{0.15}Ni_{0.30-x}Mn_xZn_{0.40}Fe_{2.15}O_4$ (where $x=0.00, 0.03, 0.06, 0.09, 0.12$, and 0.15) obtained by using an advanced X-ray diffractometer (*model-Philips PANalytical X'PERT-PRO*) equipped with $Cu-K_{\alpha}$ as a target ($\lambda=0.1540598$ nm).

4.1.1 Phase identification by XRD

The energy of the X-ray remains unchanged in Bragg's reflection, which is referred to as coherent elastic scattering. If a beam of monochromatic radiation with wavelength ' λ ' is incident on a periodic crystal plane at an angle ' θ ' and is diffracted at the same angle as illustrated in **Fig. 4.1**, the Bragg diffraction condition for X-rays is given by the equation displayed below,

$$2d \sin\theta = n\lambda \quad \dots \quad \dots \quad \dots \quad \dots \quad \dots \quad \dots \quad \dots \quad \dots \quad \dots \quad \dots \quad (4.1)$$

Where ' d ' is the distance between crystal planes and ' n ' is the positive integer which represents the order of reflection. **Equation (4.1)** is known as 'Bragg's law'. This law suggests that diffraction is only possible when $d \geq \lambda/2$ [1]. That's why we can't use the

visible light to determine the crystal structure of a material. *XRD* provides substantial information on the crystal structure. Sharp peaks of *XRD* are analyzed to identify the phase of the present compositions comparing with characteristic reflections of earlier reported compositions.

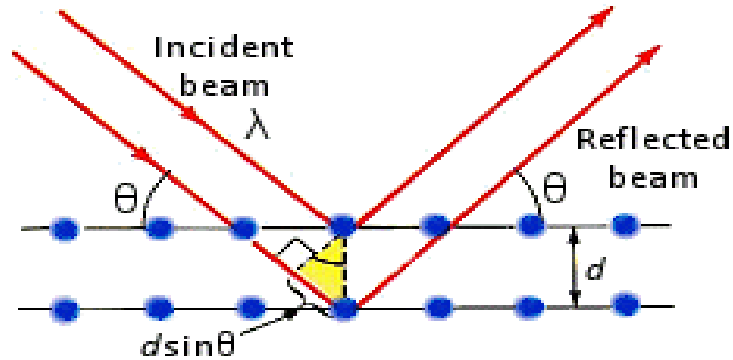


Fig. 4.1. Bragg's law of diffraction.

4.1.2 Crystallite size measurement

Determination of crystallite size is important in the ferrite nanoparticles. Significant fine particle broadening is observed in the Bragg peaks, due to their small particle size. A crystal is usually considered perfect when atoms occupy all lattice sites and no imperfection exists in the crystal. The broadening of diffraction peaks arises mainly due to three factors. The peaks become broader due to the effect of small crystallite sizes and thus an analysis of peaks broadening can be used to determine the crystallite sizes introduce additional broadening into the diffraction peaks.

The condition for constructive interference, reinforcement of *X*-ray scattering from a crystalline powder is given by Bragg's law which is given by **equation (4.1)**:

$$2d \sin\theta = n\lambda .$$

This equates the path difference of *X*-ray scattered from parallel crystalline planes spaced $d = d_{hkl}$ apart to an integral (n) number of *X*-ray wavelength: ' λ '. Here ' θ ' is the diffraction angle measured with respect to the crystalline planes. For an infinite crystal Bragg scattering occurs at discrete values of ' 2θ ' satisfying the Bragg condition, i.e.

Bragg peaks are δ -function. For finite sized crystals, the peaks are broadened over a range of angle.

To understand the phenomenon of fine particle broadening following argument of Cullity [2], we consider a finite crystal of thickness, $D_{thickness}=md$, where ‘ m ’ is an integer and ‘ d ’ is the distance between crystal planes, i.e. there are ‘ m ’ planes in ‘ $D_{thickness}$ ’.

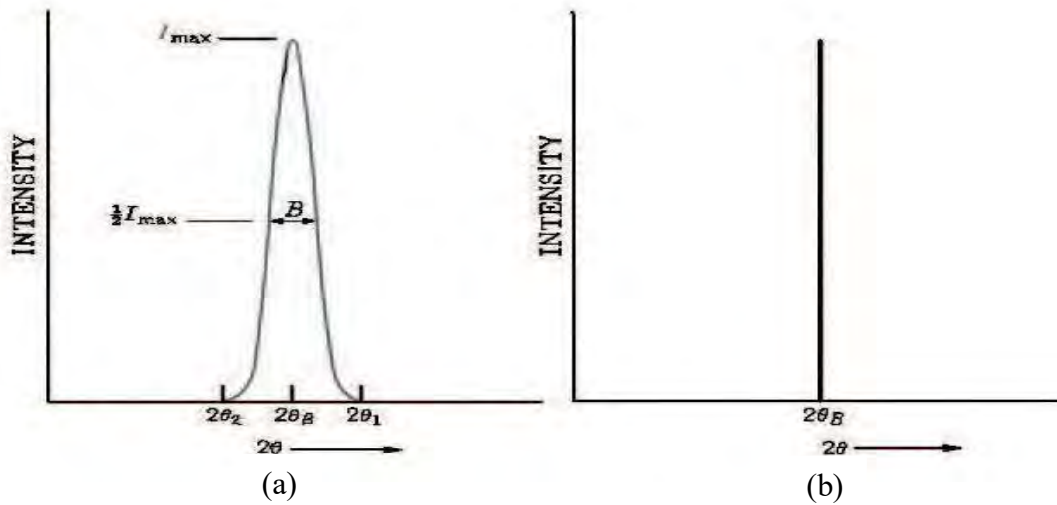


Fig. 4.2. The effect of fine particle size on diffraction curves (Schematic): (a) Small particle size and (b) Large particle size.

Considering Fig. 4.2, if the broadened Bragg peak begins at an angle $2\theta_2$ and ends at $2\theta_1$, the breadth of the peaks or full width at half maximum ($FWHM$) is given as,

$$\beta = \frac{1}{2}(2\theta_1 - 2\theta_2) = (\theta_1 - \theta_2) \quad \dots \quad \dots \quad \dots \quad \dots \quad \dots \quad \dots \quad \dots \quad \dots \quad \dots \quad (4.2)$$

Now if we consider the path differences for each of the two angles θ_1 and θ_2 for X-ray traveling the full thickness of the crystal. The width β is usually measured in radians. We now write path difference equations for these two angles, related to the entire thickness of the crystal rather to the distance between adjacent planes,

$$2D \sin \theta_1 = (m+1)\lambda \quad \dots \quad \dots \quad \dots \quad \dots \quad \dots \quad \dots \quad \dots \quad \dots \quad \dots \quad (4.3)$$

$$2D \sin \theta_2 = (m-1)\lambda \quad \dots \quad \dots \quad \dots \quad \dots \quad \dots \quad \dots \quad \dots \quad \dots \quad \dots \quad (4.4)$$

4.1.3 Lattice parameter, Lattice constant, and $r_{(variant)}$ measurements

To determine the lattice parameter of each peak of each sample the following formula is used,

$$a = d_{hkl} \sqrt{h^2 + k^2 + l^2} \dots \dots \dots \dots \dots \dots \dots \dots \dots \dots \dots \dots \quad (4.9)$$

Where 'h', 'k', and 'l' are the indices of the crystal planes.

Nelson-Riley method was used to determine the lattice constant of each ferrite sample. The Nelson-Riley function $F(\theta)$ is given as,

$$F(\theta) = \frac{1}{2} \left[(\cos^2 \theta / \sin \theta) + (\cos^2 \theta / \theta) \right] \dots \dots \dots \dots \dots \dots \dots \quad (4.10)$$

The values of the lattice parameter of all the peaks for a sample are plotted against $F(\theta)$. Then using a least square fit method (by the extrapolation of the lattice parameter lines) lattice constant (a_o) is determined. The point where the least square fit straight line cut the y-axis (i.e. at $F(\theta)=0$ or $\theta=90^\circ$) is the actual lattice constant (a_o) of the sample. This method was applied for all samples sintered at optimum temperature (T_s).

The mean ionic radius of the variant ions for $Li_{0.15}Ni_{0.30-x}Mn_xZn_{0.40}Fe_{2.15}O_4$ was calculated by the following relation [3],

$$r_{(variant)} = (0.30 - x)r_{Ni} + (x)r_{Mn} \dots \dots \dots \dots \dots \dots \dots \dots \dots \dots \quad (4.11)$$

Where ' r_{Ni} ' is the ionic radius of nickel, ' r_{Mn} ' is the ionic radius of manganese, and $x=0.00, 0.03, 0.06, 0.09, 0.12$, and 0.15 .

4.1.4 Density, porosity, and hopping length measurements

The physical or bulk densities (ρ_B) of the disc (pellet) shaped samples were determined by using the following expression,

$$\rho_B = \frac{M}{V} \text{ g / cm}^3 \dots \dots \dots \dots \dots \dots \dots \dots \dots \dots \dots \dots \quad (4.12)$$

Where ' M ' is the mass of the sample and ' V ' is the volume of the sample.

Here, $V = \pi r^2 t$. Where 'r' and 't' are the radius and thickness of the pellet shaped sample, respectively.

To determine the theoretical density (ρ_{th}) of the samples, we need to consider the following expression of molecular concentration, ' n_{mol} ' (number of molecule per unit volume),

$$n_{mol} = \frac{x}{a_o^3} \dots \dots \dots \dots \dots \dots \dots \dots \dots \dots \dots \dots \dots \quad (4.13)$$

But, the relation between molecular concentration (n_{mol}) and theoretical density (ρ_{th}) can be expressed as below,

$$n_{mol} = \frac{\rho_{th} N_A}{M_A} \dots \dots \dots \dots \dots \dots \dots \dots \dots \dots \dots \dots \dots \quad (4.14)$$

Where ' N_A ' is Avogadro's number ($6.0221 \times 10^{23} \text{ mol}^{-1}$) and ' M_A ' is the molecular weight.

Now, from **equation (4.13) & (4.14)** we can write that,

$$\begin{aligned} \frac{x}{a_o^3} &= \frac{\rho_{th} N_A}{M_A} \\ \Rightarrow \rho_{th} &= \frac{x M_A}{N_A a_o^3} \text{ g/cm}^3 \dots \dots \dots \dots \dots \dots \dots \dots \dots \dots \dots \dots \dots \quad (4.15) \end{aligned}$$

However, **equation (4.15)** is used to calculate the theoretical density (ρ_{th}) of the samples, where, $x=8$ for spinel cubic ferrites.

The porosity was calculated from the following relation,

$$P(\%) = \left\{ (\rho_{th} - \rho_B) / \rho_{th} \right\} \times 100 \dots \dots \dots \dots \dots \dots \dots \dots \dots \dots \quad (4.16)$$

Where ' ρ_{th} ' and ' ρ_B ' are the theoretical density and bulk density of the samples, respectively.

The distance between magnetic ions (hopping length) in the A-sites, shared sites, and B-sites have calculated from three relations, which are as the following [4],

$$L_{A-A} = \frac{a_o \sqrt{3}}{4} \dots \dots \dots \dots \dots \dots \dots \dots \dots \dots \dots \dots \dots \quad (4.17a)$$

$$L_{A-B} = \frac{a_o \sqrt{11}}{8} \dots \dots \dots \dots \dots \dots \dots \dots \dots \dots \dots \dots \quad (4.17b)$$

$$L_{B-B} = \frac{a_o \sqrt{2}}{4} \dots \dots \dots \dots \dots \dots \dots \dots \dots \dots \dots \dots \quad (4.17c)$$

Where ‘ a_o ’ is the lattice constant.

4.2 Surface morphology analysis

The samples of different compositions sintered at optimum temperature (T_s) were chosen for morphological analysis. The microstructural study was performed in order to have an insight of the grain structures. The surface micrographs were taken using field emission scanning electron microscopy (FESEM, Model no. JEOL JSM 7600F) to reveal the microstructure of the ferrites with respect to grain size, grain boundaries, and pores.

Average grain sizes (grain diameter) of the samples were determined from optical micrographs by linear intercept technique [5]. To do this, several random horizontal and vertical lines were drawn on the micrographs. Therefore, we counted the number of grains intersected and measured the length of the grains along the line traversed. Finally, the average grain size was calculated by the following equation,

$$D = \frac{L}{XN} \dots \dots \dots \dots \dots \dots \dots \dots \dots \dots \dots \dots \quad (4.18)$$

Where ‘ L ’ is the total length of the test line, ‘ X ’ symbolizes the magnification, and ‘ N ’ represents the total number of intercept.

The elemental analyses of the samples were investigated using Energy Dispersive X-ray Spectroscopy (EDS, Model no. JEOL JSM-7600F).

4.3 Complex initial permeability measurement

High permeability with low loss is the desirable property of ferrite for high-frequency application. One of the most important goals of ferrite research is to fulfill this requirement. The techniques of complex initial permeability measurement and frequency characteristics of the ferrite samples are described in sections 4.3.1 and 4.3.2.

4.3.1 Techniques for the initial permeability measurement

The measurements of the change in self-inductance of a coil in presence of the magnetic core confirm the measurements of permeability. The behavior of a self-inductance can be explained as follows. We assume an ideal lossless air coil of inductance (L_0). On insertion of a magnetic core with permeability (μ), the inductance will be ' μL_0 '. The complex impedance (Z) of this coil [6] can be expressed as follows,

$$Z = R + jX = j\omega L_0 \mu = j\omega L_0 (\mu' - j\mu'') \quad \dots \quad \dots \quad \dots \quad \dots \quad \dots \quad (4.19)$$

$$\text{Where resistive part is, } R = \omega L_0 \mu'' \quad \dots \quad \dots \quad \dots \quad \dots \quad \dots \quad \dots \quad \dots \quad (4.20a)$$

$$\text{And reactive part is, } X = \omega L_0 \mu' \quad \dots \quad \dots \quad \dots \quad \dots \quad \dots \quad \dots \quad \dots \quad (4.20b)$$

The RF permeability can be derived from the complex impedance of a coil (Z), given by **equation (4.19)**. The core is taken as toroid (ring) shape to avoid demagnetizing effects. The quantity L_0 is derived geometrically as presented in the next section (**section 4.3.2**).

4.3.2 Frequency characteristics of the ferrite samples

The frequency characteristics of the ferrite samples i.e. the initial permeability spectra were investigated using Wayne Kerr Precision Impedance Analyzer (Model no. 6520B). The complex permeability measurements on toroid shaped specimens were carried out at room temperature on all the samples in the frequency range 1 kHz-100 MHz. The real part (μ'_i) and imaginary part (μ''_i) of the complex permeability were calculated using the following relations [2],

$$\mu'_i = L_s / L_o \quad \dots \quad \dots \quad \dots \quad \dots \quad \dots \quad \dots \quad \dots \quad \dots \quad \dots \quad (4.21)$$

$$\mu''_i = \mu'_i \tan \delta_M \quad \dots \quad \dots \quad \dots \quad \dots \quad \dots \quad \dots \quad \dots \quad \dots \quad \dots \quad (4.22)$$

Where ' L_s ' is the self-inductance of the sample core and $L_o = \mu_o N^2 S / \pi \bar{d}$ is derived geometrically. Here ' L_o ' is the inductance of the winding coil without the sample core, ' N ' is the number of turns of the coil ($N=4$), ' S ' is the area of cross section of the toroid-shaped

sample, and $S = d \times h$, where, $d = d_2 - d_1/2$, ' d_1 ' and ' d_2 ' are inner and outer diameter, respectively, and ' h ' indicates the height of the sample. Again, \bar{d} is the mean diameter of the toroid-shaped sample: $\bar{d} = d_2 + d_1/2$. In equation (4.22) ' $\tan \delta_M$ ' is the magnetic loss factor. Moreover, the relative quality factor (RQF) is determined from the ratio,

$$RQF = \frac{\mu'_i}{\tan \delta_M} \quad \dots \quad \dots \quad \dots \quad \dots \quad \dots \quad \dots \quad \dots \quad \dots \quad \dots \quad (4.23)$$

4.4 Temperature-dependent μ'_i and Néel temperature measurements

The temperature dependent initial permeability (μ'_i) measurement is one of the most important measurements for ferrimagnetic materials. Néel temperature provides substantial information on the magnetic status of a substance in respect of the strength of exchange interaction. So, the determination of temperature-dependent initial permeability (μ'_i) and Néel temperature (T_N) are of great importance.

4.4.1 Techniques for measurement of temperature-dependent μ'_i

For the measurement of temperature-dependent μ'_i , the sample was kept inside a cylindrical oven with a thermocouple placed at the middle of the sample. The thermocouple measures the temperature inside the oven and also of the sample. The sample was kept just in the middle part of the cylindrical oven in order to minimize the temperature gradient. The temperature of the oven was then raised slowly.

If the heating rate is very fast then the temperature of the sample may not follow the temperature inside the oven, and there can be misleading information on the temperature of the sample. The thermocouple showing the temperature, in that case, will be erroneous.

Therefore, a slow heating rate was used to eliminate this problem. Also, slow heating ensures accuracy in the determination of Néel temperature. The oven was kept thermally insulated from the surroundings. The temperature dependent permeability μ'_i was measured at a constant frequency (1 MHz) of a sinusoidal wave.

4.6 Complex impedance spectroscopy measurement

The real part (Z') and imaginary part (Z'') of impedance for all the samples sintered at optimum T_s as a function of frequency at room temperature were also measured by Wayne Kerr Precision Impedance Analyzer (Model no. 6500B). The Cole-Cole plot at room temperature for all the samples sintered at optimum ' T_s ' was also measured from the real part (Z') and imaginary part (Z'') of impedance.

4.7 ac conductivity and ac resistivity measurements

The ac conductivity (σ_{ac}) and ac resistivity (ρ_{ac}) were determined at room temperature in the frequency range 20 Hz-120 MHz to study the mechanism of conduction. For the measurement of σ_{ac} and ρ_{ac} the samples were painted on either side with silver paste to ensure good electric contacts. The σ_{ac} and ρ_{ac} of the sample were calculated from the dielectric data using the relation [7],

$$\sigma_{ac} = \epsilon_0 \epsilon'' \omega \quad \dots \quad \dots \quad \dots \quad \dots \quad \dots \quad \dots \quad \dots \quad \dots \quad \dots \quad \dots \quad (4.26)$$

$$\rho_{ac} = \frac{1}{\epsilon_0 \epsilon'' \omega} \quad \dots \quad \dots \quad \dots \quad \dots \quad \dots \quad \dots \quad \dots \quad \dots \quad \dots \quad \dots \quad (4.27)$$

Where ' ϵ_0 ' is the permittivity of free space ($\epsilon_0 = 8.85 \times 10^{-12} \text{ Fm}^{-1}$), ' ϵ'' ' is the imaginary part of dielectric constant ($\epsilon'' = \epsilon' \tan \delta_E$), ' ϵ' ' is the real part of dielectric constant, ' $\tan \delta_E$ ' is the dielectric loss, and ' ω ' is the angular frequency.

References:

- [1] Kittel, C. (1996) *Introduction to Solid State Physics*, 7th edition, Jhon Wiley & Sons, Inc., New York.
- [2] Cullity, B. D. (1978) *Elements of X-ray diffraction*, 2nd edition, Addison-Wisley Publishing Company, Inc., California.
- [3] El-Ata, A. M. A. et al., "Spectral, initial magnetic permeability and transport studies of $\text{Li}_{0.5-0.5x}\text{Co}_x\text{Fe}_{2.5-0.5x}\text{O}_4$ spinel ferrite," *Journal of Magnetism and Magnetic Materials*, vol. 295(1), pp. 28-36, 2005.

- [4] El-Ghazzawy, E. H., and Amer, M. A., “Structural, elastic and magnetic studies of the as-synthesized $\text{Co}_{1-x}\text{Sr}_x\text{Fe}_2\text{O}_4$ nanoparticles,” *Journal of Alloys and Compounds*, vol. 690, pp. 293-303, 2017.
- [5] Hossain, A. K. M. A., *Investigation of colossal magnetoresistance in bulk and thick film magnetites*, Ph. D. Thesis, Imperial College, London, 1998.
- [6] Goldman, A. (1999) *Handbook of Modern Ferromagnetic Materials*, Kulwer Acad. Pub, Boston.
- [7] Mahajan, R .P., Patankar, K. K., Borange, N. M., Choudhari, S. C., Ghatage, A. K., and Patil, S. A., “Magnetoelectric effect in cobalt ferrite-barium titanate composite and their electrical properties,” *Indian J. Pure Appl. Phys.*, vol. 38, pp. 615-620, 2000.

.....

CHAPTER 5

RESULTS AND DISCUSSION

In this chapter, all results of the present work are presented in graphical and tabular forms. Possible explanations of these results of the ferrite samples are also included here. Recorded data from theoretical and experimental analyses are used to explain the features of ferrite nanoparticles and compared with earlier reported results. The structural analysis and surface morphology of the present samples are discussed here. Complex initial permeability, as well as temperature-dependent permeability including Néel temperature of the samples are also reported here. This chapter also presents the dielectric study of the ferrite samples including their ac conductivity and ac resistivity.

5.1 Structural analysis

The *XRD* is used to find the structural information of ferrite materials. It is important for phase identification of the ferrite samples. Lattice constant, theoretical density, bulk density, porosity, crystallite size, mean ionic radius of the variant ions, and the distance between magnetic ions (hopping length) reveal the structural characteristics of ferrite nanoparticles.

5.1.1 X-ray diffraction analysis

The *X-ray* diffraction (*XRD*) patterns for various $Li_{0.15}Ni_{0.30-x}Mn_xZn_{0.40}Fe_{2.15}O_4$ (where $x=0.00, 0.03, 0.06, 0.09, 0.12$, and 0.15) compositions sintered at 1523 K in air for 1 hour are shown in **Fig. 5.1**. The patterns clearly show the formation of spinel structure for each composition. It is observed that the *XRD* patterns of the samples consist of major spinel cubic phase. All the peaks in the spectrum for all samples matched well with characteristic reflections of spinel structure reported earlier. The *XRD* peaks are well indexed to the crystal planes of spinel ferrites (111), (220), (311), (222), (400), (422), (511), and (440).

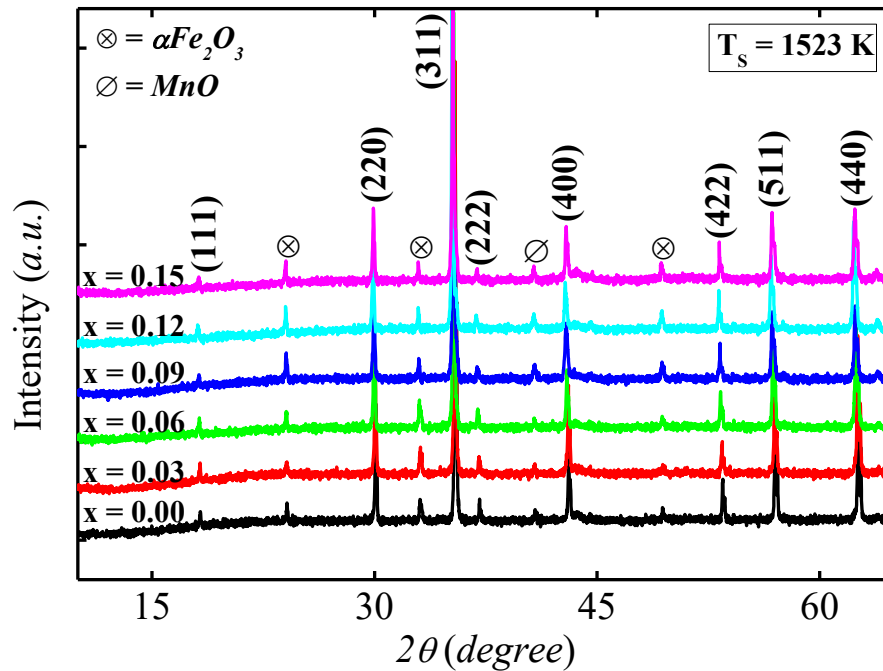


Fig. 5.1. The X-ray diffraction pattern of nanocrystalline $Li_{0.15}Ni_{0.30-x}Mn_xZn_{0.40}Fe_{2.15}O_4$ sintered at 1523 K.

In the spectrum, the minor impurity peaks, which are marked as ‘ \otimes ’ and ‘ \emptyset ’ are the secondary impurity Fe_2O_3 and MnO phases, respectively. These impurity peaks are mainly from the unreacted ingredients of the compositions. These impurity phases may be attributed due to the metastable, non-stoichiometry, Mn^{3+} and Mn^{4+} ions, low sintering temperature (T_s) as well as low decomposition temperature etc. [1-2]. These secondary impurity peaks may fully disappear at the higher sintering temperature [3-4].

5.1.2 Crystallite size

The crystallite size was estimated by using Debye-Scherrer formula from the broadening of the highest intensity peaks (311) of XRD patterns. Debye-Scherrer’s formula is: $D_{\text{crystallite}} = \frac{0.9\lambda}{\beta \cos\theta}$ [5], where ‘ $D_{\text{crystallite}}$ ’ is the crystallite size, ‘ λ ’ is the wavelength of the radiation used as the primary beam of $Cu K\alpha$ ($\lambda=0.154178$ nm), ‘ θ ’, is the angle of the incident beam in degree, and ‘ β ’ is the full width at half maximum (FWHM) of the fundamental reflection (311) in radian of the FCC ferrites phase. Debye-Scherrer’s formula

assumes approximation and gives the crystallite size if the grain size distribution is narrow and strain-induced effects are quite negligible.

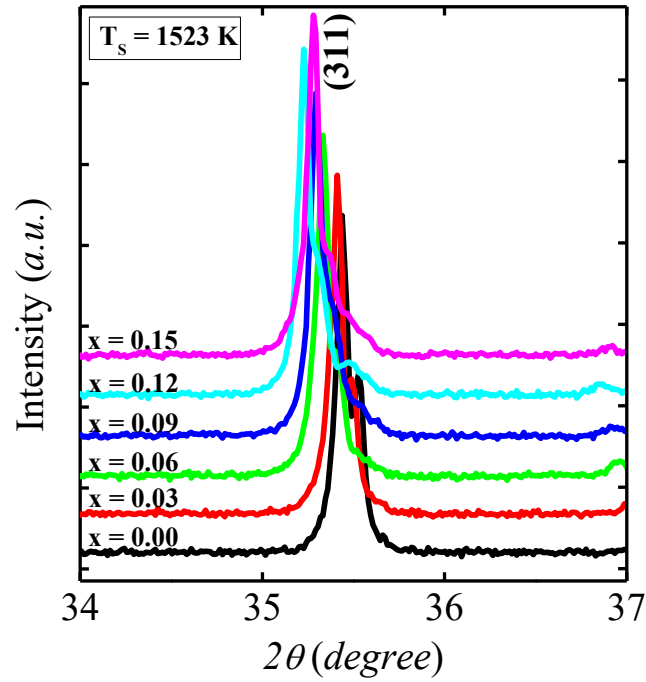


Fig. 5.2. The XRD patterns for various as prepared powder of $Li_{0.15}Ni_{0.30-x}Mn_xZn_{0.40}Fe_{2.15}O_4$ for (311) peak sintered at 1523 K.

Table 5.1. FWHM and crystallite size of various $Li_{0.15}Ni_{0.30-x}Mn_xZn_{0.40}Fe_{2.15}O_4$ samples sintered at 1523 K.

Mn Content, (x)	FWHM, β (in degree)	FWHM, β (in radian)	Crystallite size (nm)
0.00	0.1599	0.0028	52
0.03	0.1602	0.0028	52
0.06	0.1615	0.0028	52
0.09	0.1739	0.0030	48
0.12	0.1827	0.0032	46
0.15	0.1776	0.0031	47

Fig. 5.2 shows the XRD patterns for various as prepared powders of $Li_{0.15}Ni_{0.30-x}Mn_xZn_{0.40}Fe_{2.15}O_4$ sintered at 1523 K for 1 hour, where (311) peaks are shown in expanded form to understand the variation of β of the Bragg peaks with the Mn content.

From **Fig. 5.2**, it is observed that the value of β increases with increasing *Mn* content except $x=0.15$. This is because of the larger manganese ions replace nickel ions [6-9]. It is also seen that with increasing *Mn* content, the most intense peak (*311*) along with other peaks shifts towards lower 2θ angle up to $x=0.12$. This shifting of peaks with the substitution of Mn^{2+} in the place of Ni^{2+} is due to the relative difference between the ionic radii of Mn^{2+} (0.089 nm) with that of Ni^{2+} (0.077 nm) [10-11].

However, for $x=0.15$, β decreases and the peak (*311*) along with other peaks shows the right shift. This is may be due to the Mn^{2+} ions enter into both tetrahedral-*A* and octahedral-*B* sites instead of the preferable tetrahedral-*A* site [6-9]. The crystallite size ($D_{crystallite}$) of the sample is inversely proportional to β according to the Debye-Scherrer formula [5]. The observed crystallite size is in the range 46 to 52 nm and shown a decreasing trend with *Mn* content, which are listed in **Table 5.1**. Slightly broader (*311*) peak indicating that the nano-sized particle is formed [12].

5.1.3 Lattice constant and $r_{(variant)}$

The values of lattice constants have been calculated with the help of the Nelson-Riley function, shown in **equation (4.10)**. The values of lattice constants were estimated from the extrapolation of the lattice parameter lines (by linear fit) to $F(\theta)=0$ or $\theta=90^\circ$. The lattice constant (a_0) including $r_{(variant)}$ of various $Li_{0.15}Ni_{0.30-x}Mn_xZn_{0.40}Fe_{2.15}O_4$ compositions sintered at 1523 K for 1 hour are plotted as a function of *Mn* content shown in **Fig. 5.3**. The lattice constant slightly increases with the increase of *Mn* content up to $x=0.12$, obeying the Vegard's law [10]. The increase in lattice constant with decreasing *Ni* content can be explained on the basis of the ionic radii of variant cations. The ionic radii of the cations of Mn^{2+} and Ni^{2+} used in $Li_{0.15}Ni_{0.30-x}Mn_xZn_{0.40}Fe_{2.15}O_4$ are 0.089 and 0.077 nm, respectively [13]. In the present compositions, *Ni* is substituted by *Mn*. When the larger *Mn* ions enter the lattice, it reveals the expansion of the unit cell while preserving the overall cubic symmetry [14]. Therefore, a slight increase in lattice constant with increasing *Mn* content is expected. But for $x=0.15$, a slight decrease in lattice constant is observed. This is maybe for the right shift of the most intense XRD peak (*311*) along with other peaks and decrease of β for $x=0.15$. Here the assumption is, Mn^{2+} ions may be entered into both tetrahedral-*A* and octahedral-*B* sites instead of preferable tetrahedral-*A*

site [8]. The mean ionic radius of the variant ions for $Li_{0.15}Ni_{0.30-x}Mn_xZn_{0.40}Fe_{2.15}O_4$ can be written as: $r_{(variant)} = (0.30 - x)r_{Ni} + (x)r_{Mn}$. From this relation, because of higher ionic radii of Mn than that of Ni , it is observed that $r_{(variant)}$ is increased with increasing Mn content. The values of a_o and $r_{(variant)}$ are listed in **Table 5.2**.

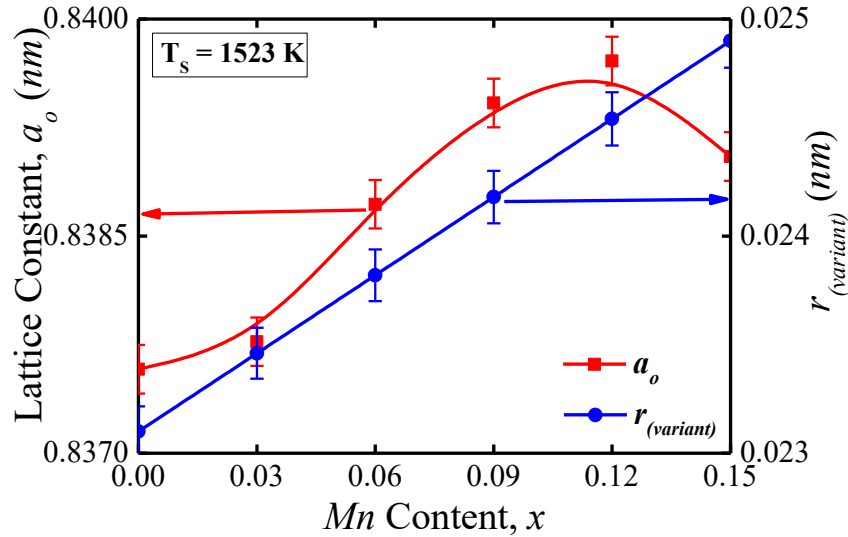


Fig. 5.3. Variation of the a_o and the $r_{(variant)}$ as a function of Mn content for $Li_{0.15}Ni_{0.30-x}Mn_xZn_{0.40}Fe_{2.15}O_4$ sintered at 1523 K.

5.1.4 Density and porosity

Density plays a key role in controlling the properties of ferrite materials. Both theoretical density (ρ_{th}) and bulk density (ρ_B) decrease in a similar fashion with the increase of Mn content in $Li_{0.15}Ni_{0.30-x}Mn_xZn_{0.40}Fe_{2.15}O_4$ for a fixed sintering temperature ($T_s=1523$ K), as shown in **Fig. 5.4**. It indicates that as Mn increases in $Li_{0.15}Ni_{0.30-x}Mn_xZn_{0.40}Fe_{2.15}O_4$, density decreases and porosity increases. This is happened for all Mn content except $x=0.15$. It is possible to explain this phenomenon in terms of the atomic weight of the constituent atoms. The atomic weight (**Appendix-B**) of Mn (54.9380 amu) is much less than the atomic weight of Ni (58.6934 amu) [15-16]. Therefore the density decrease is expected. On the other hand, porosity shows the opposite trend as shown in **Fig. 5.4**. The similar results from the same sintering temperature are also illustrated in **Fig. 5.5**, which indicates the variation of bulk density (ρ_B) and porosity (%P) with Mn content. However, for $x=0.15$, density slightly increased and porosity

slightly decreased. This is because of the lesser volume of the sample, which is attributed because of the smaller lattice constant (a_0) at $x=0.15$. The values of theoretical density (ρ_{th}) and bulk density (ρ_B) and porosity ($\%P$) of various samples sintered at 1523 K are presented in **Table 5.2**.

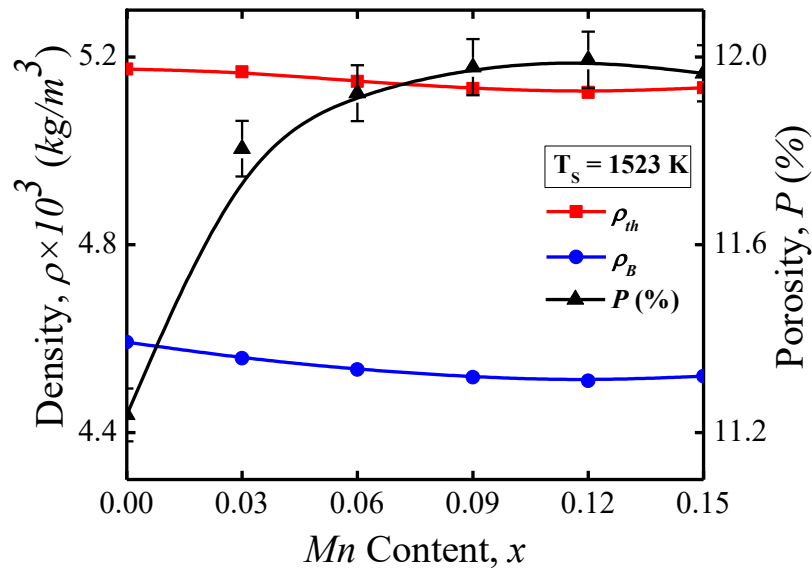


Fig. 5.4. The variation of ρ_{th} , ρ_B , and P (%) as a function of Mn content in $Li_{0.15}Ni_{0.30-x}Mn_xZn_{0.40}Fe_{2.15}O_4$ sintered at 1523 K .

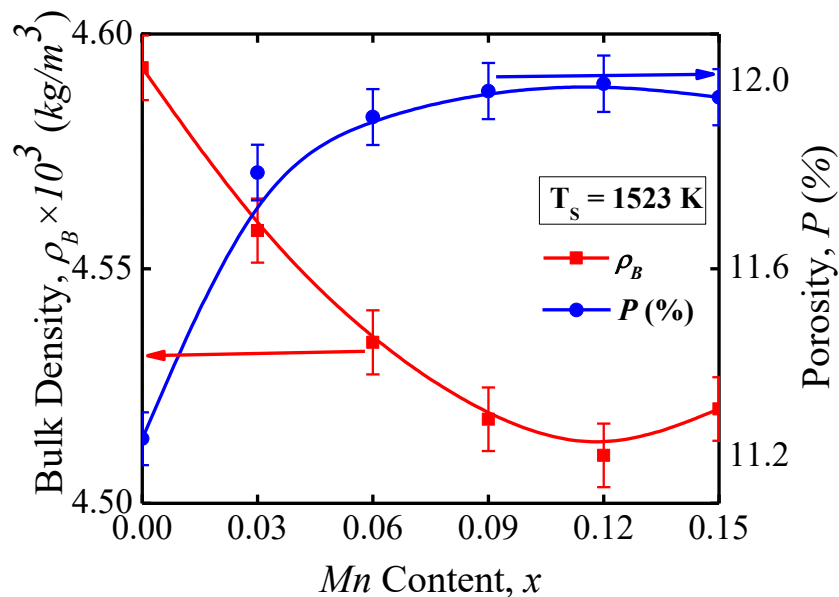


Fig. 5.5. The variation of bulk density and porosity (%) as a function of Mn content in $Li_{0.15}Ni_{0.30-x}Mn_xZn_{0.40}Fe_{2.15}O_4$ sintered at 1523 K .

The density of various $Li_{0.15}Ni_{0.30-x}Mn_xZn_{0.40}Fe_{2.15}O_4$ samples increases as the sintering temperature increases from 1373 to 1523 K, as shown in Fig. 5.6 and as expected porosity decreases with sintering temperature. During the sintering process, the thermal energy generates a force that drives the grain boundaries to grow over pores, thereby decreasing the pore volume and increasing the density of the material. It is known that the porosity of ceramics results from two sources, such as intra-granular porosity and inter-granular porosity. Thus the total porosity could be written as $P = P_{intra} + P_{inter}$. The inter-granular porosity mainly depends on the grain size. At higher T_s grain forms uniformly and void reduces as a result density increases [12,17].

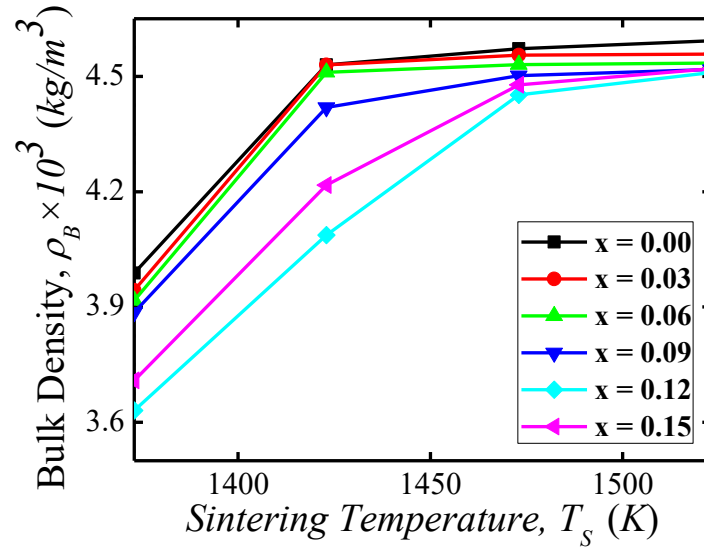


Fig. 5.6. The variation of bulk density as a function of T_s for various $Li_{0.15}Ni_{0.30-x}Mn_xZn_{0.40}Fe_{2.15}O_4$ samples.

However, the distance between the centers of adjacent ions is known as the hopping length (L). The distance between magnetic ions (hopping length) in the A -sites, shared sites, and B -sites can be calculated using the following relations [11,18]: $L_{A-A} = \frac{a_o \sqrt{3}}{4}$, $L_{A-B} = \frac{a_o \sqrt{11}}{8}$, and $L_{B-B} = \frac{a_o \sqrt{2}}{4}$. It is found that the hopping lengths increase with the increase of Mn content up to $x=0.12$, which suggests that the magnetic ions become larger with Mn^{2+} dopant. But for maximum Mn content of this current research ($x=0.15$), hopping

lengths decrease. This is for the decrease of lattice constant (a_o) for that specific Mn content. Various values of hopping lengths are also tabulated in **Table 5.2**.

Table 5.2. The lattice constant, the mean ionic radius of the variant ions, theoretical density, bulk density, porosity, the distance between magnetic ions in the A -sites, shared sites, and B -sites, and average grain size of various $Li_{0.15}Ni_{0.30-x}Mn_xZn_{0.40}Fe_{2.15}O_4$ samples sintered at 1523 K .

Mn Content, (x)	Lattice Constant a_o (nm)	$r_{(variant)}$ (nm)	$\rho_{th} \times 10^3$ (kg/m ³)	$\rho_B \times 10^3$ (kg/m ³)	Porosity P (%)	L_{A-A} (nm)	L_{A-B} (nm)	L_{B-B} (nm)	Grain Size (μm)
0.00	0.8376	0.0231	5.1743	4.5928	11.2375	0.3627	0.3472	0.2961	0.76
0.03	0.8378	0.0235	5.1682	4.5581	11.8048	0.3628	0.3473	0.2962	0.85
0.06	0.8387	0.0238	5.1481	4.5343	11.9231	0.3632	0.3477	0.2965	0.98
0.09	0.8394	0.0242	5.1327	4.5179	11.9784	0.3635	0.3480	0.2968	1.01
0.12	0.8397	0.0245	5.1249	4.5102	11.9939	0.3636	0.3481	0.2969	1.08
0.15	0.8391	0.0249	5.1344	4.5201	11.9651	0.3633	0.3479	0.2967	1.04

5.2 Surface morphology

The microstructure of ferrites strongly influences their electrical and magnetic properties, so it is necessary to determine the average grain size (D_{grain}) and the type of grain growth of the samples from the micrographs. The *FESEM* micrographs and the *EDS* patterns of various $Li_{0.15}Ni_{0.30-x}Mn_xZn_{0.40}Fe_{2.15}O_4$ sintered at 1523 K have been analyzed. The *FESEM* micrographs from 3 (three) different magnifications (5000, 10000, and 15000) are given in **Fig. 5.7-Fig. 5.9**. The D_{grain} of the samples are calculated from these optical micrographs by linear intercept technique with the help of the equation:

$$D_{grain} = \frac{L}{XN},$$

where 'L' is the total length of the test line, 'X' symbolizes the magnification, and 'N' represents the total number of intercept, and are presented in

Table 5.2. It is observed that average grain size (grain diameter) noticeably dependent on Mn substitution. We observed that the D_{grain} increases with increasing Mn^{2+} substitution up to $x=0.12$, which could be attributed to Mn^{2+} have higher ionic radius than Ni^{2+} [11]. This is also may occur due to the modified chemical properties as a result of Mn substitution. Depending on Mn substitution, brand new chemical compositions are produced. The physical and chemical properties of each substituted composition are

completely different. This also implies that the melting point of *Mn* (1518 K) is lesser than that of *Ni* (1726 K) [2,14].

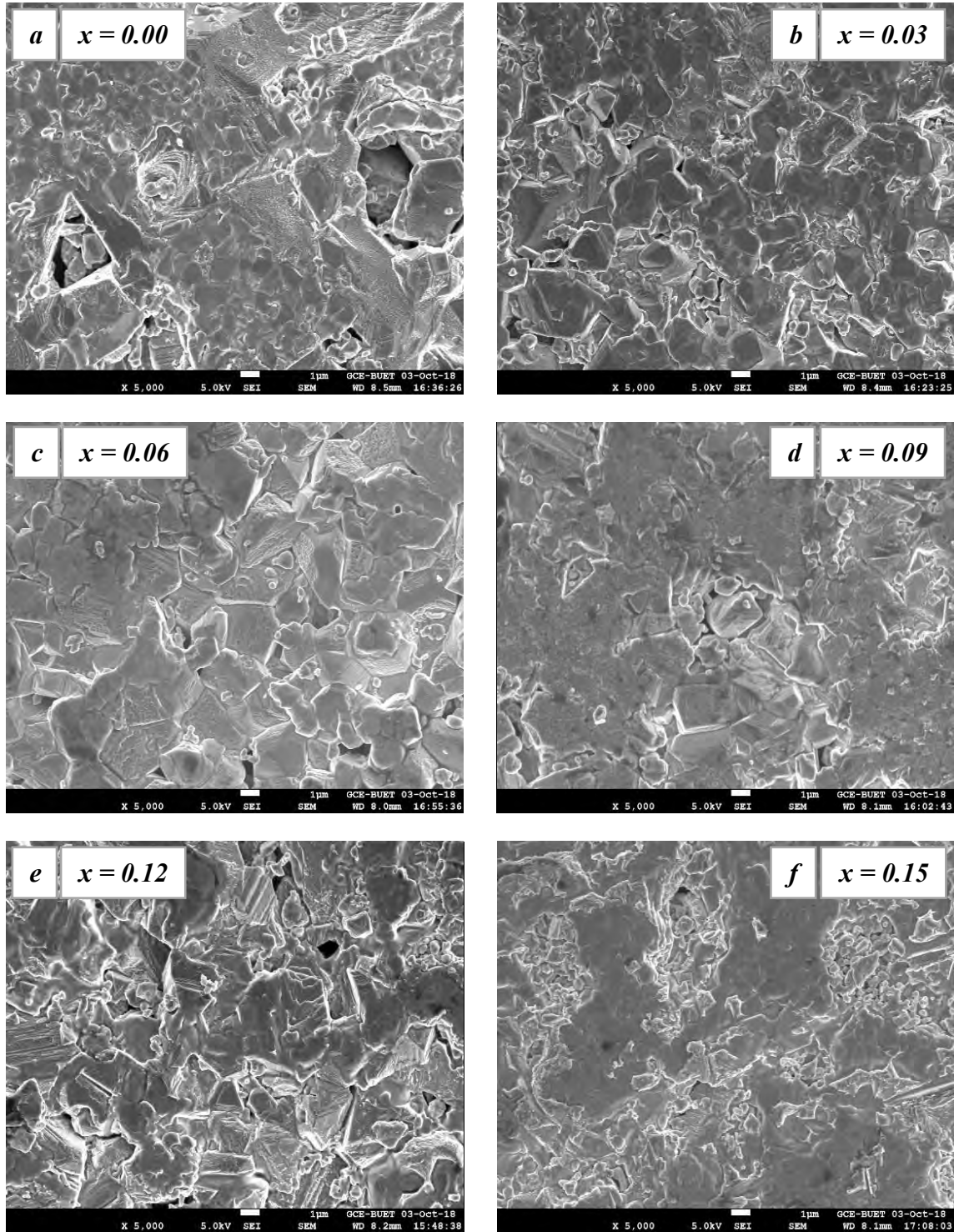


Fig. 5.7. (a-f) The FESEM micrographs of manganese substituted spinel ferrite nanoparticles of various $Li_{0.15}Ni_{0.30-x}Mn_xZn_{0.40}Fe_{2.15}O_4$ sintered at 1523 K, where the magnification is 5000.

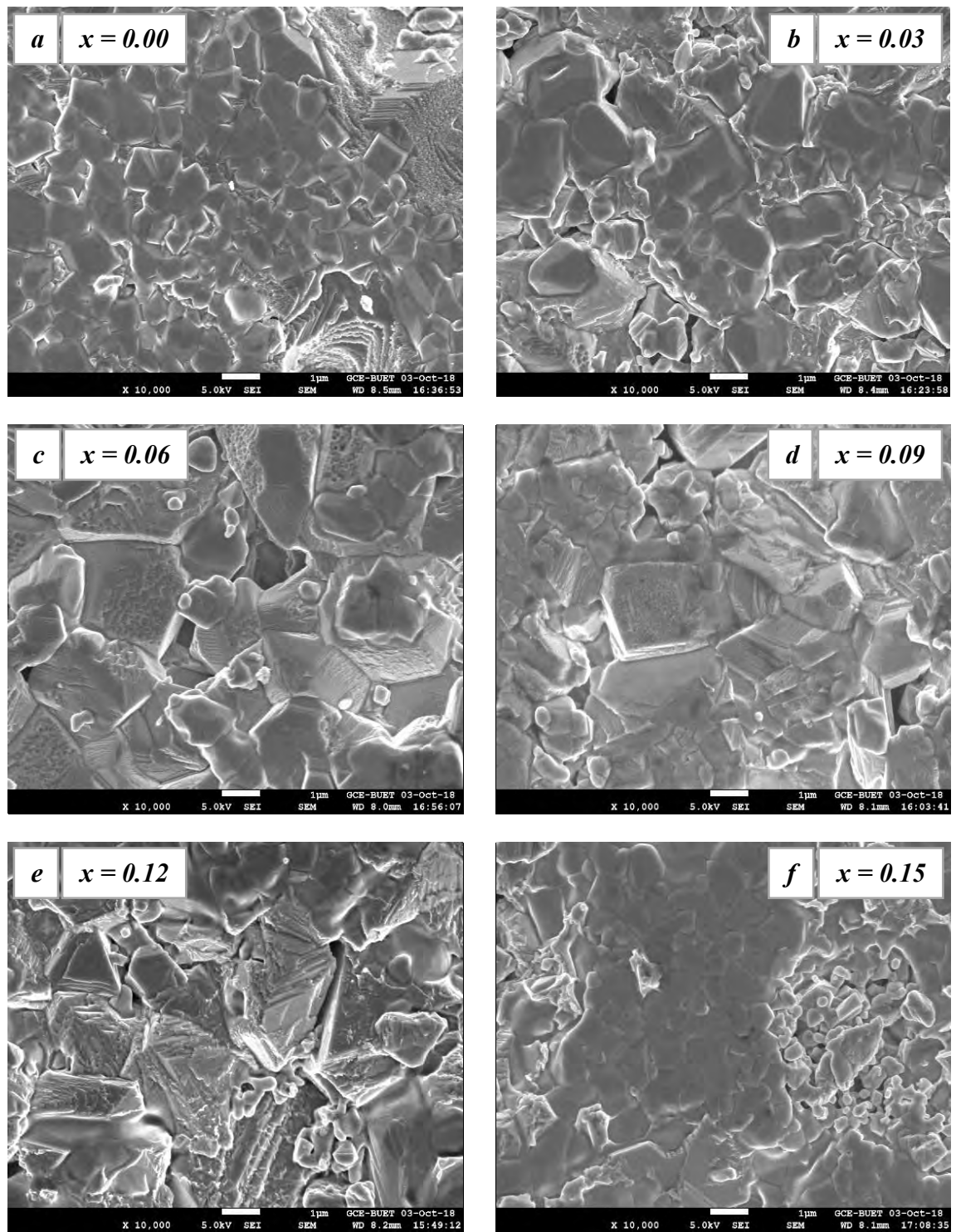


Fig. 5.8. (a-f) The FESEM micrographs of manganese substituted spinel ferrite nanoparticles of various $\text{Li}_{0.15}\text{Ni}_{0.30-x}\text{Mn}_x\text{Zn}_{0.40}\text{Fe}_{2.15}\text{O}_4$ sintered at 1523 K, where the magnification is 10000.

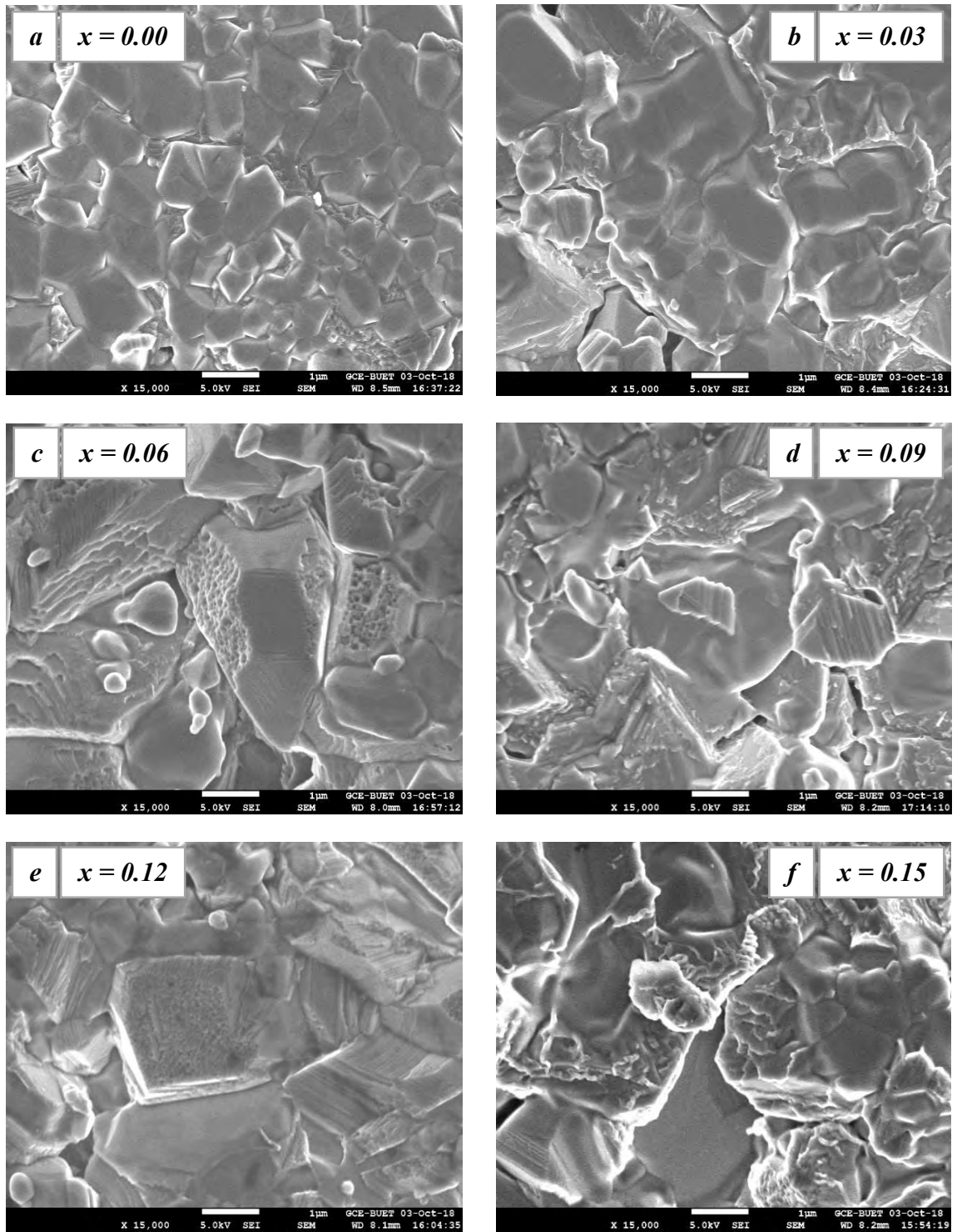


Fig. 5.9. (a-f) The FESEM micrographs of manganese substituted spinel ferrite nanoparticles of various $Li_{0.15}Ni_{0.30-x}Mn_xZn_{0.40}Fe_{2.15}O_4$ sintered at 1523 K, where the magnification is 15000.

For $x=0.15$, the D_{grain} decreases because in this case significant amount of Mn^{2+} resides at the grain boundaries which hamper the grain growth and may be increased in

strain on the grains, consequently, lead the D_{grain} to decrease. In this case, it is also noticeable that, for $x=0.15$, the lattice constant, density, porosity, and hopping lengths also show the opposite trend.

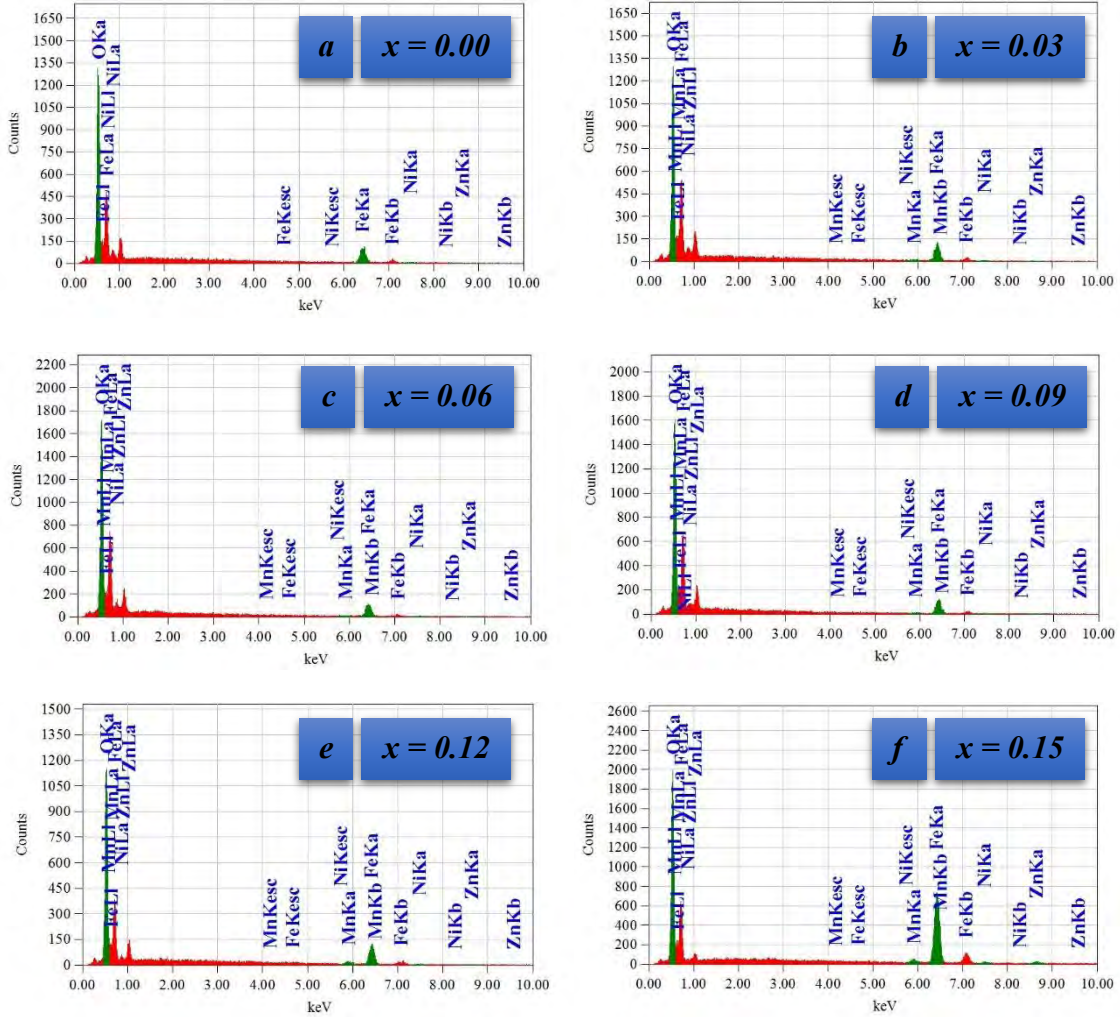


Fig. 5.10. (a-f) The EDS spectrum of manganese substituted spinel ferrite nanoparticles of various $Li_{0.15}Ni_{0.30-x}Mn_xZn_{0.40}Fe_{2.15}O_4$ sintered at 1523 K.

The surface elemental composition of the samples of $Li_{0.15}Ni_{0.30-x}Mn_xZn_{0.40}Fe_{2.15}O_4$ sintered at 1523 K was investigated by the energy dispersive X-ray spectroscopy (EDS) analysis. The EDS spectra of the different samples are shown in Fig. 5.10, which confirmed the presence of Ni, Mn, Zn, Fe, and O elements. But Li is absent in the EDS spectrum because of its lower atomic number and comparatively light-weight. The EDS spectrum was measured at different regions of the samples and it was found that a relatively

higher amount of *Mn* resides at the grain boundaries for $x=0.15$. The quantitative analysis of the *EDS* spectrums results that the relative atomic ratio of manganese substituted in mixed ferrites is near to the expected values. It is suggested that the experimental values of the atomic percentage of different spinel ferrites have some oxygen deficiency with the stoichiometry in preparation [4].

5.3 Complex initial permeability

The variation of complex initial permeability (μ_i' and μ_i'') as a function of frequency for *Mn* substituted various $Li_{0.15}Ni_{0.30-x}Mn_xZn_{0.40}Fe_{2.15}O_4$ in the frequency range of 0.1 MHz-100 MHz sintered at 1523 K are shown in **Fig. 5.11**. It is observed that the real part of initial permeability (μ_i') decreases for $x=0.03$, then it increases for $x=0.06$, after that it decreases again for $x=0.09$. For $x=0.12$, μ_i' increases again and attains the maximum value ($\mu_i'=334$), which is 7% greater compared to the parent composition. For $x=0.15$, μ_i' decreases again. It is also observed that the imaginary part of initial permeability (μ_i'') decreases with frequency and reached a minimum value at a certain frequency, where the μ_i' starts to decrease. The μ_i'' appears because of lagging of the domain walls motion with the applied alternating magnetic field. The decrease in μ_i' implies the onset of ferromagnetic resonance. The μ_i' of ferrites is influenced by their intrinsic factors like preferential site occupancy as well as extrinsic properties such as density, porosity, and grain size [19-20]. Processing parameters also play a crucial role to tune its characteristics. As μ_i' is very sensitive to several parameters so it is still challenging to obtain a precise conclusion for variation of μ_i' with concentration.

The real part of initial permeability (μ_i') at 1 MHz, maximum relative quality factor (RQF_{max}), and resonance frequency (f_r) for various $Li_{0.15}Ni_{0.30-x}Mn_xZn_{0.40}Fe_{2.15}O_4$ spinel ferrite nanoparticles sintered at 1523 K are presented in **Table 5.3**. For polycrystalline ferrites, the permeability is the superposition of two different magnetizing processes [21-23]: (i) Spin rotation and (ii) Domain wall motion, which can be delineated as: $\mu_i = 1 + \chi_{spin} + \chi_w$, where ' χ_{spin} ' is intrinsic rotational susceptibility and ' χ_w ' is domain wall susceptibility. The χ_{spin} and χ_w can be written as: $\chi_{spin} = \frac{2\pi M_s^2}{K}$ and

$\chi_w = \frac{3\pi M_s^2 D_{grain}}{4\gamma}$, where ' M_s ' is that the saturation magnetization, ' K ' the anisotropy constant, ' D_{grain} ' the average grain diameter, and ' γ ' the domain wall energy. Accordingly, the domain wall motion is influenced by the average grain size and enhanced with the increase of grain size. Generally, μ_i' of ferrite material obeys the relation: $\mu_i' \propto \frac{M_s^2 D_{grain}}{\sqrt{K_1}}$, where ' K_1 ' is the magneto-crystalline anisotropy constant [24].

When the grain growth is normal then the μ_i' would be proportional to D_{grain} . Increase in grain size results in an increase in the domain walls number in every grain. As the domain walls movement regulates the μ_i' so any intensification in the domain walls number would consequence in an increase in μ_i' [25-26].

Table 5.3. The real part of initial permeability (μ_i') at 1 MHz, maximum relative quality factor (RQF_{max}), and resonance frequency (f_r) for various $Li_{0.15}Ni_{0.30-x}Mn_xZn_{0.40}Fe_{2.15}O_4$ spinel ferrite nanoparticles sintered at 1523 K including expected total (net) magnetization (M_T) for various samples.

Sample Composition	μ_i' (1 MHz)	RQF_{max}	f_r (MHz)	T_N (K)	M_T (μ_B)
$Li_{0.15}Ni_{0.30}Zn_{0.40}Fe_{2.15}O_4$	295	12101	1.44	593	5.35
$Li_{0.15}Ni_{0.27}Mn_{0.03}Zn_{0.40}Fe_{2.15}O_4$	292	9663	4.32	588	5.44
$Li_{0.15}Ni_{0.24}Mn_{0.06}Zn_{0.40}Fe_{2.15}O_4$	308	13369	5.68	583	5.53
$Li_{0.15}Ni_{0.21}Mn_{0.09}Zn_{0.40}Fe_{2.15}O_4$	256	9278	4.67	573	5.62
$Li_{0.15}Ni_{0.18}Mn_{0.12}Zn_{0.40}Fe_{2.15}O_4$	309	14087	6.38	563	5.71
$Li_{0.15}Ni_{0.15}Mn_{0.15}Zn_{0.40}Fe_{2.15}O_4$	283	9246	4.32	578	5.80

Accordingly, the increase in μ_i' with Mn substitution can be attributed to the increase in D_{grain} . However, decreasing in the μ_i' of $Li_{0.15}Ni_{0.30-x}Mn_xZn_{0.40}Fe_{2.15}O_4$ can be attributed to the ionic radii of Mn^{2+} may be greater than the lattice of spinel, so considerable Mn^{2+} find difficulty to enter the spinel lattice, for this reason, a significant amount of Mn^{2+} reside at grain boundaries which hamper the mobility of grain boundary as well as grain growth. Consequently, the domain rotation and domain wall motion become difficult which causes a decrease in μ_i' . Density is inversely proportional to porosity. When density increases then porosity decreases thus connectivity among grains increases with increasing density. High connectivity among grains facilitates magnetic flux

flow which increases μ_i' . It is found that μ_i' remains almost constant up to resonance frequency (f_r) and the relation between μ_i' and f_r are related inversely, which can be explained by Snoek's law: $\mu_i' f_r = \text{constant}$. The μ_i' shows a decreasing trend with increasing frequency because nonmagnetic impurities between grains and intra-granular pores function as pinning points at higher frequencies and hamper the motion of spin and domain walls increasingly [25-26].

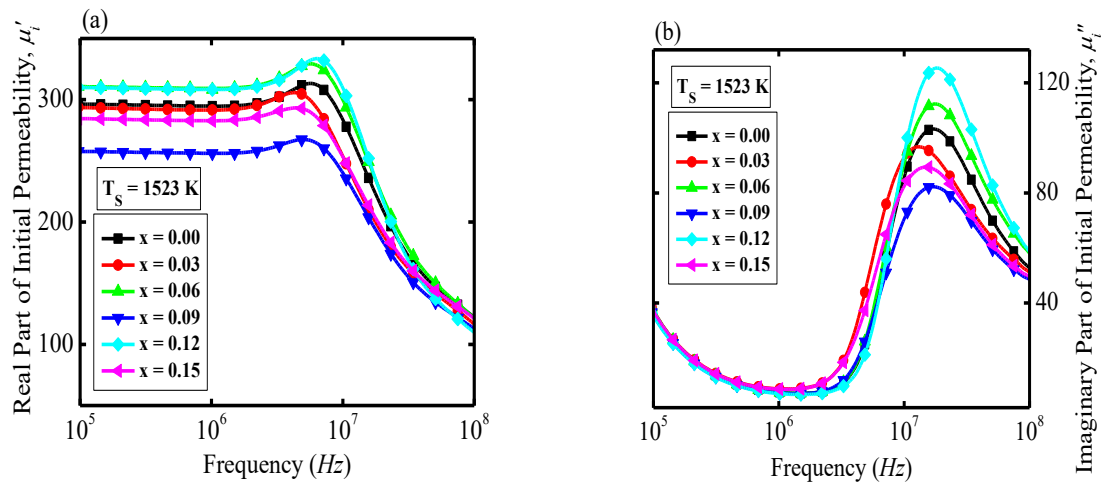


Fig. 5.11. The variation of (a) μ_i' and (b) μ_i'' as a function of frequency for various $\text{Li}_{0.15}\text{Ni}_{0.30-x}\text{Mn}_x\text{Zn}_{0.40}\text{Fe}_{2.15}\text{O}_4$ spinel ferrite nanoparticles sintered at 1523 K.

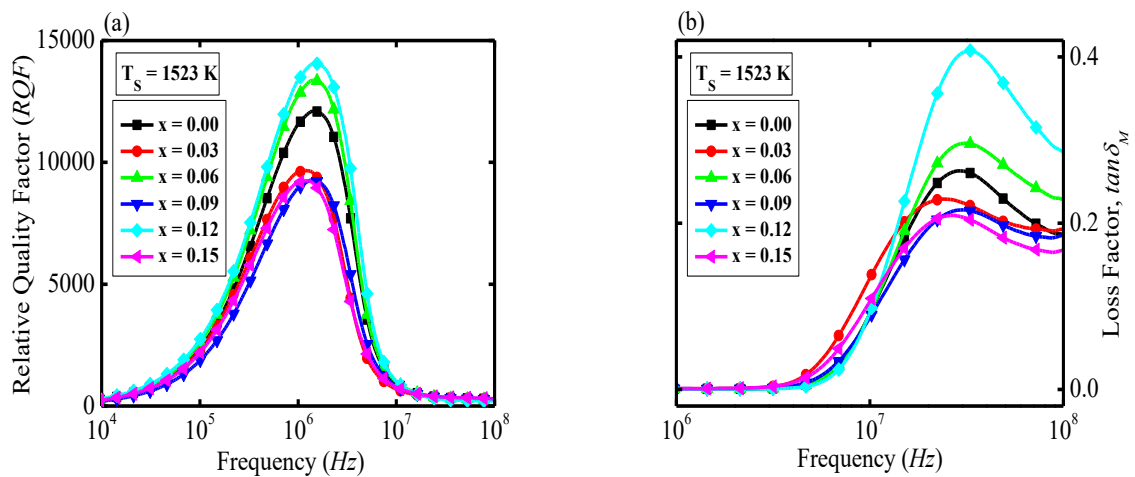


Fig. 5.12. The variation of (a) RQF and (b) $\tan\delta_M$ as a function of frequency for various $\text{Li}_{0.15}\text{Ni}_{0.30-x}\text{Mn}_x\text{Zn}_{0.40}\text{Fe}_{2.15}\text{O}_4$ spinel ferrite nanoparticles sintered at 1523 K.

The variation of RQF and $\tan\delta_M$ as a function of frequency for various $Li_{0.15}Ni_{0.30-x}Mn_xZn_{0.40}Fe_{2.15}O_4$ spinel ferrite nanoparticles sintered at 1523 K are shown in **Fig. 5.12**. The maximum value of RQF at 1523 K is 14067 (for $x=0.12$), which is 16% higher than that of parent composition. RQF is often used as a yardstick to measure the performance in practical applications. It is observed that RQF increases with increasing frequency and then it shows a peak at particular frequencies. After showing a peak RQF starts to decrease with more increase in frequency. RQF becomes higher may be due to the growth of lesser imperfections and defects. The magnetic loss factor $\tan\delta_M$ arises from the lag of domain wall motion with respect to applied alternating magnetic field. It is attributed to several domain effects like non-uniform and non-repetitive domain wall motion, nucleation and annihilation of the domain wall, domain wall bowing, and the localized variation of flux density [27].

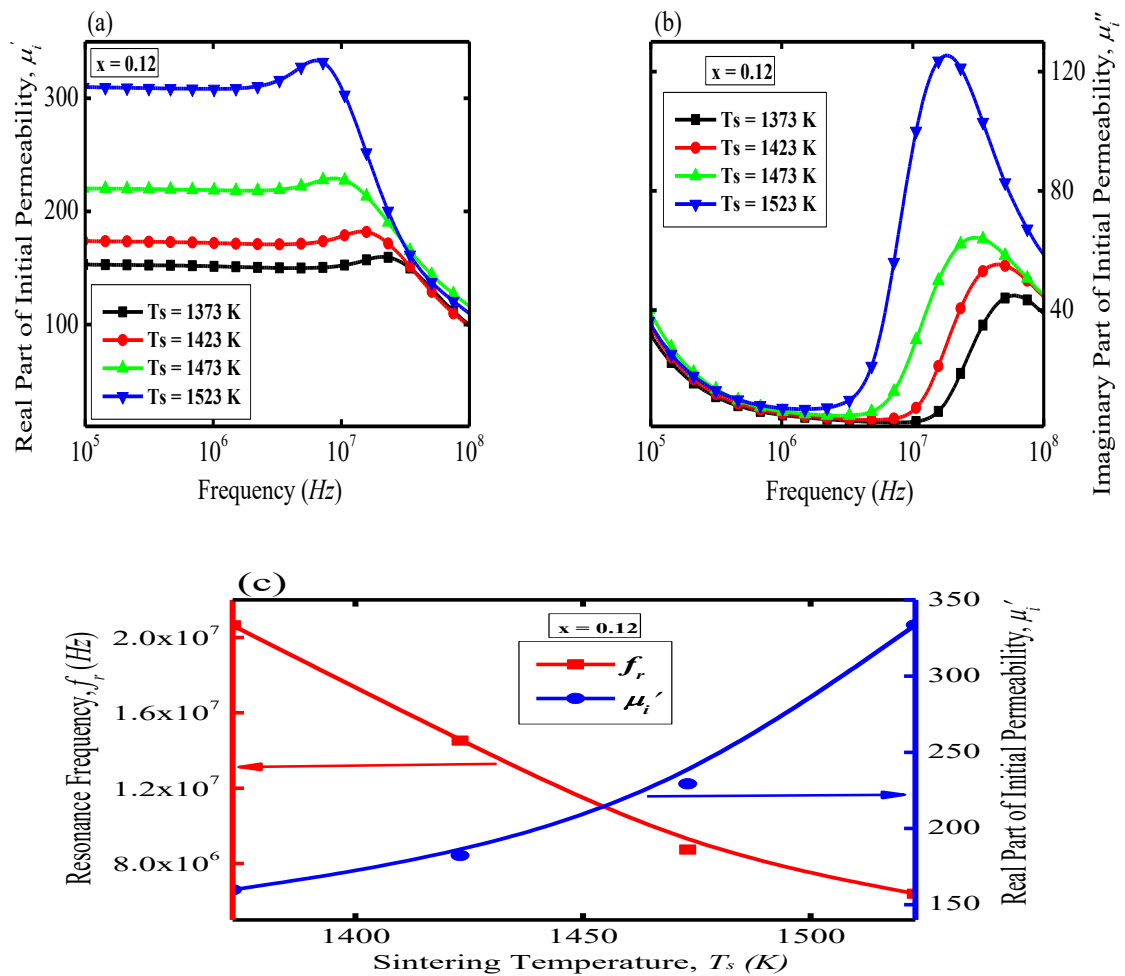


Fig. 5.13. The variation of (a) μ_i' , (b) μ_i'' as a function of frequency, and (c) variation of μ_i' & f_r with T_s for $Li_{0.15}Ni_{0.30-x}Mn_xZn_{0.40}Fe_{2.15}O_4$ ($x=0.12$) spinel ferrite nanoparticles sintered at various temperatures.

However, **Fig. 5.13(a-b)** illustrates the variation of μ_i' and μ_i'' as a function of frequency for $Li_{0.15}Ni_{0.18}Mn_{0.12}Zn_{0.40}Fe_{2.15}O_4$ spinel ferrite nanoparticles sintered at 1373, 1423, 1473, and 1523 K. It is noticed that the μ_i' increases with increasing sintering temperature from 1373 to 1523 K. Almost similar behavior is observed for all other $Li_{0.15}Ni_{0.30-x}Mn_xZn_{0.40}Fe_{2.15}O_4$ samples sintered at 1373, 1423, 1473, and 1523 K (not shown in figure). It is also observed that the μ_i'' as a function of frequency for $Li_{0.15}Ni_{0.18}Mn_{0.12}Zn_{0.40}Fe_{2.15}O_4$ sintered at 1373, 1423, 1473, and 1523 K shows significant results, which is because of lagging of domain wall motion. In **Fig. 5.13(a)** it is also found that the domain wall relaxation frequency is known as resonance frequency (f_r), for all compositions, shifted from a higher value to a lower value as T_s increases. From this observation, it can be declared that the μ_i' is inversely proportional to f_r for $Li_{0.15}Ni_{0.18}Mn_{0.12}Zn_{0.40}Fe_{2.15}O_4$ with various T_s . Accordingly, **Fig. 5.13(c)** shows the variation of μ_i' and f_r with T_s for $Li_{0.15}Ni_{0.18}Mn_{0.12}Zn_{0.40}Fe_{2.15}O_4$, which confirms the Snoek's limit [21-28].

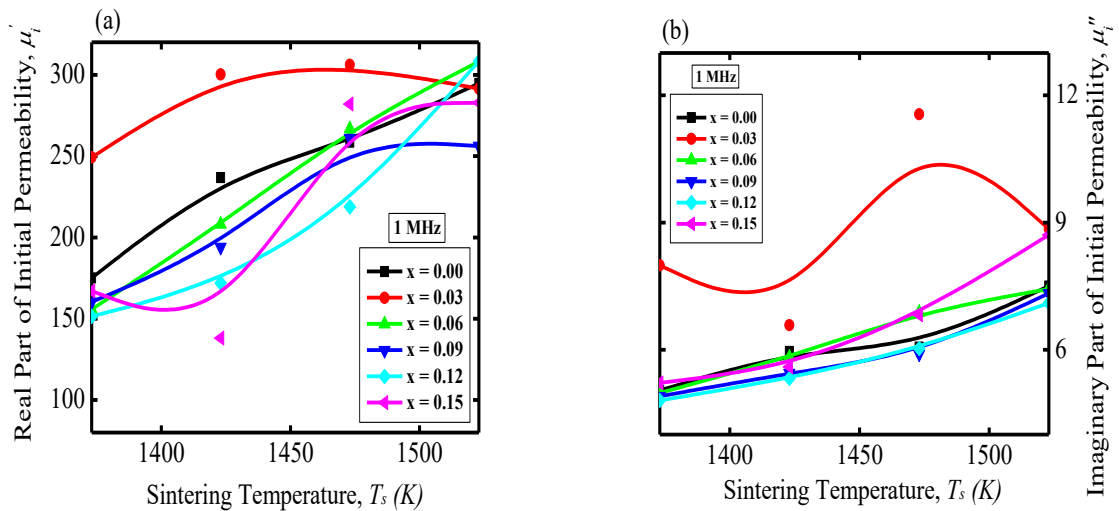


Fig. 5.14. The variation of (a) μ_i' and (b) μ_i'' as a function of sintering temperature for various $Li_{0.15}Ni_{0.30-x}Mn_xZn_{0.40}Fe_{2.15}O_4$ spinel ferrite nanoparticles at a constant frequency of 1 MHz.

Moreover, at a constant frequency (1 MHz), the graphs of μ_i' and μ_i'' as a function of sintering temperature for various $Li_{0.15}Ni_{0.30-x}Mn_xZn_{0.40}Fe_{2.15}O_4$ spinel ferrite nanoparticles are shown in **Fig. 5.14**. It is noticed that at a constant frequency (1 MHz), for $x=0.03$, 0.09, and 0.15, the real part of initial permeability, μ_i' reaches its largest value at 1473 K, and for $x=0.00$, 0.06, and 0.12, μ_i' reaches its largest value at 1523 K. It is also

found that at the sintering temperature of 1373 K, 1423 K, and 1473 K, $x=0.03$ samples show the maximum value of μ_i' . But at the sintering temperature of 1523 K (which is considered as optimum temperature), $x=0.12$ sample shows the maximum value of μ_i' (which is the highest value of μ_i'). In this case, the curves of μ_i'' from the damping of domain wall motion as a function of T_s also reveal similar significant effects as μ_i' .

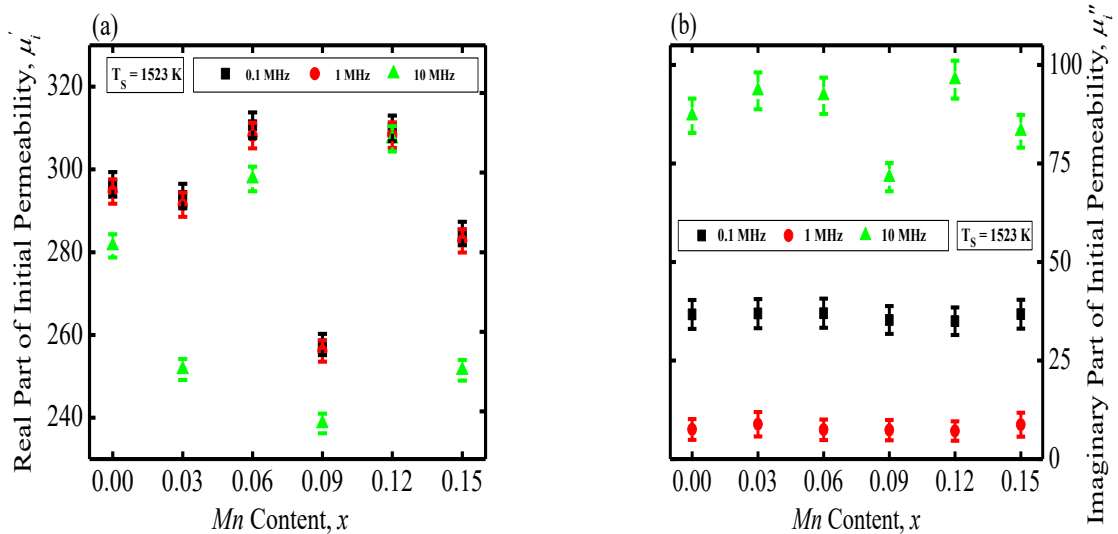


Fig. 5.15. The variation of (a) μ_i' and (b) μ_i'' as a function of Mn content (x) for various $Li_{0.15}Ni_{0.30-x}Mn_xZn_{0.40}Fe_{2.15}O_4$ spinel ferrite nanoparticles sintered at 1523 K, at different frequencies.

However, the **Fig. 5.15** presents the curves of μ_i' and μ_i'' as a function of Mn content (x) for various $Li_{0.15}Ni_{0.30-x}Mn_xZn_{0.40}Fe_{2.15}O_4$ spinel ferrite nanoparticles sintered at 1523 K, at the frequencies of 0.1 MHz, 1 MHz, and 10 MHz. The curves of the variation of μ_i' with Mn content for 0.1 MHz, and 1 MHz are almost similar and significantly differ from the curve for 10 MHz from a point of view of the practical applications of ferrite nanomaterial.

The change in μ_i' with the change of Mn substitution can be credited to the change in D_{grain} . The relationship between permeability and average grain size would generally be proportion only if the grain growth is normal.

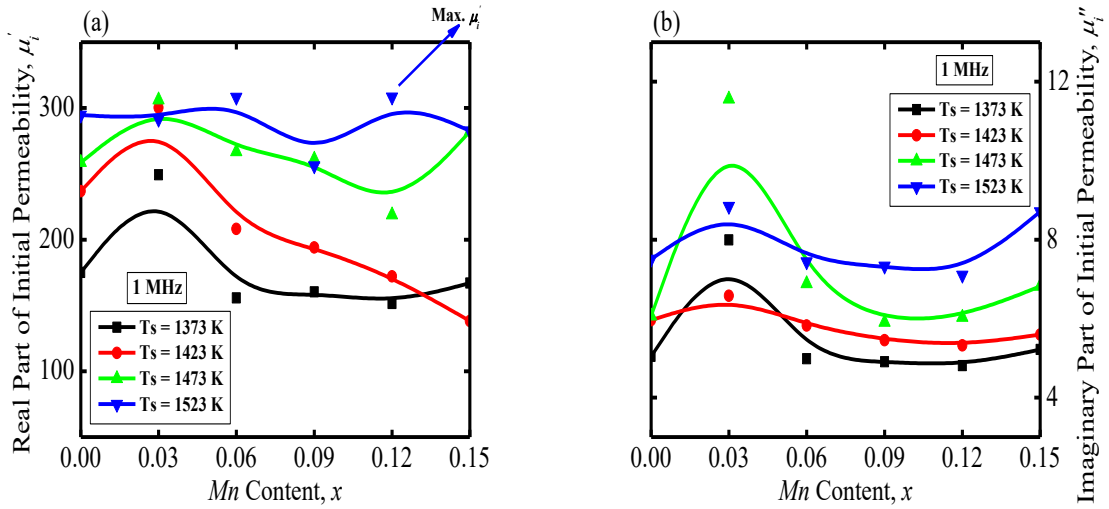


Fig. 5.16. The variation of (a) μ_i' and (b) μ_i'' as a function of Mn content (x) for various $Li_{0.15}Ni_{0.30-x}Mn_xZn_{0.40}Fe_{2.15}O_4$ spinel ferrite nanoparticles at a constant frequency of 1 MHz sintered at various temperatures.

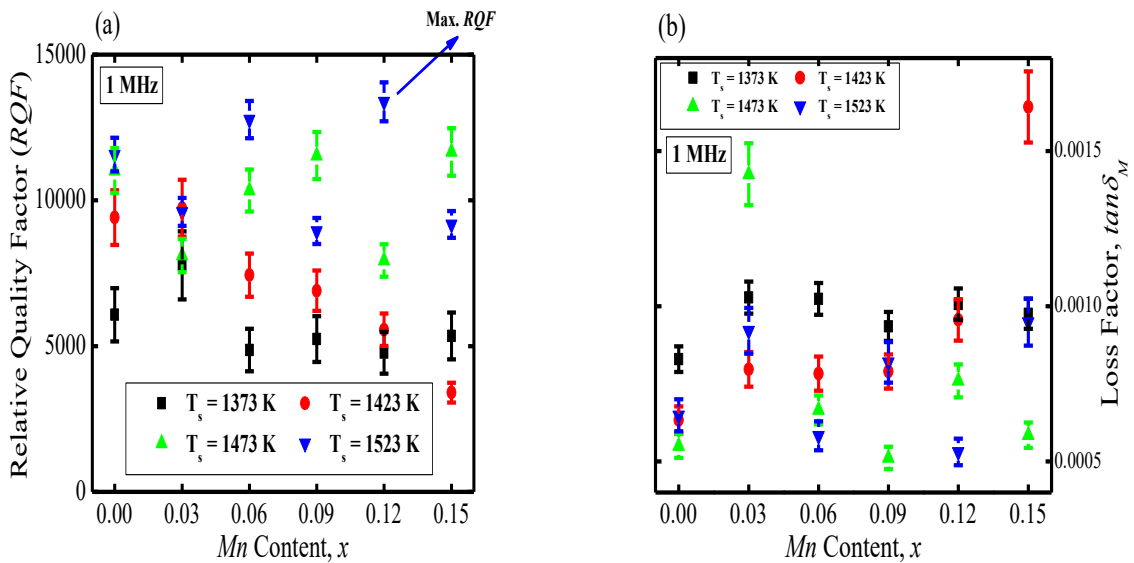


Fig. 5.17. The variation of (a) RQF and (b) $\tan\delta_M$ as a function of Mn content (x) for various $Li_{0.15}Ni_{0.30-x}Mn_xZn_{0.40}Fe_{2.15}O_4$ spinel ferrite nanoparticles at a constant frequency of 1 MHz sintered at various temperatures.

Therefore, one can expect higher μ_i' for a particular composition sintered at higher T_s . In this study, μ_i' is found to be highest (=334) at the sintering temperature of 1523 K (optimum T_s). Now, if the sintering temperature goes beyond the optimum T_s , the value of μ_i' will assume to be decreased. It is conceivable that the samples sintered at above

optimum T_s increase the number of pores inside the grain, as a result, the value of μ_i' decreases. The pores play as pinning sites for the domain wall movement. Consequently, domain wall movement is hindered and this limits the growth of μ_i' [12].

The variation of μ_i' (1 MHz) and μ_i'' (1 MHz) with Mn content for various $Li_{0.15}Ni_{0.30-x}Mn_xZn_{0.40}Fe_{2.15}O_4$ spinel ferrite nanoparticles sintered at different T_s are shown in **Fig. 5.16**. This figure illustrates that the μ_i' reaches its maximum value for $x=0.12$ sintered at 1523 K and μ_i'' plays an opposite role for the same sample. **Fig. 5.17** shows the change of RQF (1 MHz) and $\tan\delta_M$ (1 MHz) with Mn content for various $Li_{0.15}Ni_{0.30-x}Mn_xZn_{0.40}Fe_{2.15}O_4$ spinel ferrite nanoparticles sintered at 1373, 1423, 1473, and 1523 K. From this figure, it was found that for $x=0.12$ sintered at 1523 K the RQF reaches its maximum value and $\tan\delta_M$ shows the opposite result.

5.4 Temperature-dependent permeability and Néel temperature

The temperature-dependent real part of initial permeability (μ_i') was studied at a constant frequency (1 MHz) to find the Néel temperature of the studied samples. The real part of the initial permeability (μ_i') as a function of temperature (μ_i' vs. T plot) for $Li_{0.15}Ni_{0.30-x}Mn_xZn_{0.40}Fe_{2.15}O_4$ spinel ferrite nanoparticles sintered at 1523 K is shown in **Fig. 5.18(a)**.

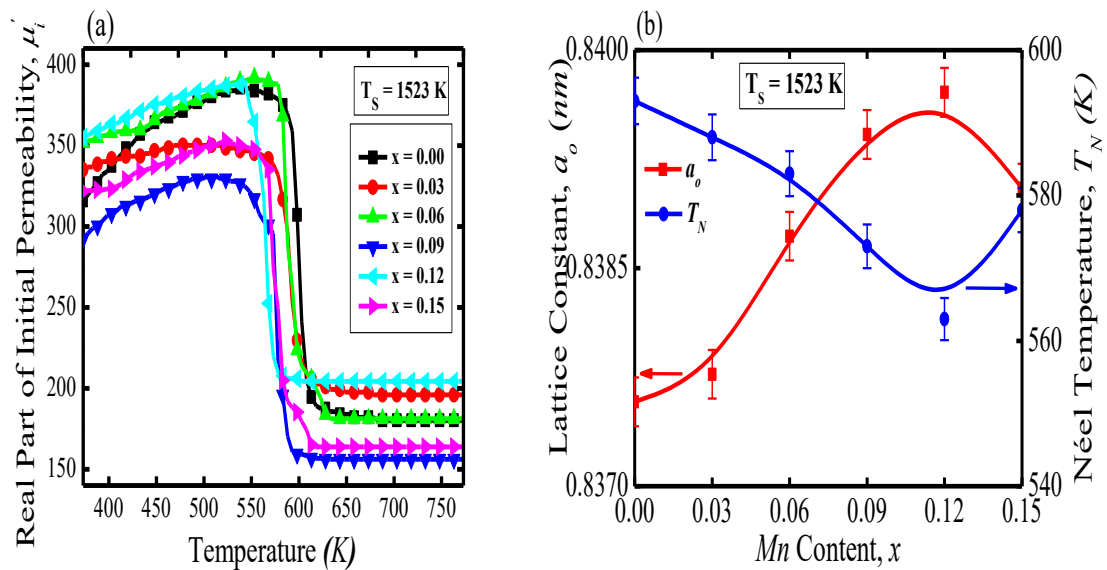


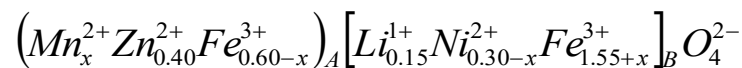
Fig. 5.18. (a) The temperature-dependent μ_i' (at constant frequency 1 MHz) and (b) Variation of a_o and T_N with Mn content (x) for various $Li_{0.15}Ni_{0.30-x}Mn_xZn_{0.40}Fe_{2.15}O_4$ spinel ferrite nanoparticles sintered at 1523 K.

It is observed that μ_i' slowly increases with temperature, reaches a maximum and then drops sharply at a certain temperature, known as Néel temperature (T_N) for all samples. A sharp decrease of the μ_i' at the Neel temperature indicates a good compositional homogeneity in the ferrite samples.

The Néel temperature (T_N) for different samples is presented in **Table 5.3**. It is a function of the exchange energy. Physically, at T_N , the thermal agitation is so violent that it reduces the alignment of the magnetic moment along a given axis to zero [14,29]. It follows that a ferrimagnetic material above its T_N is paramagnetic. Variation of a_o and T_N with Mn content (x) for various $Li_{0.15}Ni_{0.30-x}Mn_xZn_{0.40}Fe_{2.15}O_4$ samples sintered at 1523 K is plotted in **Fig. 5.18(b)**. It is noticed that T_N decreases continuously with increasing Mn^{2+} substitution up to $x=0.12$, beyond this T_N increases. The value of T_N is found to decrease from 593 (for $x=0.00$) to 563 K (for $x=0.12$). This suggests that Mn^{2+} ions may be incorporated into the lattice of ferrites, resulting in the weakening of A - B interaction between the two sub-lattices in the ferrite. This could be attributed to the increase in distance between the moments of A - and B -sites (i.e. the hopping lengths, L_{A-B} , presented in **Table 5.2**), which is confirmed by the increase in the lattice constant with increasing Mn^{2+} concentration up to $x=0.12$. Beyond this decrease in the lattice constant with increasing Mn^{2+} substitution indicates the enhancement of T_N from 563 (for $x=0.12$) to 578 K (for $x=0.15$).

5.5. *dc* magnetization of $Li_{0.15}Ni_{0.30-x}Mn_xZn_{0.40}Fe_{2.15}O_4$

The magnetic properties of the various $Li_{0.15}Ni_{0.30-x}Mn_xZn_{0.40}Fe_{2.15}O_4$ could be explained by super-exchange interaction between A - and B -sites. As a normal behavior, the magnetization (M) of all composition is assumed to be increased linearly with increasing of the applied magnetic field up to a certain value and attains its saturation values (M_s) for fields higher than that of the certain value of applied magnetic field. It is expected that, as Mn concentration increases μ_i' and M_s increased up to its maximum value. This could be explained by the cation distribution and super-exchange interaction between A - and B -sites. In this present study, the probable cation distribution may be written as:



Where the parentheses () and square brackets [] represent *A*- and *B*-sites, respectively. It is known that Mn^{2+} (magnetic moment= $5\mu_B$) and Zn^{2+} (non-magnetic) ions prefer the *A*-sites while Li^{1+} (non-magnetic) and Ni^{2+} (magnetic moment= $2\mu_B$) ions occupy *B*-sites. Although Fe^{3+} (magnetic moment= $5\mu_B$) ions may exist at both *A*- and *B*-sites. Moreover, it is to be mentioned that the cation distribution of Mn^{3+} and Mn^{4+} situated at the *B*-sites [12].

According to Néel's two sub-lattice model *A*-*B* super-exchange interaction is predominant over inter-sub-lattice *A*-*A* and *B*-*B* interaction, and the net magnetization is given by the vector sum of the magnetic moments of the individual *A* and *B* sub-lattices:

$$M_T(T) = M_B(T) - M_A(T).$$

Where M_A is the magnetization of *A*-sites, M_B is the magnetization of *B*-sites, M_T is the total (net) magnetization, and T is the temperature. As Li^{1+} and Zn^{2+} do not contribute to the magnetization because of being non-magnetic, Ni^{2+} , Mn^{2+} , and Fe^{3+} ions having magnetic moment $2\mu_B$, $5\mu_B$, and $5\mu_B$, respectively results the net magnetic moment which can be estimated as below:

The magnetization of *A*-sites,

$$\begin{aligned} M_A(T) &= [5 \times (x) + 5 \times (0.60 - x)]\mu_B \\ \Rightarrow M_A(T) &= 3\mu_B. \end{aligned}$$

Similarly, the magnetization of *B*-sites,

$$\begin{aligned} M_B(T) &= [2 \times (0.30 - x) + 5 \times (1.55 + x)]\mu_B \\ \Rightarrow M_B(T) &= (8.35 + 3x)\mu_B. \end{aligned}$$

Now, the total (net) magnetization,

$$\begin{aligned} M_T(T) &= [(8.35 + 3x) - 3]\mu_B \\ \Rightarrow M_T(T) &= (5.35 + 3x)\mu_B. \end{aligned}$$

From this estimation, it can be seen that total (net) magnetization (M_T) increases with increasing *Mn* content. When Mn^{2+} ions are substituted instead of Ni^{2+} ions in *Li-Ni-Zn* ferrite, Mn^{2+} ions enter *A*-sites (tetrahedral position) [14]. As a result, some of the Fe^{3+} ions migrate from *A* to the *B*-sites in view of the site preferences for different ions as mentioned above, which influence the enhancement of total (net) magnetization (M_T) in

present ferrite samples. The estimated values of total (net) magnetization (M_T) based on the preferred sites of the cations for various samples are presented in **Table 5.3**.

5.6 Dielectric properties of $Li_{0.15}Ni_{0.30-x}Mn_xZn_{0.40}Fe_{2.15}O_4$

The dielectric properties of ferrites are affected by several factors, like structural homogeneity, chemical composition, preparation method, density, porosity, grain size, sintering temperature and atmosphere, impurity levels etc. [20,30]. The variation of dielectric constant (ϵ') as a function of frequency is shown in **Fig. 5.19(a)**. It is observed that the dielectric constant decrease steeply at lower frequencies and remains constant at higher frequencies. It indicates the usual dispersion behavior in the lower frequency region. The dispersion behavior is observed due to the presence of Maxwell-Wagner type interfacial polarization in accordance with Koop's phenomenological theory [31-33]. In this model, the dielectric structure is assumed to consist of two layers. The first layer is a conducting layer consists of large grains and the other being grain boundaries are a poor conductor. According to this theory, the conductivity of grain boundaries contributes more effectively to the dielectric constant at lower frequencies.

For ferrites, the ϵ' is directly proportional to the square root of conductivity [33-34]. The grain boundaries have lower values of ϵ' and conductivity while the grains have higher values of these. At lower frequencies, the grain boundaries are more effective than the grains controlling the electrical conduction. Therefore, the ϵ' is higher at lower frequencies and decreases with frequency. The low-frequency dispersion in ferrites may be observed due to the space charge effect. It is also found that the dielectric constant varies with increase in Mn content. The substitution of Mn for Ni could modify the structural homogeneity which would cause a decrease in the degree of polarization. The conduction mechanism and the dielectric behavior of ferrites have strong correlation [35-39]. By electronic exchange, $Fe^{3+} \leftrightarrow Fe^{2+}$ and $Mn^{2+} \leftrightarrow Mn^{3+}$, one obtains the local displacement of the electrons in the direction of the applied electric field. These displacements of the electrons contribute to the polarization of the ferrites. By increasing frequency polarization decreases and reaches a constant minimum value due to the fact that beyond a certain frequency of the electric field, the electric dipoles are unable to follow the fast alteration of the applied alternating electric field. In other words, the electronic exchange between

ferrous and ferric ions cannot follow the alternating field [40]. The exchange of electrons between Fe^{2+} and Fe^{3+} and the exchange of holes between Mn^{3+} and Mn^{2+} in the octahedral sites of manganese ferrites results in local displacement of charge carriers in the direction of the electric field which leads to electric polarization. Similar behavior of dielectric constant with frequency had been reported by Shaikh et al. [34].

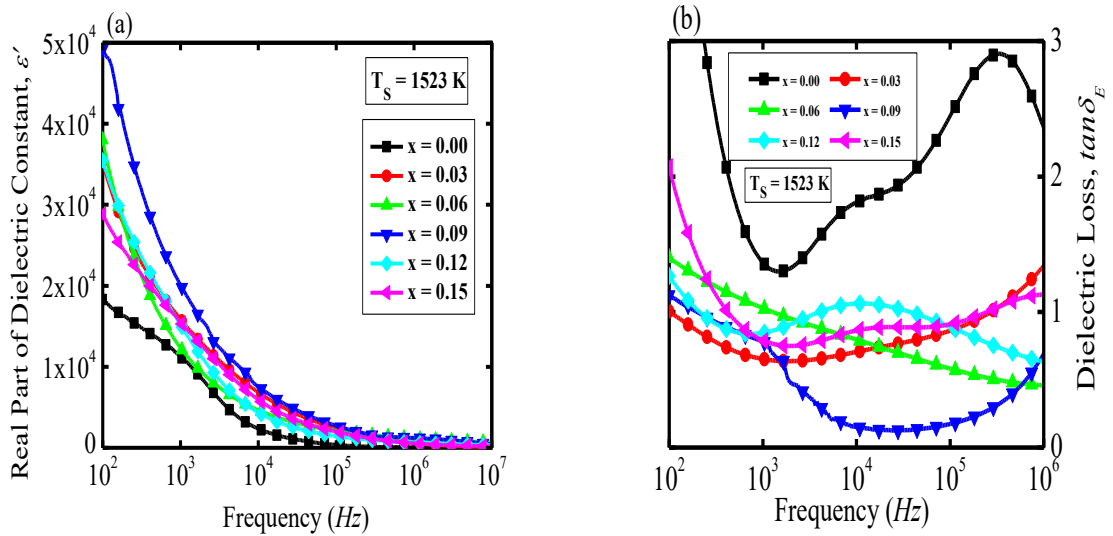


Fig. 5.19. The variation of the (a) Real part of dielectric constant (ϵ') and (b) Loss tangent ($\tan\delta_E$) as a function of frequency at room temperature for various $Li_{0.15}Ni_{0.30-x}Mn_xZn_{0.40}Fe_{2.15}O_4$ spinel ferrite nanoparticles sintered at 1523 K .

Fig. 5.19(b) shows the variation of dielectric loss tangent ($\tan\delta_E$) with frequency. The dielectric loss arises mainly due to impurities and imperfections in the crystal lattice. It is observed that the dielectric loss tangent for all compositions decreases with increasing frequency and slightly increases at a higher frequency. The dielectric loss decreases with the increase of frequency due to the fact that the hopping frequency of the electron exchange between Fe^{2+} and Fe^{3+} ions at adjacent octahedral sites cannot follow the changes of the external ac applied electric field beyond a certain frequency limit. The dielectric loss peaks can be explained by the Debye relaxation theory. The peak in the dielectric loss arises when the hopping frequency is nearly equal to the frequency of the externally applied electric field and condition $\omega\tau=1$ ($\omega=2\pi f$) is satisfied. At higher frequencies, losses are found to be low since domain wall motion is inhibited and

magnetization is forced to change by rotation. The dielectric loss tangent decreases inversely as the frequency. At higher frequency, the loss is small, which ensures that present ferrites could possibly be used in practical applications [41-43].

5.7 Complex impedance spectroscopy study

To study the electrical properties of ferrites nanoparticles, impedance spectroscopy is an important method as the impedance of grains can be separated from the other impedance sources, such as the impedance of electrodes and grain boundaries. The analysis of impedance is essential to get information about the resistive (real part) and reactive (imaginary part) components of the materials.

Fig. 5.20(a) illustrates the variation of the real part of impedance (Z') for all the samples sintered at 1523 K as a function of frequency at room temperature. It is found that the magnitude of Z' gradually decreases with increasing frequency up to a certain frequency (0.1 MHz) for all samples.

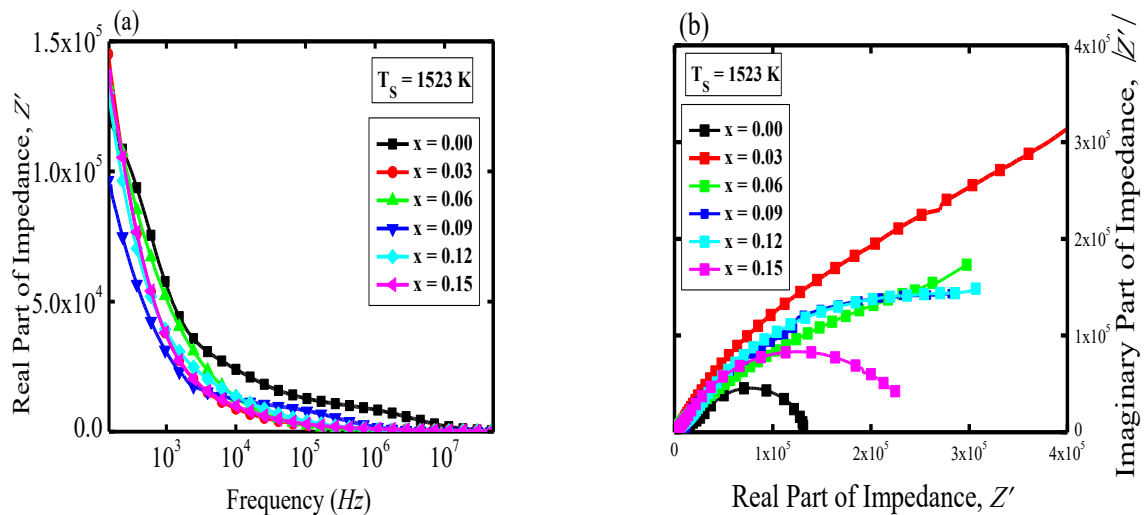


Fig. 5.20. (a) The variation of Z' with frequency and (b) The Cole-Cole plot at room temperature for various $\text{Li}_{0.15}\text{Ni}_{0.30-x}\text{Mn}_x\text{Zn}_{0.40}\text{Fe}_{2.15}\text{O}_4$ spinel ferrite nanoparticles sintered at 1523 K .

The decrease in Z' indicates that the conduction is increasing with frequency and at the higher frequency ($\geq 0.1\text{ MHz}$) it becomes almost frequency independent. At lower frequencies, the higher values of Z' indicates the larger polarization. At higher frequencies,

the lower values of Z' for all samples declare the possible release of space charge polarization at the boundaries of homogeneous phases in the composites under the applied external field [44]. A ferrite material is assumed to be consisting of crystalline plates.

A sample is assumed as a microstructure made up of parallel conducting plates (grains) separated by resistive plates (grain boundaries). Generally, two semicircles are observed in the Cole-Cole plot; first semicircle at low-frequency side represents the grain boundary resistance and the second semicircle at high frequency corresponds to the resistance of grain or bulk [45]. The complex impedance or Cole-Cole plot for all the compositions sintered at 1523 K as a function of frequency at room temperature is presented in Fig. 5.20(b). The plot obtained shows only one semi-circular arc for all the ferrite compositions corresponding to the conduction due to the grain boundary volume in the low-frequency region. This single semicircle suggests that through the grain boundary volume conduction mechanism takes place predominantly [46].

5.8 ac conductivity and ac resistivity

The ac conductivity and resistivity of ferrites give the fundamental information associated to the concentration of charge carriers at grain or grain boundaries, dielectric polarization of magnetic ions and inter-granular tunneling of charge carriers across the grain boundary. The variation of ac conductivity (σ_{ac}) and ac resistivity (ρ_{ac}) as a function of frequency at room temperature for various $Li_{0.15}Ni_{0.30-x}Mn_xZn_{0.40}Fe_{2.15}O_4$ spinel ferrites sintered at 1523 K is illustrated in Fig. 5.21. The σ_{ac} and ρ_{ac} were calculated by using the relations:

$\sigma_{ac} = \epsilon_o \epsilon'' \omega$ and $\rho_{ac} = \frac{1}{\epsilon_o \epsilon'' \omega}$, respectively, where ' ϵ_o ' is the permittivity of free space ($\epsilon_o = 8.85 \times 10^{-12} \text{ Fm}^{-1}$), ' ϵ'' ' is the imaginary part of dielectric constant ($\epsilon'' = \epsilon' \tan \delta_E$), ' ϵ' ' is the real part of dielectric constant, ' $\tan \delta_E$ ' is the dielectric loss, and ' ω ' is the angular frequency. From figure, it is observed that at the lower frequency range (up to 0.1 MHz) ρ_{ac} decreases with increasing frequency but at the higher frequencies (above 0.1 MHz) it becomes almost frequency independent and shows negligibly small values. The resistivity mechanism in ferrites can be explained on the basis of electron hopping between Fe^{2+} and Fe^{3+} . The grains are low resistive materials whereas the grain boundaries are high resistive materials. The grain boundaries having highly resistivity are more active

at lower frequency region so the hopping frequency of electron between Fe^{3+} and Fe^{2+} is less at lower frequencies. With the increase in the frequency of applied field, the grains having low resistivity become more active, consequently, the hopping frequency of electron between Fe^{3+} and Fe^{2+} enhance. As a result, the ρ_{ac} gradually decreases with frequency whereas the ac electrical conductivity increases [31-32,46].

Ferrites having high density provide high ρ_{ac} . However, among the studied samples, $Li_{0.15}Ni_{0.27}Mn_{0.03}Zn_{0.40}Fe_{2.15}O_4$ and $Li_{0.15}Ni_{0.18}Mn_{0.12}Zn_{0.40}Fe_{2.15}O_4$ sintered at 1523 K show comparatively higher ρ_{ac} at lower frequency range. In ferrites, two metal ions existing at B -sites are closer than two metal ions existing at different sites, one at A -sites and another one at B -sites.

Therefore, the probability of electron hopping between B - B sites is greater than B - A sites. Hopping between A - A sites may not exist because during the sintering process some Fe^{2+} are formed and preferentially occupy B -sites only. It is expected that as Mn^{2+} prefer A -sites, so the doping will decrease the resistivity linearly with increasing Mn content which can be explained by the following arguments. Due to the relative difference between the ionic radii of Mn^{2+} and Ni^{2+} , the substitution of Mn^{2+} in place of Ni^{2+} will expand the bond length and unit cell, and reduce the overlapping of orbitals, consequently, the hopping probability will be reduced.

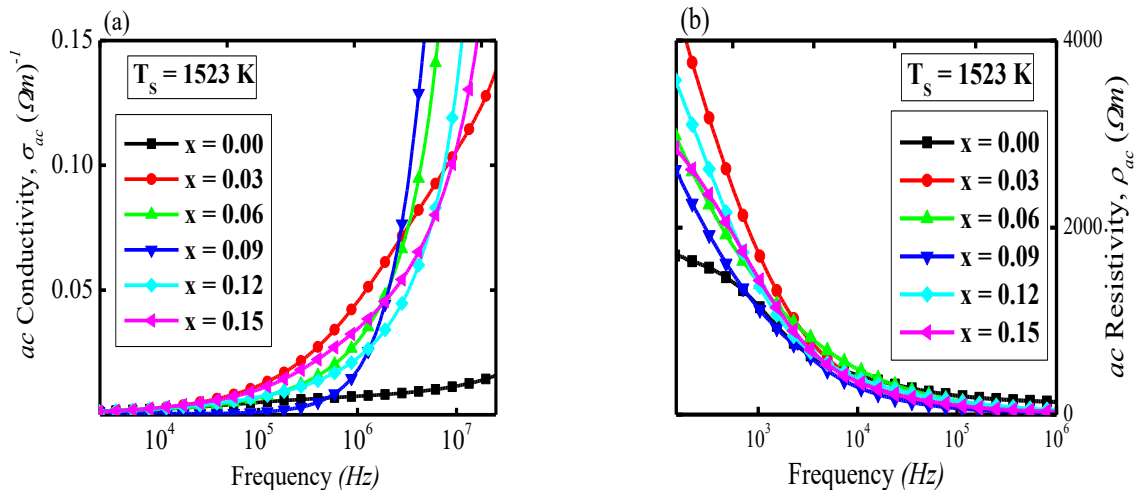


Fig. 5.21. The variation of (a) ac conductivity (σ_{ac}) and (b) ac resistivity (ρ_{ac}) as a function of frequency for various $Li_{0.15}Ni_{0.30-x}Mn_xZn_{0.40}Fe_{2.15}O_4$ spinel ferrites sintered at 1523 K .

However, the observed resistivity does not decrease linearly by obeying the above-mentioned reasons. The deviation from linearity may be explained by assuming that at higher concentrations some Mn^{2+} may possibly occupy B -sites besides a large portion of it going to A -sites, whereas for lower concentrations Mn^{2+} preferentially occupy A -sites.

References:

- [1] Rahman, M. A., Rahman, M. A., and Hossain, A. K. M. A., "Effect of Cu^{2+} substitution on structural, magnetic and transport properties of $Fe_{2.5}Zn_{0.5-x}Cu_xO_4$," *Journal of Magnetism and Magnetic Materials*, vol. 369, pp. 168-175, 2014.
- [2] Momin, A. A., Parvin, R., and Hossain, A. K. M. A., "Structural, morphological and magnetic properties variation of nickel-manganese ferrites with lithium substitution," *Journal of Magnetism and Magnetic Materials*, vol. 423, pp. 124-132, 2017.
- [3] Hessien, M. M., Rashad, M. M., El-Barawy, K., and Ibrahim, I. A., "Influence of manganese substitution and annealing temperature on the formation, microstructure and magnetic properties of Mn-Zn ferrites," *Journal of Magnetism and Magnetic Materials*, vol. 320(9), pp. 1615-1621, 2008.
- [4] Kumar, E. R., Jayaprakash, R., and Kumar, S., "The role of annealing temperature and bio template (egg white) on the structural, morphological and magnetic properties of manganese substituted MFe_2O_4 ($M=Zn, Cu, Ni, Co$) nanoparticles," *Journal of Magnetism and Magnetic Materials*, vol. 351, pp. 70-75, 2014.
- [5] Scherrer, P., "Göttinger Nachrichten Math.," *Phys.*, vol. 2, pp. 98-100, 1918.
- [6] Botta, P. M., Bercoff, P. G., Aglietti, E. F., Bertorello, H. R., and López, J. P., "Two alternative synthesis routes for MnZn ferrites using mechanochemical treatments.," *Ceramics international*, vol. 32(8), pp. 857-863, 2006.
- [7] Bhosale, D. N., Verenkar, V. M. S., Rane, K. S., Bakare, P. P., and Sawant, S. R., "Initial susceptibility studies on Cu-Mg-Zn ferrites," *Materials chemistry and physics*, vol. 59(1), pp. 57-62, 1999.
- [8] Jalaiah, K., and Babu, K. V., "Structural, magnetic and electrical properties of nickel doped Mn-Zn spinel ferrite synthesized by sol-gel method," *Journal of Magnetism and Magnetic Materials*, vol. 423, pp. 275-280, 2017.
- [9] Mohseni, H., Shokrollahi, H., Sharifi, I., and Gheisari, K., "Magnetic and structural studies of the Mn-doped Mg-Zn ferrite nanoparticles synthesized by the glycine nitrate process," *Journal of Magnetism and Magnetic Materials*, vol. 324(22), pp. 3741-3747, 2012.
- [10] Vegard, L., "Die konstitution der mischkristalle und die raumfüllung der atome," *Zeitschrift für Physik A Hadrons and Nuclei*, vol. 5(1), pp. 17-26, 1921.

- [11] Rashid, M. H., and Hossain, A. K. M. A., "Structural, morphological and electromagnetic properties of Sc^{3+} doped Ni-Cu-Zn ferrites," *Results in Physics*, vol. 11, pp. 888-895, 2018.
- [12] Islam, M. A., Hasan, M., and Hossain, A. K. M. A., "Enhancement of initial permeability and reduction of loss factor in Zn substituted nanocrystalline $\text{Li}_{0.35-0.5x}\text{Ni}_{0.3}\text{Zn}_x\text{Fe}_{2.35-0.5x}\text{O}_4$," *Journal of Magnetism and Magnetic Materials*, vol. 424, pp. 108-114, 2017.
- [13] Shannon, R. D., "Revised effective ionic radii and systematic studies of interatomic distances in halides and chalcogenides," *Acta Crystallographica Section A: Crystal Physics, Diffraction, Theoretical and General Crystallography*, vol. 32(5), pp. 751-767, 1976.
- [14] Hossain, A. K. M. A., Biswas, T. S., Mahmud, S. T., Yanagida, T., Tanaka, H., and Kawai, T., "Enhancement of initial permeability due to Mn substitution in polycrystalline $\text{Ni}_{0.50-x}\text{Mn}_x\text{Zn}_{0.50}\text{Fe}_2\text{O}_4$," *Journal of Magnetism and Magnetic Materials*, vol. 321(2), pp. 81-87, 2009.
- [15] Huheey, J. E., Keiter, E. A., and Keiter, R. L., (1993) *Principles and applications of inorganic chemistry, 4th ed.*, Harpercollins, New York.
- [16] M. J. Winter, www.webelements.com, University of Sheffield, UK, 1995-2006.
- [17] Sattar, A. A., El-Sayed, H. M., El-Shokrofy, K. M., and El-Tabey, M. M., "Improvement of the magnetic properties of Mn-Ni-Zn Ferrite by the nonmagnetic Al-Ion substitution," *J. Appl. Sci.*, vol. 5(1), pp. 162-168, 2005.
- [18] El-Ghazzawy, E. H., and Amer, M. A., "Structural, elastic and magnetic studies of the as-synthesized $\text{Co}_{1-x}\text{Sr}_x\text{Fe}_2\text{O}_4$ nanoparticles," *Journal of Alloys and Compounds*, vol. 690, pp. 293-303, 2017.
- [19] Mendelson, M. I., "Average grain size in polycrystalline ceramics," *Journal of the American Ceramic society*, vol. 52(8), pp. 443-446, 1969.
- [20] Rahaman, M. D., Mia, M. D., Khan, M. N. I., and Hossain, A. K. M. A., "Study the effect of sintering temperature on structural, microstructural and electromagnetic properties of 10% Ca-doped $\text{Mn}_{0.6}\text{Zn}_{0.4}\text{Fe}_2\text{O}_4$," *Journal of Magnetism and Magnetic Materials*, vol. 404, pp. 238-249, 2016.
- [21] Nakamura, T., "Snoek's limit in high-frequency permeability of polycrystalline Ni-Zn, Mg-Zn, and Ni-Zn-Cu spinel ferrites," *Journal of applied physics*, vol. 88(1), pp. 348-353, 2000.
- [22] Jun, H., and Mi, Y., "Preparation of high- permeability NiCuZn ferrite," *J. Zhejiang Univ. Sci.*, vol. 6B(6), pp. 580-583, 2005.
- [23] Tsutaoka, T., Ueshima, M., Tokunaga, T., Nakamura, T., and Hatakeyama, K., "Frequency dispersion and temperature variation of complex permeability of Ni-Zn ferrite composite materials," *Journal of Applied Physics*, vol. 78(6), pp. 3983-3991, 1995.
- [24] Globus, A., Duplex, P., and Guyot, M., "Determination of initial magnetization curve from crystallites size and effective anisotropy field," *IEEE Transactions on Magnetics*, vol. 7(3), pp. 617-622, 1971.
- [25] Bloembergen, N., "Magnetic resonance in ferrites," *Proceedings of the IRE*, vol. 44(10), pp. 1259-1269, 1956.

- [26] Snoek, J. L., "Dispersion and absorption in magnetic ferrites at frequencies above one Mc/s," *Physica*, vol. 14(4), pp. 207-217, 1948.
- [27] Overshott, K., "The causes of the anomalous loss in amorphous ribbon materials," *IEEE transactions on Magnetics*, vol. 17(6), pp. 2698-2700, 1981.
- [28] Valenzuela, R. (1994) *Magnetic ceramics (Vol. 4)*, Cambridge University Press, Cambridge.
- [29] Chauhan, B. S., Kumar, R., Jadhav, K. M., and Singh, M., "Magnetic study of substituted Mg-Mn ferrites synthesized by citrate precursor method," *Journal of magnetism and magnetic materials*, vol. 283(1), pp. 71-81, 2004.
- [30] Dimri, M. C., Verma, A., Kashyap, S. C., Dube, D. C., Thakur, O. P., and Prakash, C., "Structural, dielectric and magnetic properties of NiCuZn ferrite grown by citrate precursor method," *Materials Science and Engineering: B*, vol. 133(1-3), pp. 42-48, 2006.
- [31] Maxwell, J. C. (1892) *A Treatise on Electricity and Magnetism (3rd ed., Vol. 1)*, Oxford University Press, Oxford.
- [32] Wagner, K. W., "The theory of incomplete dielectricity," *Ann. Phys.*, vol. 40, p. 817, 1913.
- [33] Koops, C. G., "On the dispersion of resistivity and dielectric constant of some semiconductors at audiofrequencies," *Physical Review*, vol. 83(1), p. 121, 1951.
- [34] Shaikh, A. M., Bellad, S. S., and Chougule, B. K., "Temperature and frequency-dependent dielectric properties of Zn substituted Li-Mg ferrites," *Journal of Magnetism and Magnetic Materials*, vol. 195(2), pp. 384-390, 1999.
- [35] George, M., Nair, S. S., Malini, K. A., Joy, P. A., and Anantharaman, M. R., "Finite size effects on the electrical properties of sol-gel synthesized CoFe₂O₄ powders: deviation from Maxwell-Wagner theory and evidence of surface polarization effects," *Journal of Physics D: Applied Physics*, vol. 40(6), p. 1593, 2007.
- [36] Rao, B. P., and Rao, K. H., "Effect of sintering conditions on resistivity and dielectric properties of Ni-Zn ferrites," *Journal of materials science*, vol. 32(22), pp. 6049-6054, 1997.
- [37] Jadhav, P. A., Devan, R. S., Kolekar, Y. D., and Chougule, B. K., "Structural, electrical and magnetic characterizations of Ni-Cu-Zn ferrite synthesized by citrate precursor method," *Journal of Physics and Chemistry of solids*, vol. 70(2), pp. 396-400, 2009.
- [38] Iwachi, K., "Dielectric Properties of Fine Particles of Fe₃O₄ and Some Ferrites," *Japanese Journal of Applied Physics*, vol. 10(11), pp. 1520-1528, 1971.
- [39] Rabinkin, I. T., and Novikova, Z. I., (1960) *Ferrites*, IZV Acad, Nauk USSR Minsk.
- [40] Ponpandian, N., et al., "Electrical conductivity and dielectric behaviour of nanocrystalline NiFe₂O₄ spinel," *J. Phys.: Condens. Matter*, vol. 14, pp. 3221-3237, 2002.
- [41] Ravinder, D., and Kumar, K. V., "Dielectric behaviour of erbium substituted Mn-Zn ferrites," *Bulletin of Materials Science*, vol. 24(5), pp. 505-509, 2001.
- [42] James, A. R., Prakash, C., and Prasad, G., "Structural properties and impedance spectroscopy of excimer laser ablated Zr substituted BaTiO₃ thin films," *Journal of Physics D: Applied Physics*, vol. 39(8), p. 1635, 2006.

- [43] Rezlescu, E., Rezlescu, N., Popa, P. D., Rezlescu, L., and Pasnicu, C., “The influence of R_2O_3 (R= Yb, Er, Dy, Tb, Gd, Sm and Ce) on the electric and mechanical properties of a nickel–zinc ferrite,” *Physica status solidi (a)*, vol. 162(2), pp. 673-678, 1997.
- [44] Rahaman, M. D., Setu, S. H., Saha, S. K., and Hossain, A. K. M. A., “Synthesis and characterization of $La_{0.75}Ca_{0.15}Sr_{0.05}Ba_{0.05}MnO_3-Ni_{0.9}Zn_{0.1}Fe_2O_4$ multiferroic composites,” *Journal of Magnetism and Magnetic Materials*, vol. 385, pp. 418-427, 2015.
- [45] Kambale, R. C., Shaikh, P. A., Bhosale, C. H., Rajpure, K. Y., and Kolekar, Y. D., “Dielectric properties and complex impedance spectroscopy studies of mixed Ni–Co ferrites,” *Smart Materials and Structures*, vol. 18(8), p. 085014, 2009.
- [46] Battoo, K. M., and Ansari, M. S., “Low temperature-fired Ni-Cu-Zn ferrite nanoparticles through auto-combustion method for multilayer chip inductor applications,” *Nanoscale research letters*, vol. 7(1), p. 112, 2012.

.....

CHAPTER 6

CONCLUSIONS

Major findings from the structural, morphological, magnetic, and dielectric studies of the ferrite samples as well as suggestions of future works are listed in this chapter.

6.1 Major findings of present study

Major findings of the study of the present ferrite ($Li_{0.15}Ni_{0.30-x}Mn_xZn_{0.40}Fe_{2.15}O_4$) samples sintered at various temperatures are mentioned below:

- The structural analysis (XRD) of various $Li_{0.15}Ni_{0.30-x}Mn_xZn_{0.40}Fe_{2.15}O_4$ confirms that all the samples have spinel structure consist of major (primary) spinel cubic phase including minor (secondary) impurity Fe_2O_3 and MnO phases.
- The crystallite size ($D_{crystallite}$) was estimated by Debye-Scherrer formula, which shows a decreasing trend with increasing Mn content up to $x=0.12$, beyond that $D_{crystallite}$ increased.
- The mean ionic radius and $r_{(variant)}$ of the variant ions for $Li_{0.15}Ni_{0.30-x}Mn_xZn_{0.40}Fe_{2.15}O_4$ is increased with increasing Mn content. The lattice constant (a_o) and distance between magnetic ions (hopping lengths) in the A -sites, shared sites, and B -sites are also increased with increasing Mn content up to $x=0.12$, beyond that they decreased.
- For a fixed T_s ($=1523$ K), both theoretical density (ρ_{th}) and bulk density (ρ_B) decreased in a similar fashion with the increase of Mn content up to $x=0.12$ in present ferrite samples, but for $x=0.15$ they increased. An opposite trend was found for the porosity. The ρ_B of various samples increased and as expected porosity decreased with T_s .
- The average grain size (D_{grain}), estimated by linear intercept technique from the FESEM micrograph, was found to increase with increasing Mn^{2+} substitution up to $x=0.12$, beyond that D_{grain} decreased. The EDS analysis of various

$Li_{0.15}Ni_{0.30-x}Mn_xZn_{0.40}Fe_{2.15}O_4$ confirmed the presence of all elements (Ni , Mn , Zn , Fe , and O) except Li .

- It is found that for fixed T_s , the real part (μ_i') and imaginary part (μ_i'') of initial permeability, relative quality factor (RQF), and magnetic loss factor ($\tan\delta_M$) varied with the variation of Mn content. It is also observed that μ_i' of $Li_{0.15}Ni_{0.18}Mn_{0.12}Zn_{0.40}Fe_{2.15}O_4$ increased with T_s . The maximum value of μ_i' and RQF , as a result, the minimum value of $\tan\delta_M$ are observed in $Li_{0.15}Ni_{0.18}Mn_{0.12}Zn_{0.40}Fe_{2.15}O_4$ sintered at 1523 K.
- The Néel temperature (T_N) decreased as the increase of Mn content up to $x=0.12$, and as usual, the result is opposite for $x=0.15$. A sharp decrease of the μ_i' at the T_N indicates a good compositional homogeneity in the ferrite samples.
- The real part of dielectric constant (ϵ'), dielectric loss tangent ($\tan\delta_E$), complex impedance, ac conductivity (σ_{ac}), and ac resistivity (ρ_{ac}) were studied in the frequency range 100 Hz-100 MHz.
- Frequency dependence of ϵ' in lower frequencies indicates a usual dielectric dispersion. The $\tan\delta_E$ shows similar behavior like ϵ' .
- The effect of grain and grain boundaries on the electrical properties was confirmed by the complex impedance analysis study of the samples.
- The σ_{ac} showed frequency independent behavior at lower frequency region and with increasing frequency the conductivity increases. An inverse trend is observed for ρ_{ac} .

However, these results indicated the importance of present ferrite nanoparticles in practical applications. These ferrites might be applicable as the materials of the component of various electronic devices, such as the electronic filters, microwave devices, transducers, magnetic switches, memory elements for the computer etc. Magnetic nanoparticles of these ferrites might be helpful for the biomedical equipment and medical diagnostics.

6.2 Suggestions for further research

The works on *Mn* substituted *Li-Ni-Zn* ferrites which can be conducted in the future are mentioned hereafter:

- Divalent and trivalent cations can be substituted in $Li_{0.15}Ni_{0.18}Mn_{0.12}Zn_{0.40}Fe_{2.15}O_4$ to enhance its magnetic properties.
- Sintering additives like Bi_2O_3 and V_2O_5 can be mixed to promote densification and getting a better result in lower sintering temperatures to magnetic materials.
- The molar ratio of metals to citric acid during sample preparation was 1:3 in this study. This ratio can be changed to control the reaction time.
- The variation in sintering temperature can be investigated in present ferrite materials.
- *dc* magnetization can be investigated for these ferrite samples.
- Electron spin resonance (*ESR*) studies of *Mn* substituted *Li-Ni-Zn* ferrites may be performed for investigating magnetic properties of the samples.
- An investigation on the Mössbauer effect for *Mn* substituted ferrite (nanoparticle) samples can be performed.

.....

Appendices

APPENDIX-A. STOICHIOMETRIC AMOUNTS OF THE COMPOUNDS (grams)

Md. Moiful Alam; ID: 0413143016F; M. Phil. (Physics), BUET											
Stoichiometric amounts of the compounds (for auto-combustion)											
Li _{0.15} Ni _{0.30-x} Mn _x Zn _{0.40} Fe _{2.15} O ₄											
Serial	Name of the compounds	Mass of the compounds (molecular mass, g/mole)	Required mass of the compounds (molecular mass, g/mole) (for 20 grams)							Total requirements	Comment(s)
			For sample-1	For sample-2	For sample-3	For sample-4	For sample-5	For sample-6			
----	----	Value of the 'x' =	0.00	0.03	0.06	0.09	0.12	0.15	----	----	
----	----	Mass of the samples (g/mole) =	228.8695200	228.7568595	228.6441989	228.5315384	228.4188779	228.3062174	----	----	
1.	LiNO ₃ (≥99%)	68.94594	0.9037	0.9042	0.9046	0.9051	0.9055	0.9060	5.4291	N/A	
2.	Ni(NO ₃) ₂ ·6H ₂ O (≥98.5%)	290.81656	7.6240	6.8650	6.1052	5.3447	4.5834	3.8214	34.3437	N/A	
3.	MnCl ₂ ·4H ₂ O (99.99%)	197.918969	0.0000	0.5191	1.0387	1.5589	2.0795	2.6007	7.7970	N/A	
4.	Zn(NO ₃) ₂ ·6H ₂ O (≥98%)	297.51316	10.3994	10.4045	10.4096	10.4148	10.4199	10.4251	62.4733	N/A	
5.	Fe(NO ₃) ₃ ·9H ₂ O (≥98%)	404.02974	75.9091	75.9465	75.9839	76.0214	76.0589	76.0964	456.0161	N/A	
6.	Citric acid (C ₆ H ₈ O ₇) (99%)	----	43.2225	43.2142	43.2060	43.1977	43.1894	43.1811	259.2110	N/A	
7.	Ammonia solution	----	Up to pH 7	Up to pH 7	Up to pH 7	Up to pH 7	Up to pH 7	Up to pH 7	----	N/A	
8.	Distilled Water	----	Up to dissolve	Up to dissolve	Up to dissolve	Up to dissolve	Up to dissolve	Up to dissolve	----	N/A	

APPENDIX-B. ATOMIC WEIGHT OF THE ELEMENTS (amu)

	1	2	3	4	5	6	7	8	9	10	11	12	13	14	15	16	17	18
1	H 1.00794																	He 4.002602
2	Li 6.941	Be 9.012182											B 10.811	C 12.0107	N 14.00674	O 15.9994	F 18.9984032	Ne 20.1797
3	Na 22.989770	Mg 24.3050											Al 26.981538	Si 28.0855	P 30.973761	S 32.066	Cl 35.4527	Ar 39.948
4	K 39.0983	Ca 40.078	Sc 44.955910	Ti 47.867	V 50.9415	Cr 51.9961	Mn 54.938049	Fe 55.845	Co 58.933200	Ni 58.6934	Cu 63.546	Zn 65.39	Ga 69.723	Ge 72.61	As 74.92160	Se 78.96	Br 79.904	Kr 83.80
5	Rb 85.4678	Sr 87.62	Y 88.90585	Zr 91.224	Nb 92.90638	Mo 95.94	(98)	Tc 101.07	Ru 101.07050	Rh 106.42	Pd 107.8682	Cd 112.411	In 114.818	Sn 118.710	Sb 121.760	Te 127.60	I 126.90447	Xe 131.29
6	Cs 132.90545	Ba 137.327	*	Hf 178.49	Ta 180.9479	W 183.84	Re 186.207	Os 190.23	Ir 192.217	Pt 195.078	Au 196.96655	Hg 200.59	Tl 204.3833	Pb 207.2	Bi 208.98038	Po (209)	At (210)	Rn (222)
7	Fr (223)	Ra (226)	**	Rf (261)	Db (262)	Sg (263)	Bh (262)	Hs (265)	Mt (266)	Uun (269)	Uuu (272)	Uub (277)						
			*	La 138.9055	Ce 140.116	Pr 140.90765	Nd 144.24	Pm (145)	Sm 150.36	Eu 151.964	Gd 157.25	Tb 158.92534	Dy 162.50	Ho 164.93032	Er 167.26	Tm 168.93421	Yb 173.04	Lu 174.967
			**	Ac (227)	Th 232.0381	Pa 231.03588	U 238.0289	Np (237)	Pu (244)	Am (243)	Cm (247)	Bk (247)	Cf (251)	Es (252)	Fm (257)	Md (258)	No (259)	Lr (262)

Element Groups	Alkali Earth	Alkaline Earth	Transition Metals	Rare Earth	Other Metals	Metalloids	Non-Metals	Halogens	Noble Gases
----------------	--------------	----------------	-------------------	------------	--------------	------------	------------	----------	-------------

APPENDIX-C. PRESENTATION BASED ON THIS THESIS

- [1] Moiful Alam, M., and Hossain, A. K. M. A., “Synthesis of Li-Ni-Mn-Zn Ferrite Nanoparticles by Auto-combustion Method and their Size Dependent Electro-magnetic Properties,” presented at the Int. Conference on Physics-2018, 08-10 March, Venue: University of Dhaka, Dhaka, Bangladesh, Poster: PP-108.

.....